Wind Simulation for Extreme and Fatigue Loads

Nielsen, Morten; Larsen, Gunner Chr.; Mann, Jakob; Ott, Søren; Hansen, Kurt Schaldemose; Pedersen, B.J.

Publication date:
2003

Document Version
Publisher's PDF, also known as Version of record

Risø–R–1437(EN)

Wind Simulation for Extreme and Fatigue Loads

M. Nielsen, G. C. Larsen, J. Mann, S. Ott, K. S. Hansen,
and B. J. Pedersen

Risø National Laboratory, Roskilde, Denmark
January 2004

Abstract Målinger af atmosfærisk turbulens afviger fra en Gaussisk proces, specielt hvad angår hastighedsændringer over små tidsskridt, hvor halerne på sandsynlighedsfordelingen snarere er ekspotentielle end Gaussiske. Tælleprincipperne for ekstreme hændelser og eksistensen af kaskader af hændelser gennemgås. Empiriske ekstremstatistikker findes i overensstemmelse med Rices overskridelsesteori, når fordelingerne af hastighedsfluktuationer og deres tidsafledede antages at være uafhængige. Forudsigelser baseret på antagelsen om at turbulensen er en Gaussisk proces vil dog undervurdere forekomsten af ekstremværdier med adskillige størrelsesordner, på grund af afvigelsen fra den sande sandsynlighedsfordeling.

Der er udviklet metoder til at simulere turbulenssignaler of visse forbedringer af beregningseffektiviteten. Metoderne kan anvendes til koblede processer med individuelle spektral- og sandsynlighedsfordelinger. Ikke-Gaussiske processer simuleres med en en transformation fra de Gaussiake tilfælde under hensyntagen til forvrængningen af korrelationsfunktionen; ikke-stationære processer opnås med Bezier interpolation mellem stationære simuleringer med identiske pseudotilfældige tal; mens simulering af systemer, hvor enkelte signaler er kendte, muliggøres med betingede sandsynlighedsfordelinger.

Der er udviklet en alsidig metode til at simulere ekstreme hændelser. Denne metode kan generere vindstød, vindspring, ekstreme hastighedsgradienter, og pludselige vindretningsskift. Der kan foreskrives en ønsket ensemble-middel form af de simulerede hændelser, og metode kan bruges til at find den kritiske hændelse for en given konstruktion. Opgaven formuleres som et variationsproblem, hvor man finder den mest sandsynlige justering af en sædvanlig simulering af en stationær Gaussisk process underlagt den relevante ekstremværdibetingelse, der formuleres som en linearkombination af værdier i processen. Metoden generaliseres til flere korrelerede processer, flere samvirkende betingelser, og tredimesionale felter. Der præsenteres generaliseringer for en enkelt ikke-Gaussisk proces underlagt simple betingelser, og der foreslås yderligere generaliseringer for korrelerede ikke-Gaussiske proceser.

This work is a joint effort of Risø National Laboratory, the Technical University of Denmark, and NEG-Micon A/S, as part of the EFP-2001(Wind) programme sponsored by the Danish Energy Agency, contract no. 1363/01-0005.

ISBN 87–550–3281–8(Internet)
ISSN 0106–2840

Contents

1 Introduction

The verification of the structural integrity of a wind turbine structure involves analyses of fatigue loading as well as extreme loading arising from the environmental wind climate. The present report presents new models that extend and improve the load prediction capabilities within both the above mentioned load categories.

Traditionally, the *fatigue loading* is determined based on synthetic Gaussian turbulence fields reflecting correctly the second order statistics of turbulence associated with flat and homogeneous terrain. In many situations, the Gaussian turbulence description suffices. However, for certain, usually complex, terrain terrain conditions, deviations from the Gaussian behaviour can be observed. These deviations is usually not dramatic, however, on the other not so marginal that they can be neglected. The observed non–Gaussian behaviour is usually characterized by increased probability of large excursions from the mean wind speed. The fatigue loading process is a strongly non–linear function of the loading, and as a consequence the fatigue loading imposed by non–Gaussian turbulence may be substantially increased compared to the Gaussian case. In order to facilitate load predictions under such circumstances, models for generation of non–Gaussian turbulence has been developed and implemented in a computer package. Two different 3D turbulence models have been developed. The first model basically relay on a Winterstein transformation of an associated Gaussian process. For this type of turbulence processes, the third order structure function is invariant to the transformation and thus identical zero, essentially meaning that the resulting time series have no time "orientation". The second 3D turbulence model addresses simulation of non–Gaussian turbulence fields with the third order structure function different from zero. This model is based of non–Gaussian turbulence gradient processes obtained from a Guassian gradient field transformed using a Winterstein transformation. An other type of irregularity where the turbulence characteristics deviates from the Gaussian case, is *non–stationary processes*. In relation to wind turbine load prediction, the most prominent example of such load processes is probably the load situation in wind farms, where the concept of meandering wakes implies that winds at downwind positions are undisturbed for part of the time relieved by episodes of intense turbulence and reduced mean velocity as the wake from upstream turbines hits the observation point. The meandering wake is responsible for low-frequency variations in mean wind speed and turbulence characteristics – the non–stationarity. A simulation strategy for non–stationary processes is described and subsequently exemplified with a wake load situation.

With the trend of persistently growing turbines, the *extreme loading* seems to increase in importance. The extreme loading to be assessed in an ultimate limit state analysis may result from a number of extreme load events including transient operation (start/stop sequences), faults, and extreme wind events. Examples of extreme wind events are extreme mean wind speeds with a recurrence period of 50 years, extreme (short term) wind shear, extreme wind speed gusts and extreme wind direction gusts. The present study addresses extreme wind turbine loading arising only from short term wind events driven by turbulence.

The extreme wind events explicitly accentuated above are included in the currently available draft of the IEC-standard (*IEC 61400-1 Wind Turbine Safety System: part 1, Safety Requirements* n.d.) as extreme load conditions that must be considered as ultimate load cases when designing a wind turbine.

However, the gust events described in the IEC-standard are formulated as coherent gusts of an inherent deterministic character, whereas the gusts experienced in real situation are of a stochastic nature with a limited spatial extension. This

conceptual difference may cause substantial differences in the load patterns of a wind turbine when a gust event is imposed (Dragt & Bierbooms 1996). In order to introduce more realistic extreme load situations of a stochastic nature, a fairly general theory for Gaussian as well as for non–Gaussian gust situations have been developed. Special cases derived from the theory, conceptually reflecting the load cases in the IEC code, have subsequently been implemented in a numerical tool. Contrary to previous work in this area (Bierbooms, Cheng, Larsen & Pedersen 2001),(Bierbooms & Dragt 2000), the present theory offer a fully 3D formulation of the stochastic gust events with their spatial extend resulting from the cross correlation properties of the turbulence field in which they are imbedded. Also the previous works restriction on the quad spectrum has been removed in the present formalism. Likewise, the non–Gaussian gust events was not previously treated.

Having developed models for embedding gusts in a turbulence fields, characterization of the gust amplitudes becomes of importance. This topic is also addressed. A theory for event counting, based on threshold crossing, has been formulated, and predictions from the theory have subsequently been compared with observations originating from field measurements. Two sites have been analysed – the Lammefjord site and the Oak Creek site. The Lammefjord site is characterized by being a flat and homogeneous terrain, whereas the Oak Creek site is a complex mountainous terrain.

2 Gaussianity

It is well known that atmospheric turbulence is approximately Gaussian in the sense that a Gaussian (normal) distribution for a wind component usually fits data well. The skewness[1] S and kurtosis K are the usual measures of the deviation from Gaussianity, with $S = 0$ and $K = 3$ as the values valid for a Gaussian distribution. Nielsen, Hansen & Pedersen (2000b) analyzed a number of different sites found values of S in the range -0.4 to 0.1 and values of K ranging 2.7 to 3.4. Larsen, Bierbooms & Hansen (2004) found similar deviations from Gaussianity for other sites. The cited values are averages over a large number of ten minute runs. In uncomplicated, flat terrain the turbulence tends to be more perfectly Gaussian than in complex terrain.

There does not seem to exist any simple explanation for the observed almost Gaussian pdfs, in fact theory tells us that turbulence is non-Gaussian. For Inertial range turbulence we have Kolmogorov's (1941) famous 4/5 law for the third order structure function, $\langle(\Delta u)^3\rangle = -\frac{4}{5}\varepsilon r$, and $\langle(\Delta v)^2\rangle = C_{\mathrm{K}}(\varepsilon r)^{\frac{2}{3}}$ for the second order structure function where C_{K} is the Kolmogorov constant. Using Taylor's frozen turbulence hypothesis we may set $\Delta u = -(u(t + r/\bar{u}) - u(t))$ so that $\langle\Delta u^3\rangle = -\frac{4}{5}\varepsilon r$ and $\langle\Delta u^2\rangle = C_{\mathrm{K}}(\varepsilon r)^{\frac{2}{3}}$. Thus the skewness of $(u(t + r/\bar{u}) - u(t))$ is equal to $+\frac{4}{5}C_{\mathrm{K}}^{-\frac{3}{2}} \sim 0.3$ using $C_{\mathrm{K}} \sim 2$. Uneven moments of a Gaussian variable are equal to zero, hence Δu is not exactly Gaussian.

Simulations often rely on the stronger assumption that time series $v(t)$ are realizations of a Gaussian process, i.e. the set of all the values $\{v(t)\}$ have a joint Gaussian pdf. Gaussian processes remain Gaussian under linear transformations, hence $\int \phi(t)v(t)dt$ is a Gaussian variable for any ϕ. For ten minute time series from a anemometer, the ten minute mean value $\bar{u}$ should therefore be Gaussian if $u(t)$ is a Gaussian process. This is seldom the case, since in fact $\bar{u}$ more often follows a Weibull distribution. Therefore we choose the variable $v(t) \equiv (u(t) - \bar{u})/\bar{u}$ as the

[1] Definitions: $\sigma^2 \equiv \langle(u - \langle u\rangle)^2\rangle$, $S \equiv \langle(u - \langle u\rangle)^3\rangle/\sigma^3$ and $K \equiv \langle(u - \langle u\rangle)^4\rangle/\sigma^4$

candidate for a Gaussian variable, and regard the $\bar{u}$ as fixed and given. Note that the standard deviation of v is the turbulence intensity. Fourier components are also of the form $\int \phi(t)v(t)dt$ and therefore Gaussian if $v(t)$ is a Gaussian process. For stationary time series Fourier components are un-correlated, and therefore in fact independent when they are Gaussian. We can therefore regard a Gaussian process as the sum of Fourier components with independent Gaussian amplitudes. For v the amplitude of the zero mode ($\omega = 0$) is identically equal to zero. For u the zero mode is equal to $\bar{u}$, and other Fourier components are certainly not independent of $\bar{u}$, in fact we may expect them to scale with $\bar{u}$. Choosing v instead of u solves this problem. The response characteristics of the anemometer (including amplifiers, analog to digital converters etc.) influence the measured time series. Cup anemometers are for example slightly non-linear which spoils Gaussianity. It is not a large effect, but in order to remove it we always apply a (linear) low pass filter with a cut off frequency below that of the cup anemometer. The response function of a cup anemometer is roughly a linear first order filter of the form $\psi_{\rm cup}(\omega) = \frac{1}{1+i\omega l_{\rm cup}/\bar{u}}$, where $l_{\rm cup}$ is a characteristic length equal to about 1.5m. Thus the response time $l/\bar{u}$ decreases with the (mean) wind speed. Amplifier filters are of course independent of $\bar{u}$ and so is the small amount of noise they generate. All this is removed by applying a fourth order filter to the raw data. The transfer function of the filter is $\psi_l(\omega) = \frac{1}{(1+i\omega l/\bar{u})^4}$, i.e. the spectrum $S(\omega)$ is changed to $S(\omega)|\psi_l(\omega)|^2$. We use a length scale rather than a time scale in order to preserve a possible invariance under scaling of time. We may even prefer to use $s = \bar{u}t$ instead of t as the independent variable. By Taylor's hypothesis $v(s)$ and its Fourier transform $v(k)$, where $k = \omega/\bar{u}$, may then be interpreted as measuring the spatial structure of the turbulence, but, more importantly, $v(s)$ should be completely independent of $\bar{u}$ if we can just assume invariance under time scaling. This is discussed in more detail below.

We shall illustrate the concept of Gaussianity by cup anemometer data from Lammefjord (mast 3, cup anemometer at 10 m) and Oak Creek (mast 1, cup anemometers at 10m and 79m). Lammefjord is among the most perfectly Gaussian sites, while Oak Creek is the most non-Gaussian of the sites referred to above. Descriptions of the sites are found sections B and A. For the Lammefjord data only time series with $\bar{u} > 8$m/s were used, and for the Oak Creek data $\bar{u} > 15$m/s. Furthermore, the Oak Creek data was limited to the sector 320°-360°.

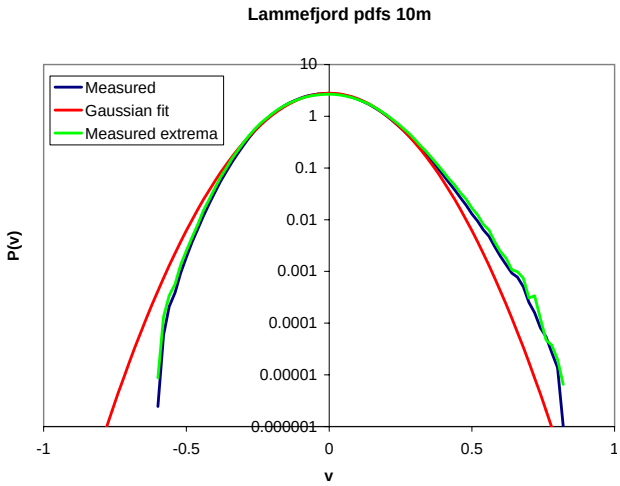

Figure 1. Pdf of v based on time series with $\bar{u} > 8m/s$ from the Lammefjord experiment.

Figure 1 shows the pdf of v evaluated from the Lammefjord data with $l = 4$m. The pdf is close to Gaussian with $K = 3.04$, though somewhat skewed ($S = 0.17$). The turbulence intensity I is 14.3%. We note that the upper tail tends to look exponential rather than Gaussian, and that the Gaussian pdf underestimates the probability of extremely large values by about an order of magnitude.

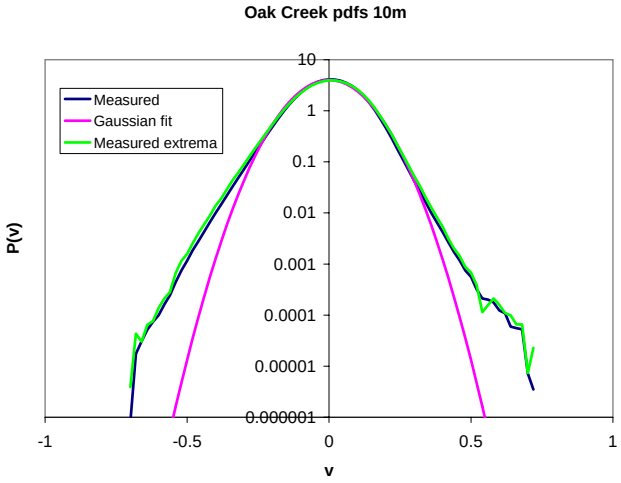

Figure 2. Pdf of v based on time series with $\bar{u} > 15m/s$ from the Oak Creek experiment.

Figure 2 shows the pdf of v at 10m evaluated from the Oak Creek data. The pdf is less Gaussian with $K = 3.50$, but still far from $K = 6$ as for a double sided exponential distribution. The skewness is now negative, $S = -0.11$ and I =10.0%. Here both tails look exponential, and the Gaussian pdf severely underestimates the probability of extremely large as well as extremely low values.

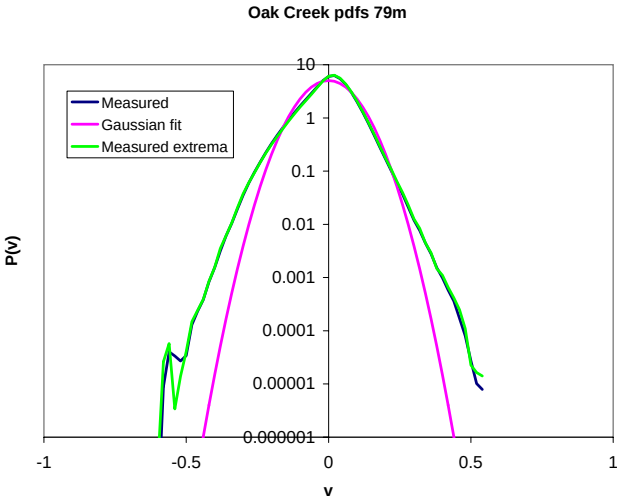

Figure 3. Pdf of v based on time series with $\bar{u} > 15m/s$ from the Oak Creek experiment.

Figure 3 shows the pdf for 79m from the Oak Creek data. This case is even more non-Gaussian with $K = 4.11$, $S = -0.34$ and I =7.9%, and probabilities of extreme values are severely underestimated. Downward peaks in the time series seems frequent. The reason for these could be thermal convection which brings bubbles of hot air up from below (where the wind speed is generally lower).

Table 1 shows the effect of varying the length constant in ψ_l. K and S move towards Gaussian values as l is increased, but it is not very dramatic indicating that the assumption of Gaussianity is better for the larger scales.

Table 1. Variation of I, S and K with the filter length constant l. Oak Creek 10 data.

l	I	S	K
1m	0.111	-0.16	3.54
2m	0.107	-0.15	3.53
4m	0.100	-0.11	3.50
8m	0.091	-0.02	3.44
16m	0.081	0.07	3.40

For a stationary Gaussian process the difference $\Delta v = v(t_2) - v(t_1)$ and the sum $V = (v(t_1) + v(t_2))$ are joint Gaussian. They are in fact independent since $\langle V\Delta v\rangle = \langle v(t_2)^2\rangle - \langle v(t_1)^2\rangle = 0$. Letting $t_2 - t_1 \to 0$ we find that $v(t)$ and $v'(t)$ are independent. In other words, the pdf of extrema ($v(t)$ where $v'(t) = 0$) should be the same as for the whole series. Gaussian or not, the experimental data have that property. The pdfs of the extrema, the green curves in the figures, match the overall pdfs (blue curves) almost perfectly. This is remarkable.

Figure 4 shows pdfs of $\Delta v(t) \equiv v(t + l/\bar{u}) - v(t)$ with $l = 4$m evaluated from the Oak Creek data at 10m. The dark blue curve, almost hidden by the red and the blue ones, is based on all data with $\bar{u} > 15$m/s. The red curve is based on time series where $15\text{m/s} < \bar{u} < 18\text{m/s}$ and the green is for $\bar{u} > 20$m/s. The pdfs are identical showing that it is permissible to pool the data. The light blue curve is the Gaussian fit, which obviously completely misses the exponential tails. With $S_{\Delta v} = 0.23$ and $K_{\Delta v} = 5.54$ the pdf of Δv is even more non-Gaussian than the pdf of v. The standard deviation of Δv, $I_{\Delta v}$, is 3.7%, i.e. substantially lower than I.

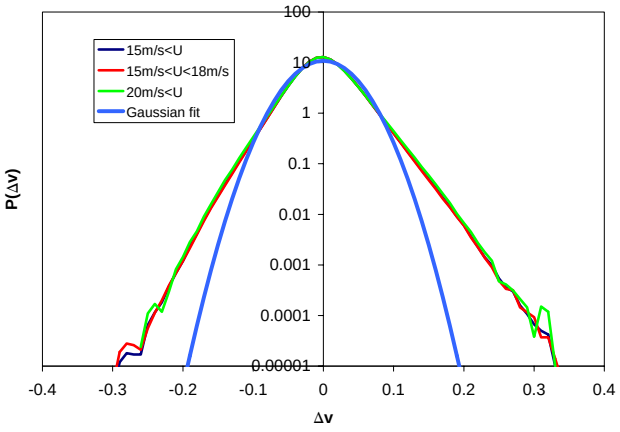

Figure 4. Pdf of Δv based on time series with varying $\bar{u}$. Oak Creek experiment, mast 1, 10m.

Figure 5 is the same as figure 4 except for the Lammefjord data, and looks in fact very similar. The skewness is 0.45 and the Kurtosis is 4.26. There is some discrepancy for different $\bar{u}$, which is mainly due to the fact that all directions were used in order to have a decent number of time series. The surface roughness depends on the wind direction for this site and at the same time direction and $\bar{u}$ are correlated in the data.

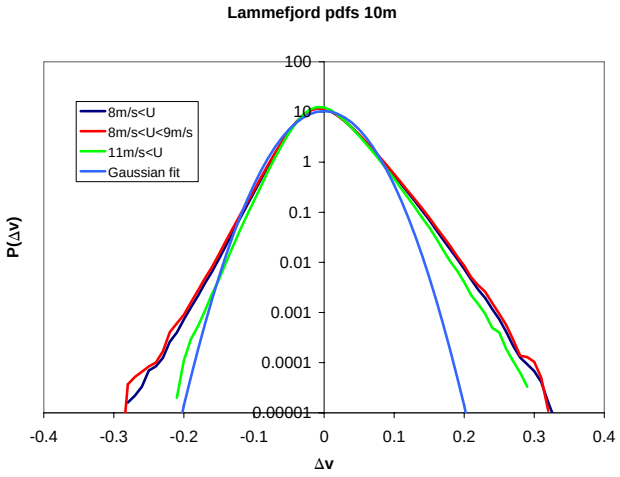

Figure 5. Pdf of Δv based on time series with varying $\bar{u}$. Lammefjord experiment, mast 3, 10m.

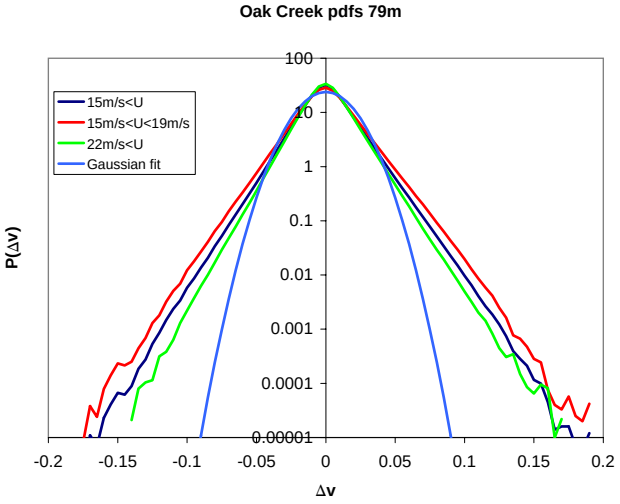

Figure 6. Pdf of Δv based on time series with varying $\bar{u}$. Oak Creek experiment, mast 1, 79m.

Figure 6 is as figure 4 but for the anemometer at 79m. Here the pdf is definitely more exponential than Gaussian ($S_{\Delta v} = 0.16$, $K_{\Delta v} = 5.78$) and values in the tails are orders of magnitude larger than the Gaussian fit. There seem to be no way around exponential tails in this case, and it we do not know of any theory that predicts this. There is a dependence on $\bar{u}$ also, which may reflect the somewhat awkward selection of the time series. In the data set only periods with $\bar{u}$ >15m/s measured at 39m were recorded. From these only time series with $\bar{u}$ >15m/s at both 10m and 79m have been selected here. This means that for the time series where $\bar{u}$ =15m/s at 79m have only been selected if $\bar{u}$ >15m/s both at 39m and at 10m, which represents a rare situation. When the lowest wind speeds are removed the curves collapse.

Table 2 shows the effect of varying the filter length constant l. The analog to the turbulence intensity $I_{\Delta v}$ is generally smaller than I. This is because Δv depends less on long scales than v. In the wave number domain this can be expressed by

$$(\Delta v)(k) = \frac{\mathrm{e}^{ikl} - 1}{(1 + ikl)^4}\, u(k)/\bar{u} \approx \frac{ikl}{(1 + ikl)^4}\, u(k)/\bar{u} = iklv(k) \to 0 \text{ for } k \to 0 \quad (2.1)$$

Thus we apply a band pass filter to u to obtain v, and therefore we should get more

Table 2. Variation of $I_{\Delta v}$, $S_{\Delta v}$ and $K_{\Delta v}$ with the filter length constant l. Oak Creek 10 data.

l	$I_{\Delta v}$	$S_{\Delta v}$	$K_{\Delta v}$
1m	0.026	0.28	5.09
2m	0.032	0.24	4.78
4m	0.037	0.23	4.54
8m	0.038	0.21	4.22
16m	0.036	0.17	3.83

variance of Δv when the filter is moved towards the energy containing part of the spectrum. We also note that $\Delta v \approx l/\bar{u}\frac{dv(t)}{dt}$ must be a very good approximation. For load cases where a regulator is involved $u'(t)$ is more relevant than $u(t)$, see section 6.3, and it can be argued that $I_{\Delta v}$ is a better measure of the impact of the turbulence than I. Another advantage of $I_{\Delta v}$ over I is that ten minute estimates of $I_{\Delta v}$ shows much less scatter than the corresponding values of I. Returning to table 2, we note that $S_{\Delta v}$ varies only slowly with l and seem to approach a value close to the theoretical value $\frac{4}{5}C_{\mathrm{K}}^{-\frac{3}{2}} \sim 0.3$ as $l \to 0$. The kurtosis $K_{\Delta v}$ is consistently higher than 3 and increases as $l \to 0$. In this limit the shape of the pdf (not shown) develops long exponential tails.

Finally some comments on the concept of scaling of time. Suppose that the wind field $\boldsymbol{v}(\boldsymbol{x}, t)$ is an exact solution to the Navier-Stokes equations for the boundary layer. For any 'speed-up factor' α we can define a new time scaled velocity

$$\tilde{\boldsymbol{v}}(\boldsymbol{x}, t) \equiv \alpha \boldsymbol{v}(\boldsymbol{x}, \alpha t) \tag{2.2}$$

It turns out that $\tilde{\boldsymbol{v}}$ is also a solution to the Navier-Stokes equations (together with scaled density and temperature, e.g. $\tilde{\rho}(\boldsymbol{x}, t) \equiv \rho(\boldsymbol{x}, \alpha t)$). However, in the equations the viscosity needs to be changed to $\alpha\nu$, the acceleration of gravity to $\alpha^2 g$ and the Coriolis parameter to αf. Cloud formation and chemistry in general is unaffected by the time scaling as long as it is governed by equilibrium thermodynamics. Non-equilibrium properties (e.g heat flux and chemical reaction rates) are altered by the scaling. There can be good reasons to believe that the properties that change under time scaling are not very important. Firstly, since we are in the high Reynolds number limit the value of ν is immaterial as long as its value is small. Secondly, gravity mostly plays a role when there are density differences present, which is the case for stable or unstable conditions. An exception is off shore locations where g also affects wave dynamics and thereby the surface roughness. On shore and for neutral conditions, which are relevant at high wind speeds, the value of g should not matter. Thirdly, the Coriolis parameter determines the thickness of the boundary layer and it is also linked to the length of the day. Changing f would surely change the whole climate. However, the neutral surface layer can be regarded as being in a state of quasi equilibrium defined mainly by the terrain, the average wind speed and direction, and these parameters are not changed by the time scaling. This is evident from mean wind profiles which are found to scale with u_*. Above the surface layer, i.e. more than a few tens of meters above the ground, the Coriolis force tends to gradually change the logarithmic profile into a more constant profile. Therefore time scaling can be expected to fail somewhere above the surface layer, perhaps at the hub hight of a large wind turbine. Even if time scaling works for mean wind profiles, it may not work for the turbulence. In particular we need know if it works for gust events.

Extreme gusts are rare having recurrence times of perhaps several years. Even if several years of data is available, it may therefore contain preciously few events, or none at all. Predicting extreme gusts will therefore involve some kind of extrapolation from less severe events. Time scaling is an obvious candidate for such

an extrapolation. The idea is to keep climatology out of the scaling by considering only relatively short time scales. The distribution of ten minutes mean wind speeds is traditionally used to define the wind climate and each ten minute time series is regarded as a piece of an ideal, stationary time series. The ten minutes mean velocity $\bar{u}$ is used to scale so that $u/\bar{u}$ or $(u-\bar{u})/\bar{u}$ is used instead of u, and where time us relevant time it is scaled as $\bar{u}t/z$. It could be argued that the averaging period (the ten minutes) should vary with $\bar{u}$, but the effect of neglecting this is usually rather small. Filtering is more important, in particular when it comes to measured peak values, which are sensitive to the response and noise characteristics of the instrument and the data acquisition system. This introduces averaging times which do not take part in the scaling. In order to compare results for different $\bar{u}$ we need to apply a low pass filter with a time constant inversely proportional to $\bar{u}$. The cut off frequency should be somewhat below the cut off frequencies of the instrument and the amplifier.

3 Simulation of turbulence

Developing methods for turbulence simulation it is convenient to operate with Gaussian variables, since these may be added and the sum is still Gaussian. Fortunately, the Gaussian probability distribution is a reasonable approximation for atmospheric turbulence or at least a good starting point. The chosen methods are based on the fast Fourier transform (FFT), and this chapter presents methods for multiple correlated time series.

An alternative method, applied in some of the examples in chapter 6, simulates 3D turbulence fields by 3D Fourier simulations, as described in detail by Mann (1998).

3.1 Basic Fourier simulation

Any linear combination of a set of Gaussian variables will produce a new Gaussian variable. This imply that Fourier transformation will map Gaussian time series onto Gaussian spectral representations and vice versa, allowing us to simulate a stationary process in frequency domain $X(f)$ and subsequently transform it into time domain $x(t)$ by inverse FFT (Press, Flannery, Teukolsky & Vetterling 1992). This is done by

$$x(t) = \sum_{k=0}^{M} X_k e^{\mathrm{i}\cdot k\Delta f t} \tag{3.1}$$

where M is the length of the time series, which must be a power of 2 to take advantage of the efficient FFT algorithm (Press et al. 1992). When time series of arbitrary lengths are needed, the most efficient strategy is to increase M to the next power of two and disregard the extension of the simulated series. The Fourier modes are random, and their ensemble averaged variance should match the empirical power spectrum $S(f)$.

$$X_k = \begin{cases} \mu & \text{for} \quad k = 0 \\ \sqrt{S(k\Delta f)}\sqrt{\Delta f}\, y_k & \text{for} \quad k = 1 \ldots M/2 \end{cases} \tag{3.2}$$

Here, the basic frequency step is defined by the duration of the time series $\Delta f = 2\pi/T$, and y_k is a set of independent pseudo-random Gaussian variables with zero mean and unit variance, e.g. generated by the Box-Müller algorithm (Press et al. 1992). In general, a real time series will have a complex Fourier transform,

so the input variables y_k must be complex. Real series do, however, obey the symmetry $X(-f) = X(f)^*$, where $(\cdot)^*$ denotes complex conjugation, and with the 'wrap-around' data organization applied by the FFT algorithm of Press et al. (1992). We therefore supply $X_k = X^*_{M+1-k}$ for $k > M/2$.

The Fourier simulation method is widely used, but it should be noted that there are choices to be made. Some modelers supply random input with fixed amplitudes and random phases, although Grigoriu (1993) recommends the use of complex (2D) gaussian input, which will ensure a truly gaussian process. The load simulation program FLEX (Øye 1992) and its turbulence simulator VINDSIM normalize the simulated time series such that each simulation matches the prescribed variance exactly. This choice may be convenient in the context of aeroelastic simulations, but the block variance of a finite sample of a stationary process should actually be variable. Furthermore, sampled time series are rarely cyclic and their trends are often more significant than in the time series simulated as above. If realistic trends are important, one should simulate time series longer than the required output and only use part of the series.

3.2 Simulation of correlated signals

To simulate turbine dynamics one usually require spatially distributed wind loads. These loads are linked to turbulent velocities, and one way to represent these is by multiple time series representing turbulence at selected nodes on the rotor plane (e.g. Veers 1988). Furthermore, turbulence simulators operating with fields, rather than a set of correlated single-point signals, may work with correlated velocity components (e.g. Mann 1998).

Karhunen-Loève expansion

The Karhunen-Loève expansion is a robust method for generating correlated variables (Johnson 1994). The modelled variables are organized as the vector $\mathbf{x}$ of dimension N with the mean vector μ and the $N \times N$ dimensional covariance matrix $\mathbf{C}$. The covariance matrix is decomposed as

$$\mathbf{C} = \mathbf{W} \cdot \mathbf{\Lambda} \cdot \mathbf{W^T}, \tag{3.3}$$

where $\mathbf{\Lambda}$ is a diagonal matrix consisting of eigenvalues of $\mathbf{C}$, and $\mathbf{W}$ is a square matrix with corresponding eigenvectors organized in columns in the same order as the eigenvalues in $\mathbf{\Lambda}$. The notation $\mathbf{W^T}$ indicates the transposed of the $\mathbf{W}$ matrix. With the aid of the N-dimensional vector $\mathbf{y}$, composed of uncorrelated variables from the standard normal distribution $\mathrm{N}(0, 1)$, the correlated variables $\mathbf{x}$ are simulated by

$$\mathbf{x} = \mu + \mathbf{W} \cdot \sqrt{\mathbf{\Lambda}} \cdot \mathbf{y}, \tag{3.4}$$

or

$$x_i = \mu_i + \sum_{j=1}^{N} w_{ij} \sqrt{\lambda_j} y_j. \tag{3.5}$$

A numerical solution to the eigenvalue problem $\mathbf{C} \cdot \mathbf{x} = \lambda \mathbf{x}$, where $\mathbf{C}$ is a symmetric matrix, is provided by Householder's reduction to tridiagonal form followed by implicit QL decomposition. Press et al. (1992) document these algorithms for real symmetric matrices, and the EISPACK computer library provides generalized versions for Hermitian symmetric ones. The need for the latter extension is discussed below.

Fourier simulation of multiple time series

To extend Fourier simulation method for multiple series, we first note that the cross-correlation function of two processes are mirrored in time $\rho_{ij}(\tau) = \rho_{ji}(-\tau)$. This symmetry imply that the corresponding cross spectrum will have a Hermitian symmetry $\chi_{ij}(f) = \chi^*_{ji}(f)$, where $(\cdot)^*$ indicates complex conjugation. The cross-spectral matrix is therefore Hermitian symmetric, i.e. equal to its transposed and complex conjugated. Therefore, we use complex algebra for the decomposition $\chi(f) = \mathbf{W}(f) \cdot \sqrt{\mathbf{\Lambda}(f)} \cdot \mathbf{W}^*(f)$, where $\mathbf{W}^*$ is the Hermitian conjugate of $\mathbf{W}$ rather than the transposed real matrix $\mathbf{W^T}$ sufficient for real matrices. To simulate the time series $x_i(t)$ in a set of N correlated ones, we decompose the cross-spectral matrix for each frequency $f = k\Delta f$ and find the Fourier coefficients

$$X_{ik} = \begin{cases} \mu_i & \text{for} \quad k = 0 \\ \sum_{j=1}^{N} w_{ijk} \sqrt{\lambda_j} \sqrt{\Delta f} y_{jk} & \text{for} \quad k = 1 \ldots M/2 \\ X_{ik} = X^*_{i,M+1-k} & \text{for} \quad k = M/2+1 \ldots M \end{cases} \tag{3.6}$$

It is possible to improve the computational efficiency of the Fourier transformation, by knowledge of the symmetries for real series, see Press et al. (1992).

Cholesky decomposition

A proper covariance or cross-spectral matrix is positive definite, i.e. all of its eigenvalues λ_i are positive. This condition allows matrix decomposition by the Cholesky method, which results in

$$\mathbf{C} = \mathbf{L} \cdot \mathbf{L^T}, \tag{3.7}$$

where $\mathbf{L}$ is a lower triangular matrix. The standard version for real symmetric matrices (Press et al. 1992) is easily extended for Hermitian symmetric matrices, such as the general cross-spectral matrix $\chi(f) = \mathbf{L}(f) \cdot \mathbf{L}^*(f)$.

$$l_{ij} = \frac{\chi_{ij} - \sum_{k=1}^{j-1} l_{ik} l^*_{jk}}{\sqrt{\chi_{jj} - \sum_{k=1}^{j-1} l_{jk} l^*_{jk}}}, \qquad 1 \le j \le i \le n. \tag{3.8}$$

The correlated Fourier modes are simulated by

$$X_{ik} = \begin{cases} \mu_i & \text{for} \quad k = 0 \\ \sum_{j=1}^{i} l_{ijk} \sqrt{\Delta f} y_{jk} & \text{for} \quad k = 1 \ldots M/2 \\ X_{ik} = X^*_{i,M+1-k} & \text{for} \quad k = M/2+1 \ldots M. \end{cases} \tag{3.9}$$

Note, that the summation is shorter than in equation 3.6, since the matrix $\mathbf{L}$ is triangular. Compared to eigenvector decomposition, Cholesky decomposition is twice as fast and easier to implement.

Computational tricks

When simulating N time series of length M, the execution times for FFT and 'square-root' matrix decomposition are proportional to $N\,M \log_2 M$ and $N^3 M$, respectively. Thus, with the large number of time series needed for aeroelastic simulations (say $N > 100$), matrix decomposition becomes the most demanding task, and it is relevant to consider approximate speed-up methods.

- The computational work and memory requirements are reduced by a factor of two if we operate with real matrices instead of complex ones. This simplification is made in the VINDSIM implementation of Veers's (1988) model distributed with FLEX(Øye 1992). The disadvantage is that it prevents simulation of systematic phase lag between series, as in a sheared boundary layer

where turbulence features tend to hit the top of the rotor plane before the bottom (Mann 1998).

- With a simulation grid of regular geometry it is usually possible to arrange the nodes into subsystems of similar geometry, leading to many symmetries in the correlation matrix. As an example, a cartesian grid arranged as vertical profiles with equidistant lateral separation, could have its nodes numbered from the bottom, mast by mast across the wind direction. The cross-spectral matrix for this system has identical submatrices arranged in bands parallel to the diagonal, and it is possible to decompose it by fast methods based on block-matrix operations (Gallivan, Thirumalai, Dooren & Vermaut 1996). If the polar grid of Veers's (1988) model is arranged as radial distributions repeated for equidistant azimuth angles, the coherence matrix becomes a circulant symmetric block matrix, which has even faster decomposition methods (Winkelaar 1991). In a sheared boundary-layer, the phase-lag between signals do however have a vertical rather than radial dependency, so the latter method is only practical when phase information is neglected.

- A simple model for spectral coherence (Davenport 1977) is the exponentially decaying function $\mathrm{Coh}(f) = \exp(-cf\Delta/u)$, where c is a constant and Δ is the spatial separation. If we assume that the power spectrum is spatially independent, we see that the limits values of Cholesky decomposition matrix are

$$L(f) \to \sqrt{S(f)\Delta f} \begin{bmatrix} 1 & 0 & & 0 \\ 1 & 0 & & 0 \\ \vdots & & \ddots & \\ 1 & 0 & & 0 \end{bmatrix} \quad \text{for } f \to 0 \quad \text{(full correlation)}$$

and

$$L(f) \to \sqrt{S(f)\Delta f} \begin{bmatrix} 1 & 0 & & 0 \\ 0 & 1 & & 0 \\ \vdots & & \ddots & \\ 0 & 0 & & 1 \end{bmatrix} \quad \text{for } f \to \infty \quad \text{(zero correlation)}$$

The variation between these limits is smooth and monotonic. Therefore, it is sufficient to decompose matrices for a limited number of frequencies and use interpolated values for simulation, as also done in VINDSIM (Øye 1992). If we decompose at a fixed number of frequencies per decade, the work load is reduced to $\propto N^3 \log_2 M$. Additional work of setting up cubic-spline interpolations (see appendix D) between the decomposed matrices and doing these interpolations are $\propto N^2 \log_2 M$ and $\propto N^2 M$, respectively. In practice ($N > 100$, $M > 1000$) there is a significant improvement compared to the decomposition at every frequency ($\propto N^3 M$).

- The eigenvalues used in the Karhunen-Loève expansion are measures of the variance distributed on the corresponding eigenvectors, and it has been suggested to truncate the sum in equation 3.5 to eigenvectors representing say 99% of the total variance (Di Paola & Gullo 2001). The benefit of truncation is most significant with correlated variables, which in the context of turbulence means the lowest frequencies in the spectrum. Fourier simulation operates with a linear distribution of frequencies, and Appendix C suggest that in practise truncation of the Karhunen-Loève expansion, will not benefit Veers' model significantly.

3.3 Non-Gaussian simulation

Several techniques have been suggested for simulation of non-Gaussian processes – see e.g. the review article by Gurley, Tognarelli & Kareem (1997) or the book of Grigoriu (2000). In the context of Fourier simulation, the methods are often based on memoryless transformation from auxiliary Gaussian processes to non-Gaussian ones $x_i(t) \rightarrow u_i(t)$. This is expressed by the function

$$u_i(t) = g_i[x_i(t)], \tag{3.10}$$

where index i refers to one of several series, i.e. the non-Gaussian effect need not be spatially homogeneous. The probability distributions of the target and auxiliary processes are linked to each other by

$$p_{u,i}(u) = \varphi(x)\left|\frac{dx}{du_i}\right|, \tag{3.11}$$

where $\varphi(x) = (2\pi)^{-1/2}\exp(-x^2/2)$ is the probability density function of the standard Gaussian process. It is practical when the translation is a monotonic non-decreasing function $d\,g_i(x)/dx \geq 0$, since with this assumptions the transformation is provided by the inverse of the cumulated probability distribution of the target process $F_{i,T}^{-1}(u)$.

$$g_i[x_i(t)] = F_{i,T}^{-1}[\phi[x_i(t)]] \tag{3.12}$$

Here $\phi(x) = \frac{1}{2}\left(1 + \mathrm{erf}\,(x/\sqrt{2})\right)$ is the cumulated probability function of the standard Gaussian process.

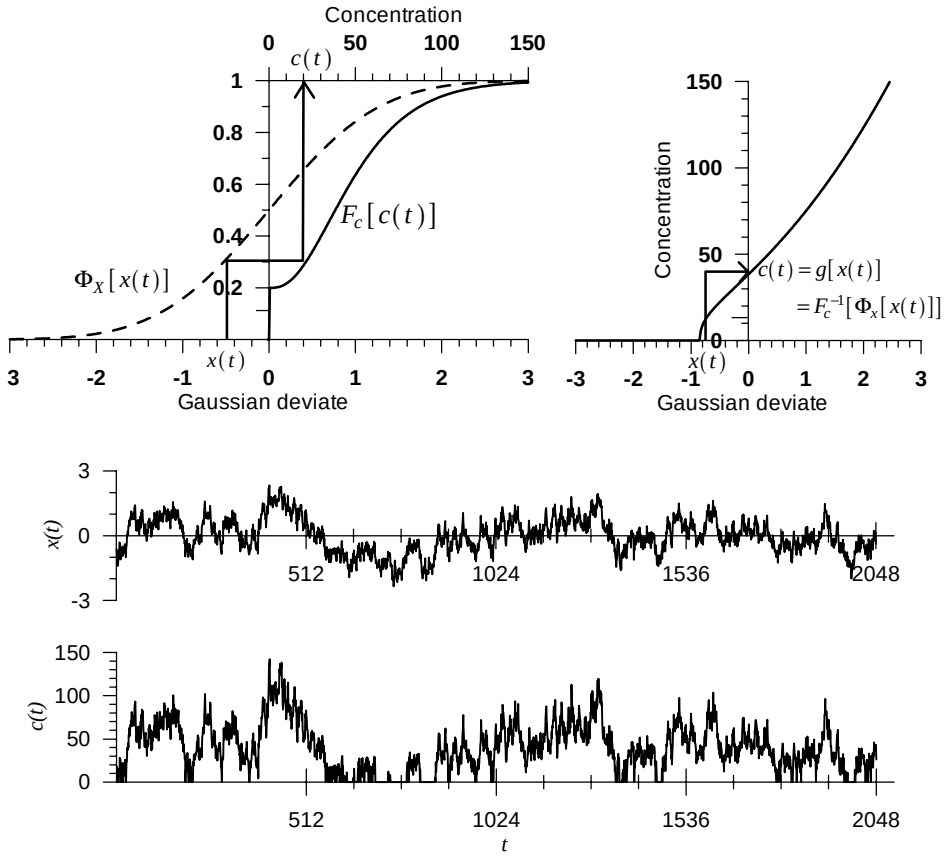

Figure 7. Sketch of relationship between correlation functions of Gaussian and transformed variables.

Figure 7 illustrates the method by an example taken from another application, in which the task was to model concentration fluctuations in a gas plume (Nielsen, Chatwin, Jørgensen, Mole, Munro & Ott 2002). This is an intermittent process, and the probability density function was modelled by a Gamma distribution for the non-zero part of the signal. The cumulated probability functions are shown in the upper-left frame of the figure, and the mapping function $g(x)$, constructed by these, is shown in the upper-right frame. An auxiliary Gaussian time series and the corresponding non-Gaussian one are shown in the lower frames of the figure. Because of the monotonic translation function, the local fluctuations in the two series are similar, even though their probability distributions are quite different. Atmospheric turbulence is nearly Gaussian, so for wind energy applications we need less dramatic transformations.

Correlation distortion

A difficulty of the transformation $u = g(x)$ is that it distorts the correlation function. There are several ways to overcome this problem, e.g. Seong & Peterka (1997) or Gurley, Kareem & Tognarelli (1996), and an iterative approach was adopted in a previous EFP project (Nielsen, Hansen & Pedersen 2000a). However, in the following we focus on a more efficient method known as correlation distortion (e.g. Gioffrè, Gusella & Grigoriu 2000). The basic idea is to model the distortion of the translation process and adjust autocorrelations and cross correlations of the auxiliary Gaussian processes, such that correlations of non-Gaussian processes becomes correct after translation. Cross-correlation functions of Gaussian processes $\rho_{x_i x_j}(\tau)$ and non-Gaussian ones $\xi_{u_i u_j}(\tau)$ are related to each other by a double integral involving the translation functions $g_i(x_i)$ and $g_j(x_j)$.

$$\sigma_i \sigma_j \xi_{ij}(\tau) = \int_{-\infty}^{\infty} \int_{-\infty}^{\infty} [g_i(x_i) - \mu_i][g_j(x_j) - \mu_j] \cdot \varphi_{2\mathrm{D}}(x_i, x_j \,|\rho_{ij}(\tau)) \, dx_i dx_j \,. \tag{3.13}$$

Here, μ_i and σ_i are the non-Gaussian mean and standard deviation, and

$$\varphi_{2\mathrm{D}}(x_i, x_j \,|\rho_{ij}) = \frac{1}{2\pi\sqrt{1-\rho_{ij}^2}} \exp\left[-\frac{x_i^2 + x_j^2 - 2\rho_{ij} x_i x_j}{2(1-\rho_{ij}^2)}\right]$$

is the joint Gaussian distribution with correlation coefficient ρ_{ij} and marginal distribution $\varphi(x)$. The general procedure is to evaluate the double integral in equation 3.13 with suitable accuracy for the entire range of Gaussian correlation values $\rho_{ij} \in [-1, +1]$, and then subsequently search the result table for the Gaussian correlation $\rho_{ij}(\tau)$, which matches specified target correlations $\xi_{ij}(\tau)$. Knowing the cross-correlation functions of the Gaussian variables, Gioffrè et al. (2000) obtained cross-spectra of corresponding Gaussian processes $\chi_{ij}(f)$ by FFT, simulated correlated Gaussian times series as above, and finally translated these into non-Gaussian time series by individual translations.

Figure 8 sketches a relation between the correlations of corresponding Gaussian and non-Gaussian processes, based on the transformation in Figure 7. This relation is an increasing function, which passes the point of zero correlation $(\rho, \xi) = (0, 0)$. The upper limit will reach perfect correlation $\xi_{\max} = 1$ only if the two translation functions are equal $g_i[x] = g_j[x]$. For the lower limit to reach the case of perfect anti-correlation $\xi_{\min} = -1$ the translation functions must both be equal and symmetrical around the mean value, i.e. $g_i[-x_i] - \mu_i = -(g_j[x_j] - \mu_j)$. If the target processes has positive skewness, the lower limit will deviate more from perfect anti-correlation ($\xi = -1$) than the upper limit will deviate from perfect

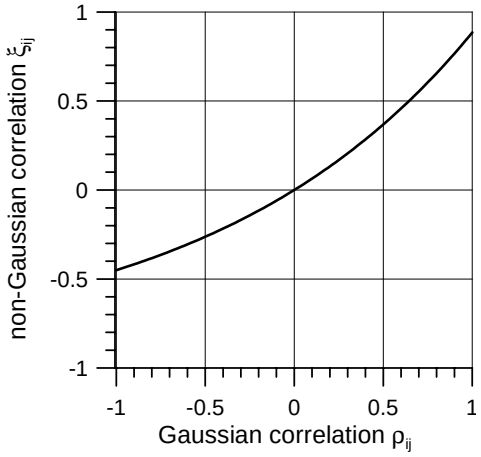

Figure 8. Sketch of relationship between correlation functions of Gaussian and non-Gaussian variables.

correlation ($\xi = 1$), as indicated in the Figure. The main point is that the possible range of correlation values of the simulated processes $[\xi_{\min}, \xi_{\max}]$ is restricted, when their probability distributions differ. This restriction must not be violated for any signal pair at any time delay $\xi_{ij}(\tau)$. Furthermore Gioffrè et al. (2000) warn that the target Gaussian correlation matrix should be non-negative definite for all time delays or, equivalently, that cross-spectral matrices should be non-negative definite for all frequencies.

Features and limitations

Fourier simulation with correlation distortion reproduce

- marginal probability distributions of individual time series, and
- power spectra and cross-spectra of time series pairs.

Reproduction of specified probability distributions ensures correct signal intermittency and statistical moments of individual series. The specified cross-spectra ensures correct second-order statistics, i.e. power spectra, autocorrelation functions and cross correlations. Time lags between processes, equivalent to asymmetric correlation functions, are included in the concept, whereas higher-order spectral statistics are unspecified. Statistics of time derivatives are only correct to second order, so individual simulated series will be *symmetric* in time.

Computational tricks

- Direct numerical evaluation of the double integral in Equation 3.13 is computational expensive and, unfortunately, it is needed for all possible signal pairs and time lags. To simulate a general non-Gaussian process efficiently by computer it is necessary to find the correlation function of the auxiliary processes by a faster method. Therefore, we approximate the translation function $g_i(x)$ by a series of Hermite polynomials.

  $$\tilde{g}_i(x) = \sum_{n=1}^{N} a_{in} \mathrm{He}_n(x). \tag{3.14}$$

  Using special properties of the Hermite polynomials (i.e. the orthogonality and diffential rules, see Table 3) Grigoriu (2000) found a maximum likelihood

estimate of the coefficients of the expansion

$$a_{in} = \frac{1}{n!} \int_{-\infty}^{\infty} \left[g_i \left\{ x \right\} - \mu_i \right] \mathrm{He}_n \left(x \right) \varphi \left(x \right) dx \tag{3.15}$$

Inserting the Hermite expansions (equation 3.14) in the general relation between the correlations of Gaussian and non-Gaussian processes (equation 3.13), and using the orthogonality of Hermite polynomials, the following simple expression for the correlation distortion was found.

$$\sigma_i \sigma_j \xi_{ij} \simeq \sum_{n=1}^{N} \frac{a_{in} a_{jn}}{n!} \rho_{ij}^n \tag{3.16}$$

The number of terms needed for sufficiently accurate approximation depends on how much probability distribution of the target processes deviate from a Gaussian distribution. As a accuracy check we observe that equation 3.13 simplifies to one-dimensional integrals in the special cases of perfect correlation ($\rho = 1$) and perfect anti-correlation ($\rho = -1$).

$$\sigma_{c_i} \sigma_{c_j} \xi_{ij} = \int_{-\infty}^{\infty} \left[g_i \left\{ x \right\} - \mu_i \right] \left[g_j \left\{ \pm x \right\} - \mu_j \right] \varphi \left(x \right) dx, \quad \text{for } \rho = \pm 1 \tag{3.17}$$

For these special cases, $\rho = \pm 1$, the degenerated version of equation 3.13, expressed in equation 3.17, can be compared with

$$\sigma_i \sigma_j \xi_{ij}^{\min} \simeq \sum_{n=1}^{N} \left(-1 \right)^n \frac{a_{in} a_{jn}}{n!} \quad \text{and} \quad \sigma_i \sigma_j \xi_{ij}^{\max} \simeq \sum_{n=1}^{N} \frac{a_{in} a_{jn}}{n!} \tag{3.18}$$

Modelling correlation distortion by equation 3.16 with ten terms is usually quite accurate, even though the Hermite expansion $\tilde{g}_i(x)$ may be a relatively poor approximation of the translation process $g_i \left[x_i \left(t \right) \right] = F_{i,T}^{-1} \left[\phi \left[x_i \left(t \right) \right] \right]$. For conversion of auxiliary Gaussian series to the non-Gaussian ones we must of course use accurate translation functions.

Table 3. Some properties of Hermite polynomials.

Definition:	$\mathrm{He}_n(x) = \frac{(-1)^n}{\varphi(x)} \frac{d^n \varphi(x)}{dx^n}$
Low-order polynomials:	$\mathrm{He}_0(x) = 1$ $\quad$ $\mathrm{He}_3(x) = x^3 - 3x$ $\mathrm{He}_1(x) = x$ $\quad$ $\mathrm{He}_4(x) = x^4 - 6x^2 + 3$ $\mathrm{He}_2(x) = x^2 - 1$ $\quad$ $\mathrm{He}_5(x) = x^5 - 10x^3 + 15$
Recurrence:	$\mathrm{He}_{n+1}(x) = x\mathrm{He}_n(x) - n\mathrm{He}_{n-1}(x)$
Derivation:	$\mathrm{He}_n'(x) = n\mathrm{He}_{n-1}(x)$
Orthogonality:	$\int_{-\infty}^{\infty} \mathrm{He}_n(x)\mathrm{He}_m(x)\varphi(x)\,dx = n!\delta_{nm}$

- Two decomposition methods were presented in Section 3.2, and the Cholesky decomposition was judged to be twice as fast with only half of the memory of the Karhunen-Loève expansion. The only reason to bother about the latter is its robustness. When we transform correlation functions as above and make

Fourier transformation of these, there is a risk of spoiling the positive definiteness of the correlation matrix at some frequencies. The problem may arise from insufficient numerical precision, or we could have asked for an impossible case of high correlation and substantially different probability distributions. A pragmatic approach is simply to ignore the problem and apply Karhunen-Loève expansion. Alternatively, we may correct spoiled or improper matrices by the following steps (van der Geest 1998):

1. Substitute all negative elements of the spectral matrix by a small positive number, producing the modified spectral matrix $\tilde{\mathbf{\Lambda}}$;
2. Calculate the guaranteed positive definite matrix $\chi' = \mathbf{W} \cdot \tilde{\mathbf{\Lambda}} \cdot \mathbf{W}^*$;
3. Calculate $\tilde{\chi} = \mathbf{C} \cdot \chi' \cdot \mathbf{C}$ where $\mathbf{C}$ is a diagonal matrix composed by the correction factors $c_{ii} = \sqrt{\chi_{ii}/\chi'_{ii}}$.

When the correction in the first step is small, the second step will only be a slight modification of the original matrix. The corrections in the last step – optional and not suggested by van der Geest (1998) – restores the original diagonal elements, i.e. variances of the simulated processes are preserved at the expense of larger covariance deviations. In Section 3.5 we really need the Cholesky decomposition to work, and in this case we will decompose the corrected matrix $\tilde{\chi}= \tilde{\mathbf{L}} \cdot \tilde{\mathbf{L}}^*$.

- A translation function, $g_i(x_i)$, has been used to describe the correlation-distortion method. However, we do not necessarily need an analytical function, which might be unknown or inconvenient for computation. Instead we may calculate cumulated probability distribution of sampled data by the Quicksort routine (Press et al. 1992) and evaluated the integrals in equation 3.15 by

$$a_{ik} = \frac{1}{n!} \sum_{k=1}^{M} u_i[k] \, \mathrm{He}_n(x_k) \, \varphi(x_k) \frac{1}{M} \quad \text{with} \quad x_k = \Phi^{-1}\left(\frac{k-1/2}{M}\right), \tag{3.19}$$

where the inverse of the cumulated normal distribution is given by the inverse error function $\Phi^{-1}(p) = \sqrt{2}\,\mathrm{erf}^{-1}(2p-1)$ for $0 < p < 1$. Finally, the rank of each point in the simulated Gaussian series are found by Quicksort, and we look up the corresponding non-Gaussian value. A drawback of this procedure is that the non-Gaussian probability distributions will be exactly the same in each simulation, which is not realistic.
When the correct translation function $g_i(x_i)$ is used, the individual probability distribution will be random, but their ensemble averages will match the target.

Winterstein transformation

A third-order polynomial is one of the simplest non-decreasing transformation possible, and we may express it by Hermite polynomials.

$$\tilde{g}_i(x_i) = a_i \, x_i + b_i \, (x_i^2 - 1) + c_i \, (x_i^3 - 3x_i) \tag{3.20}$$

If we further scale the target process to zero mean and unit variance, it is possible to relate the moments of the non-Gaussian and Gaussian processes to each other (Ditlevsen, Mohr & Hoffmeyer 1996).

$$\begin{aligned} 1 &= a_i^2 + 2\,b_i^2 + 6\,c_i^2 \qquad (3.21)\\ S_{u,i} &= 2\,b_i \, \left(2 + a_i^2 + 18\,a_i\,c_i + 42\,c_i^2\right) \\ K_{u,i} &= 15 - 12\,a_i^4 + 288\,a_i\,c_i - 264\,a_i^3\,c_i \\ &\quad +936\,c_i^2 - 864\,a_i^2\,c_i^2 - 432\,a_i\,c_i^3 - 2808\,c_i^4 \end{aligned}$$

The coefficients in these relations are determined by moments of the standard Gaussian variable $x \in \mathrm{N}(0,1)$.

$$E\{x^n\} = \begin{cases} 0 & \text{for odd } n \\ n!! & \text{for even } n \end{cases} \qquad \text{where} \quad n!! = n(n-2)(n-4)\ldots \tag{3.22}$$

By numerical solution of equations 3.21 it is possible to design the transformation in equation 3.20 for a match with specified skewness and kurtosis. This is done by Newton-Raphson iteration where the initial guess could be the approximate solution originally suggested by Winterstein (1988).

$$\begin{array}{l} a = 1/\alpha \\ b = b'/\alpha \\ c = c'/\alpha \end{array} \qquad \text{with} \quad \begin{cases} b' = S(4 + 2\sqrt{1 + 1.5\,(K-3)})^{-1} \\ c' = (\sqrt{1 + 1.5\,(K-3)} - 1)/18 \\ \alpha = \sqrt{1 + 2\,b'^2 + 6\,c'^2}. \end{cases} \tag{3.23}$$

With Winterstein transformations of two processes correlation-distortion formula in equation 3.16 simplifies to a third order polynomial.

$$\xi_{u_i u_j}(\tau) = a_i a_j \rho_{x_i x_j}(\tau) + 2 b_i b_j \rho^2_{x_i x_j}(\tau) + 6 c_i c_j \rho^3_{x_i x_j}(\tau). \tag{3.24}$$

Unfortunately, it is not possible to find a solution for every combination of S and K without violation of the requirement of a monotonic increasing translation function.

$$\frac{d\,g_i(x)}{dx} > 0 \Rightarrow a_i + 2 b_i x + 3 c_i (x^2 - 1) > 0 \tag{3.25}$$

Combined with variance normalization, $a_i^2 + 2b_i^2 + 6c_i^2 = 1$, this gives the following solutions

$$\begin{array}{l} a_i = \sqrt{1 + 21 c_i^2} - 3 c_i \\ b_i = \pm\sqrt{3 c_i (\sqrt{1 + 21 c_i^2} - 6 c_i)} \end{array} \qquad \text{for} \quad c_i \in [0, 1/\sqrt{15}] \tag{3.26}$$

The heart-shaped curve in Figure 9 was produced by insertion of these combinations in the expressions for skewness and kurtosis, equation 3.21. The fat line in the figure is the transformation $g(x) = x + a(x^2 - \langle x^2 \rangle)$, which was applied in a study on the errors in turbulence measurements of finite sample duration, representative for airborne measurements in the convective boundary layer (Lenschow, Mann & Kristensen 1994). The wing-shaped curve represents a compound distribution of two Gaussian variables $p(X) = \alpha p_1(X) + (1-\alpha) p_2(X)$ with $X_1 \in N(\mu_1, \sigma_1)$, $X_2 \in N(\mu_2, \sigma_2)$, $\alpha \in [0\ldots]$, choosing $\mu_1 = 8$m/s, $\sigma_1 = 1.4$m/s, $\mu_2 = 10$m/s, and $\sigma_2 = 0.7$m/s. This distribution could represent conditions downstream of a wind turbine, where wake meandering is expected to produce episodes of reduced wind speed and enhanced turbulence. This probability distribution is shown on the left-hand side of Figure 10 for a range of intermittency factors α. The right-hand side of the figure shows Winterstein transformations matching the mean, standard deviation, skewness, and, when possible, also the kurtosis of the compound Gaussian distribution. We see that the Winterstein transformation may produce long tails, but it cannot be bimodal.

Non-Gaussian acceleration

In many situations velocity perturbations are nearly Gaussian, while velocity increments Δu over a time step Δt have a non-Gaussian distribution (Dutton & Højstrup 1976); in other words, the wind speed signal tend to rise or fall faster than it falls. Synthetic time series of this nature are feasible with non-Gaussian simulation of series of velocity increments followed by summation. Assuming that velocity increments are uncorrelated for long time lags, the integrated velocity

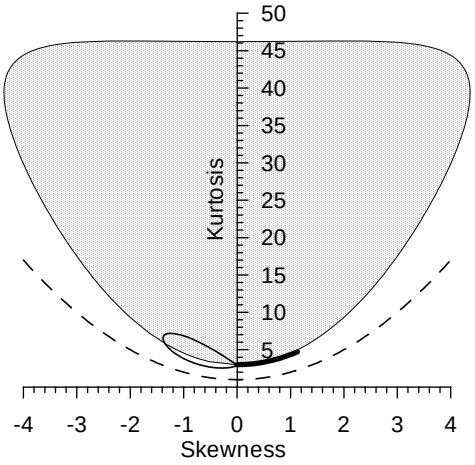

Figure 9. Combinations of skewness and kurtosis feasible with various transformations, i.e. Winterstein transformation (heart-shaped area), the transformation of Lenschow et al (1994) (fat line), and the compound Gaussian distribution (thin line) specified in the text. Also shown is the lower boundary of all distributions (dashed line).

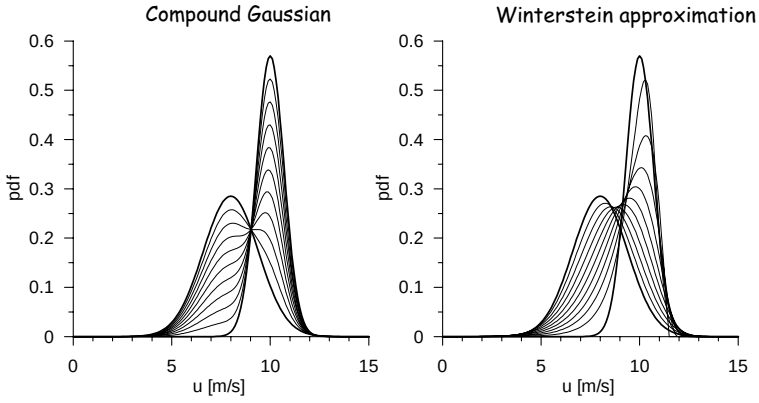

Figure 10. A family of compound Gaussian probability distributions $p(X) = \alpha p_1(X) + (1-\alpha)p_2(X)$ *with* $X_1 \in N(8\text{m/s}, 1.4\text{m/s})$, $X_2 \in N(10\text{m/s}, 0.7\text{m/s})$ *(left) and Winterstein approximations of these (right).*

signal will be asymptotically Gaussian, due to the central-limit theorem. The correlation function for velocity increments is linked to the correlation function of the process itself

$$\rho_{\Delta u_i \Delta u_j}(\tau) = 2\rho_{u_i u_j}(\tau) - \rho_{u_i u_j}(\tau + \Delta t) - \rho_{u_i u_j}(\tau - \Delta t). \tag{3.27}$$

This is derived from basic definitions, and by Fourier transformation we find a relation for the cross-spectrum of the velocity increments

$$S_{\Delta u_i \Delta u_j}(f) = 2\left[1 - \cos\, 2\pi f \Delta t\right] S_{u_i u_j}(f) \tag{3.28}$$

We further observe that

$$\begin{aligned} \lim_{\Delta t \to 0} \frac{\rho_{\Delta u_i \Delta u_j}(\tau)}{\Delta t^2} &= -\frac{\partial^2}{\partial t^2}\rho_{u_i u_j}(\tau) \quad \text{and} \\ \lim_{\Delta t \to 0} \frac{S_{\Delta u_i \Delta u_j}(f)}{\Delta t^2} &= 4\pi^2 f^2 S_{u_i u_j}(f), \end{aligned} \tag{3.29}$$

which are well-known identities for the cross correlation $\rho_{\dot{u}_i \dot{u}_j}(\tau)$ and spectrum $S_{\dot{u}_i \dot{u}_j}(f)$ of time derivatives. The variance of velocity increments is $\sigma^2_{\Delta u_i} = 2\left[\sigma^2_{u_i} - \rho_{u_i}(\Delta t)\right]$,

which is useful for normalization. As an example, a Winterstein transformation of velocity increments

$$\Delta u_i = \sigma_{\Delta u_i} \left[a_i x_i + b_i (x_i^2 - 1) + c_i (x_i^3 - 3x_i) \right] \tag{3.30}$$

could be tuned for a match with prescribed values of skewness $S_{\Delta u_i}$ and kurtosis $K_{\Delta u_i}$ by numerical solution of the system in equation 3.21. Integration results in a stochastic variable, which probability distribution gradually converges to a Gaussian one in a way, which depends on the correlation function (Ditlevsen et al. 1996). This imply that for a given process, the choice of the skewness and kurtosis of the velocity-increments $(S_{\Delta u_i}, K_{\Delta u_i})$ should depend on the simulation time step Δt.

Example 3.1: Multi-variate simulation of with inhomogeneous distribution

Figure 11 shows a 10-min simulation of four correlated time series of wind speeds at positions vertically aligned with 10m separation. The mean wind profile is logarithmic defined by a relatively large roughness length, $z_0 = 1$m. The power spectra are of the Kaimal type $S(f,t) \propto [1 + 1.5fL(z)/u(t)]^{-5/3}$ normalized by a height-dependent standard deviation $\sigma_u(t) = A(z)u_*(t)$, and the length scales of the spectra are set to $L(z) = 45, 90, 135, 180$m, increasing with height. The spectral coherence is modelled by $\mathrm{coh}(\Delta z, f) = \exp(-10\Delta z, f/u)$. The probability distribution is Gaussian at the lowest level and increasingly non-Gaussian above. The non-Gaussian probability distributions are specified, by Winterstein transformations using the target skewness $S_u = 0, -\frac{1}{2}, -1, -\frac{3}{2}$ listed from below, and the lowest Kurtosis possible with Winterstein transformation. The skewness of each series in the simulation is shown in the Figure, and these measures are seen to differ from their target values because of the finite simulation length.

Example 3.2: Multi-variate simulation with non-Gaussian time increments

The target processes of the simulation, shown in Figure 12, have the same specifications as those in Figure 11, except that now the velocity increments are made non-Gaussian. The target skewness are $S_{\Delta u} = 0, \frac{1}{2}, 1, \frac{3}{2}$, listed from below, for the specified time step $\Delta t \approx 0.15$s. Close inspection of the figure will reveal that series in the upper frames rise faster than they fall.

Example 3.3: Simulation by sample data

In this example we apply data from the Oak Creek wind farm site, see Appendix B. The selected signals were made by four cup anemometers distributed on a single mast (the M1 mast) at the 65-m turbine hub height, ±15m from this level, and at 10m. With the given wind direction during the selected one-hour period, the mast was upstream the wind turbines. To estimate target statistics the 8-Hz time series were divided into blocks of 4096 records corresponding to $\approx 8\frac{1}{2}$min, and the first six blocks were processed in the following way.

- Fourier transforms, auto-, and cross spectra were calculated for each block and block averaged for smoother variation and reasonably unbiased coherence.
- Marginal probability distributions were found by Quicksort and used to establish the translation functions $g_i(x_i)$.
- Cross-covariance functions $\xi_{ij}(t)$ were found from average spectra, and translated to Gaussian cross-covariances $\rho_{ij}(t)$ by the correlation-distortion method

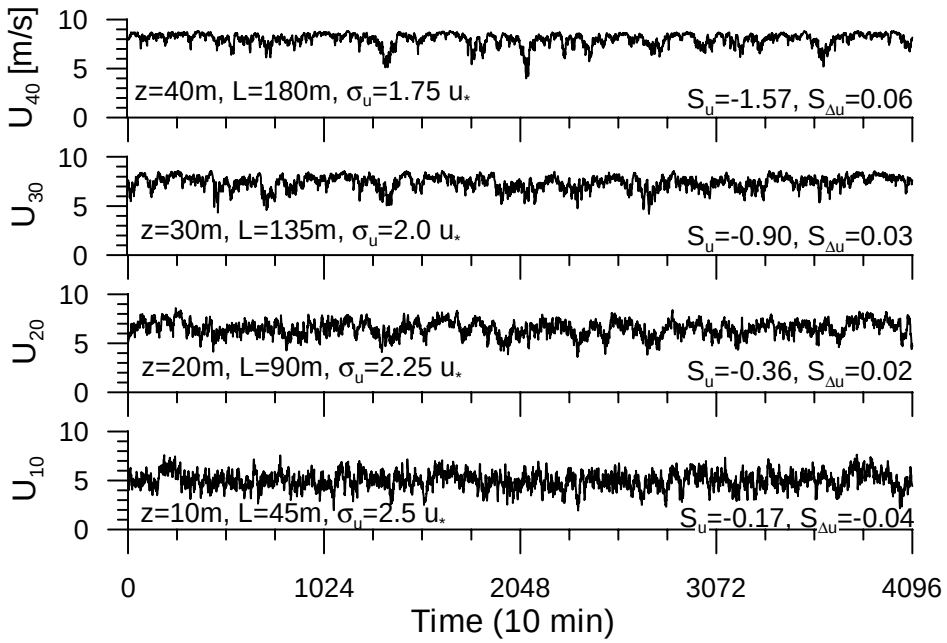

Figure 11. Simulation of four non-Gaussian wind-speed time series at heights z with specified turbulence length scale L, standard deviation σ_u and skewness S_u.

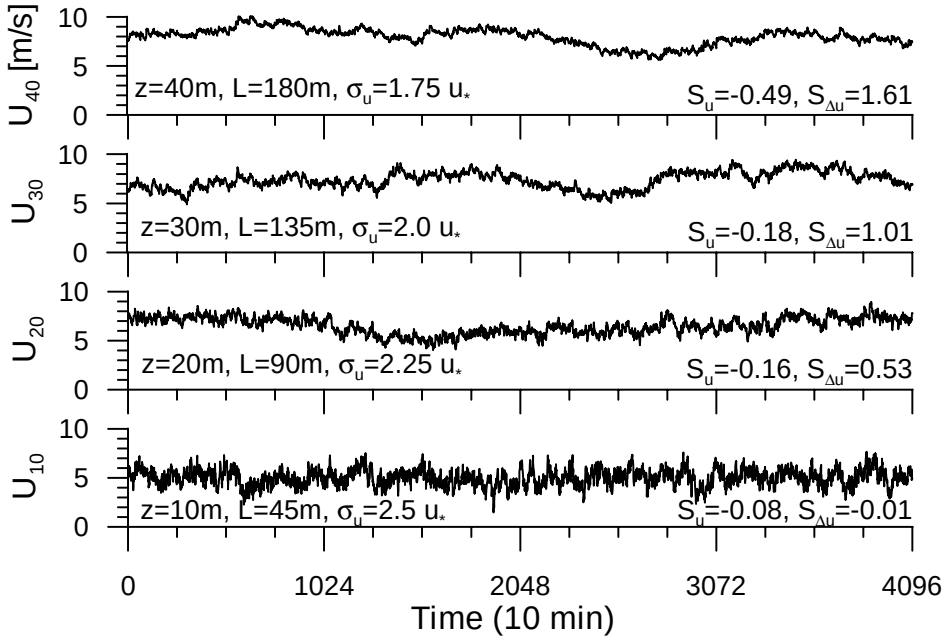

Figure 12. Simulation of four non-Gaussian wind-speed time series at heights z with specified turbulence length scale L, standard deviation σ_u, and skewness of time increment $S_{\Delta u}$.

using the Hermite expansion for computational efficiency. Covariance functions were Fourier transformed to spectra $\chi_{ij}(f)$ and smoothed with 20% bandwidth.

- The cross-spectral matrix was decomposed at up to 20 frequencies per decades by the Karhunen-Loève method with correction of negative definite matrices. Decomposed matrices at the remaining frequencies were approximated by

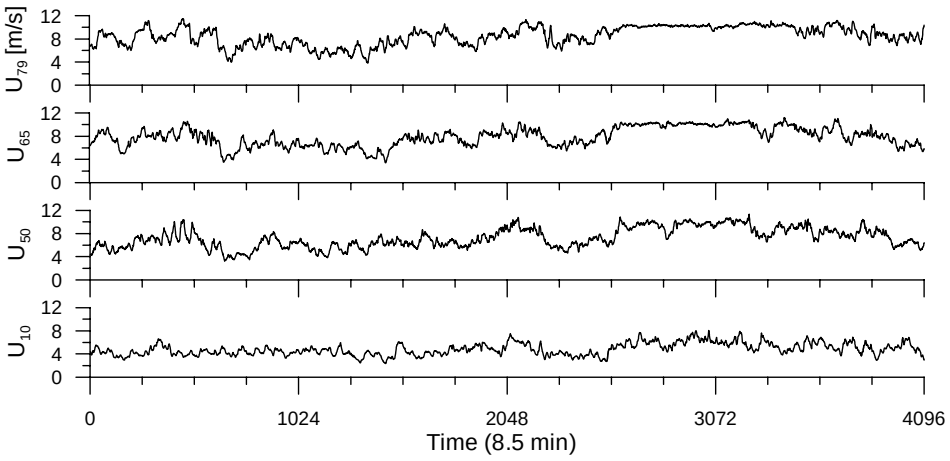

Figure 13. Cup-anemometer data from Mast 1, Oak Creek, Tahachipie, California, September 4, starting 5:51 AM.

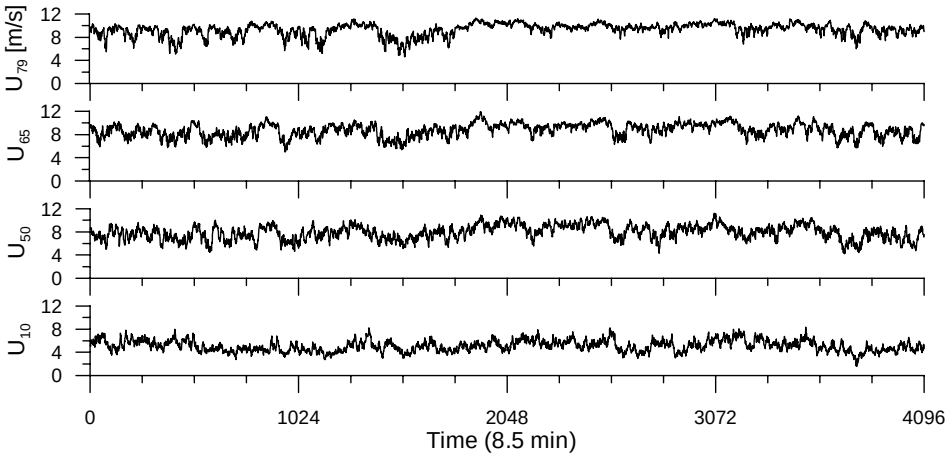

Figure 14. Simulation of processes in Figure 13, based on empirical distributions and correlations in the preceding period 5:00-5:51 AM.

cubic-spline interpolation.

The use of spectral smoothing, the relatively large number of decomposed matrices, and the correction of negative definite matrices are somewhat desperate remedies for ragged spectra resulting from a short experimental record. Dividing a record of fixed duration into a number of realizations is a compromise between the wish for reasonably long simulated series and the need to estimate cross-spectral distributions accurately, since spectral coherence will have a significant bias if the number of realizations is too small (Kristensen & Kirkegaard 1986). Of course, these problems would be less severe with smooth theoretical models instead of sample data.

Figure 14 shows a non-Gaussian simulation based on the empirical probability model and Figure 13 shows the 4096 records immediately after the reference period. In both simulation and observation, the three upper signals are well correlated, with longer time scales, less variance, and a less Gaussian probability distributions than for the 10-m signal. The target spectra of the simulated series are limited by the sample window, and this is probably why thee seem more stationary than the observed series. We shall follow up on this in example 4, section 3.5.

3.4 Non-stationary simulation

A non-stationary simulation should match time-dependent means and covariances in an ensemble-average sense, i.e.

$$\begin{aligned} \mu_i(t) &= \langle x_i(t) \rangle \\ \xi_{ij}(t,\tau) &= \langle \Big[x_i(t-\frac{\tau}{2}) - \mu_i(t-\frac{\tau}{2}) \Big] \Big[x_j(t+\frac{\tau}{2}) - \mu_j(t+\frac{\tau}{2}) \Big] \rangle. \end{aligned} \tag{3.31}$$

Accurate evaluation of empirical statistics is considerably more difficult than for stationary processes, since we cannot rely on the ergodic hypothesis and use simple time averaging. Although this could be a practical problem, we will not consider it any further, but simply extend the multivariate Fourier-simulation method to

$$x_i(t) = \sum_{k=0}^{M} X_{ik}(t) e^{\mathrm{i} \cdot k \Delta f t} \tag{3.32}$$

The Fourier modes are now time dependent, and we express them by Cholesky decomposition

$$X_{ik}(t) = \begin{cases} \mu_i(t) & \text{for} \quad k = 0 \\ \sum_{j=1}^{i} l_{ijk}(t) \sqrt{\Delta f} y_{jk} & \text{for} \quad k = 1 \ldots M/2 \\ X_{ik}(t) = X^*_{i,M+1-k}(t) & \text{for} \quad k = M/2+1 \ldots M, \end{cases} \tag{3.33}$$

or equivalent expressions for Karhunen-Loève expansion, see Section 3.2. In general, the time-dependent coefficients in equation 3.32 prevents direct use of the efficient FFT algorithm, except in the special case of uniform modulation of all spectral components.

$$\chi_{ij}(f,t) = A(t) \cdot \check{\chi}_{ij}(f) \Rightarrow l_{ij}(f,t) = \sqrt{A(t)} \cdot \check{l}_{ij}(f). \tag{3.34}$$

This formulation has been used to simulate seismic ground motions, e.g. by Li & Kareem (1991) and Deodatis (1996). The latter author further suggests to simulate the general case by direct computation of equation 3.32 instead of FFT.

Grigoriu (1995) discusses various parametric models for stochastic processes, including the use of Bezier-spline functions for time variation. A third-order Bezier spline is defined by

$$f(t) \approx \sum_{p=0}^{3} \binom{3}{p} \delta^p (1-\delta)^{3-p} \cdot f_{r+p/3} \tag{3.35}$$

where

$$\delta = \frac{t - t_r}{t_{r+1} - t_r} \quad \text{for} \quad t_r \le t \le t_{r+1} \tag{3.36}$$

is a dimensionless time, $f_r = f(t_r)$, $f_{r+1} = f(t_{r+1})$ are reference points, and $f_{r+1/3}$, $f_{r+2/3}$ are Bezier control points, defined by time derivatives at the reference points $\dot{f}(t_r)$ and $\dot{f}(t_{r+1})$, see appendix D. If time derivatives are unknown, they may be evaluated by cubic-spline interpolation (Press et al. 1992). Thus, we construct a smooth variation from a linear combination of reference points $f(t_r)$ and auxiliary Bezier control points.

$$X_{ik}(t) \approx \begin{cases} \sum_{p=0}^{3} \binom{3}{p} \delta^p (1-\delta)^{3-p} \mu_{i,r+p/3} & \text{for} \quad k = 0 \\ \sum_{j=1}^{i} \Big[\sum_{p=0}^{3} \binom{3}{p} \delta^p (1-\delta)^{3-p} \cdot l_{ijk,r+p/3} \Big] \sqrt{\Delta f} y_{jk} & \text{for} \quad k = 1 \ldots M/2 \\ X_{ik}(t) = X^*_{i,M+1-k}(t) & \text{for} \quad k = M/2+1 \ldots M. \end{cases} \tag{3.37}$$

In fact we see that we can simulate a non-stationary process by linear combination of standard FFT-based stationary simulations

$$x_i(t) = \sum_{p=0}^{3} \binom{3}{p} \delta^p (1-\delta)^{3-p} \bar{x}_{i,r+p/3}(t) \tag{3.38}$$

where the series $\bar{x}_{i,r+p/3}(t)$ are simulated with input values $\mu_{i,r+p/3}$ and $l_{ijk,r+p/3}$ at reference points and Bezier control points *with the same random input* y_{jk}*!* This is more efficient than direct computation with time-dependent Fourier modes.

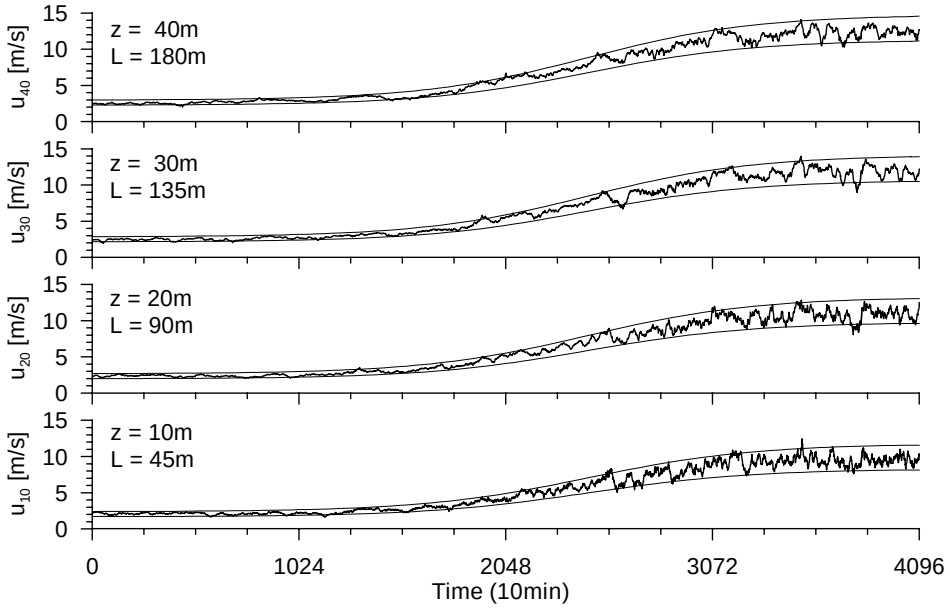

Figure 15. Simulation of four non-stationary wind-speed time series at heights z and turbulence length scales L.

Example 3.4: Multi-variate non-stationary simulation

Figure 15 shows a 10-min simulation of four correlated time series of wind speeds at positions vertically aligned with 10m separation. The mean wind speed, i.e. the ensemble mean of many realizations, is specified as a smooth variation in time using a $\tanh(x)$ function. At any time the ensemble mean wind profile is logarithmic with a roughness length set to $z_0 = 0.1$m. The power spectra are of the Kaimal type $S(f,t) \propto [1 + 1.5fL(z)/u(t)]^{-5/3}$, normalized by a time-dependent standard deviation $\sigma_u(t) = 2.5u_*(t)$, and the length scales of the spectra are set to $L(z) = 45, 90, 135, 180$m, increasing with height. The spectral coherence is modelled by $\mathrm{coh}(\Delta z, f) = \exp(-10\Delta z, f/u)$. For computational efficiency the cross-spectral matrix is only decomposed at four reference states, and matrices for intermediate frequencies are found by third-order Bezier interpolation. The smooth thin lines in the Figure indicate the $\mu(t) \pm 2\sigma_u(t)$ levels, i.e. 4.6% of the values should be outside this range.

Actually, this scenario with constant length scales and constant turbulence intensity could be simulated by traditional simulation in spatial domain, sampled with increasing longitudinal separation, reflecting varying advection $u(t)$, and scaled for varying amplitude of the velocity fluctuations. The present method is, however, more versatile, e.g. it would be possible to simulate more complex variations of the spectra.

Example 3.5: Simulation of wake turbulence

As discussed in Appendix E, the velocity perturbations in a wind-turbine wake are the combined result of atmospheric background turbulence, tip-vortices, mixing with faster-moving ambient air, and the sweeping movements of the wake, which imply that an observer intermittently is exposed to either wake or free flow. Thus, the local velocity is not a stationary process.

The Langevin process offers a simple stochastic model for centreline movements.

$$\frac{dy_c\,(t)}{dt} = -\frac{y_c\,(t)}{T} + a\,(t) \tag{3.39}$$

Here, T is a suitable time scale and the random accelerations $a\,(t)$ are modelled by a Gaussian process with a variance $\langle a\,(t')\,a\,(t)\rangle = \delta\,(t'-t)\cdot 2\sigma_y^2/T^2$, which is scaled for a match with the variance of the centreline position σ_y.

The moving-frame cross-wind profile of the velocity deficit in a wind-turbine wake evolves from a ring shape in the near region to a bell shape in the far region. This could be modelled by

$$\frac{\Delta u_{\mathrm{mov}}(r)}{U_0} = \left[1 - \sqrt{1 - C_T\frac{d^2}{8s^2}\exp\left(-\frac{a^2}{2s^2}\right)\mathrm{I}_0\left(\frac{a^2}{2s^2}\right)}\right] \cdot \frac{\exp\left(-\frac{r^2}{2s^2}\right)\mathrm{I}_0\left(\frac{ar}{s^2}\right)}{\mathrm{I}_0\left(\frac{a^2}{2s^2}\right)} \tag{3.40}$$

where C_T is the thrust coefficient, d is the rotor diameter, r is the distance from centreline, and (a, s) are the radius and spreading of a ring of Gaussian kernels, see Appendix E. Figure 16 shows three versions of this profile. Also shown on this Figure is a profile of the standard deviation of velocity perturbations caused by all other effects than wake meandering. We assume that this is higher in the wake than in the ambient flow, and for simplicity (and lack of knowledge) we use the loose estimate $\sigma_u(r)/\sigma_u, 0 = 1 + \exp\left(-(2r/d)^2\right)$. As in the previous example, the spectral distribution is modelled by a Kaimal's formula, with a local length scale which is shorter in the wake region than in the ambient, say $L_0\left[1 - 0.5\exp\left(-(2r/d)^2\right)\right]$. Variations of spectral coherence are neglected.

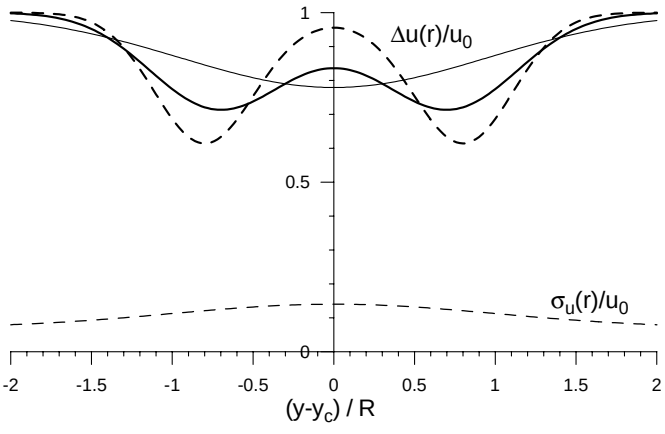

Figure 16. Three moving-frame wake profiles with fixed thrust $C_T = 0.7$ and radial spreading $a^2 + s^2 = (d/2)^2$, but variable width of the Gaussian ring $s/(d/2) = 0.3, 0.4, 0.9$.

The centreline positions, shown in the top frame of Figure 17, are simulated by a Langevin process with time scale and standard deviation set to $T = 2$min

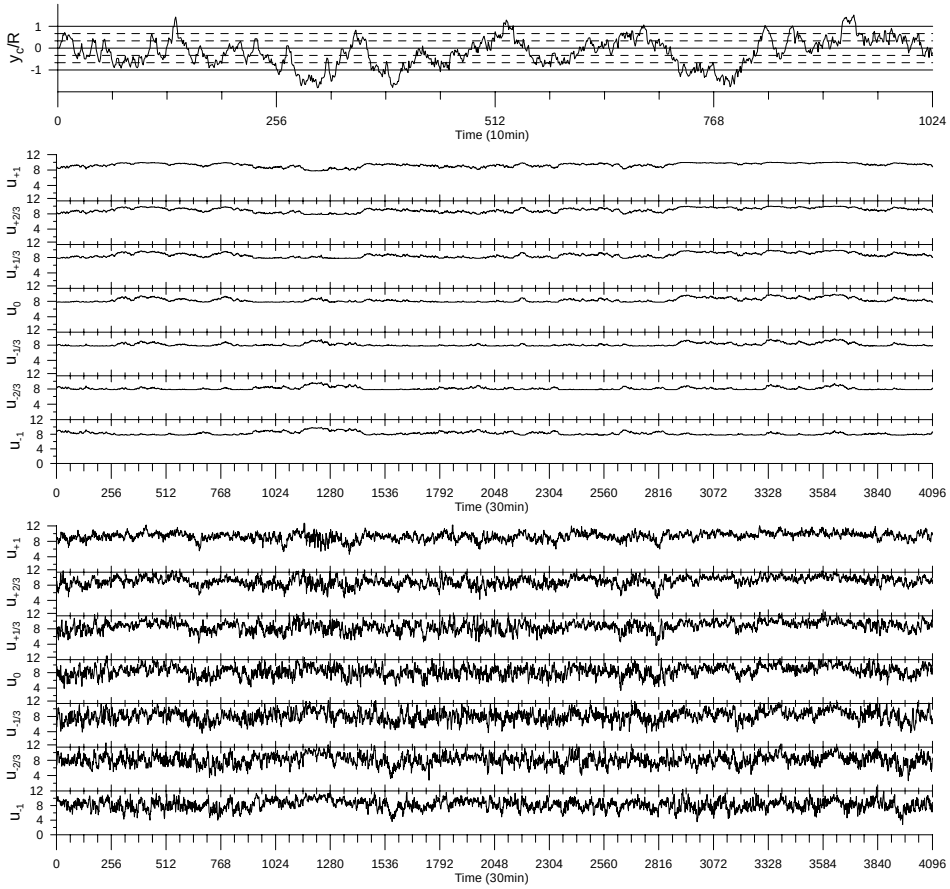

Figure 17. Simulation of wake centreline (top frame), fluctuations due to the sweeping wake at positions $-1, -2/3 \ldots 1$ *times the rotor radius (mid frame), and non-stationary turbulence (lower frame). The moving-frame wake velocity is modelled by unimodal profile from figure 16.*

and $\sigma_y = 20$m corresponding to an angle of $\sigma_\theta \approx 10^o$ for a rotor diameter of $\sigma_y = 54$m and a downwind position of $\sigma_y = 200$m. Meander induced velocity fluctuations, caused by the random centre-line movements and the uni-modal profile from Figure 16, are shown for seven positions distributed evenly over the rotor plane at hub height. It is seen how local velocities are reduced when the centre line approaches an observation point, and that velocities at the two edges of the rotor are anti-correlated. Finally, the Figure shows a non-stationary simulation of turbulent velocities, using centre-line position as a controlling parameter for local mean and standard deviation. In this example, where turbines are aligned in the wind direction, the intermittency is most distinct at the edges of the rotor plane.

Figure 18 shows a similar scenario using the same time series of centre-line positions but a more detailed moving-frame profile for the velocity deficit. The meander-induced velocity perturbations are more frequent, sudden, and larger in amplitude than those in Figure 17, and the correlation or anti-correlation among series are less obvious.

3.5 Conditional simulation

This section consider simulation of a multivariate probability model when a subset of the processes is known. We shall refer to this as conditional simulation, not to be confused by constrained simulation defined in the next section.

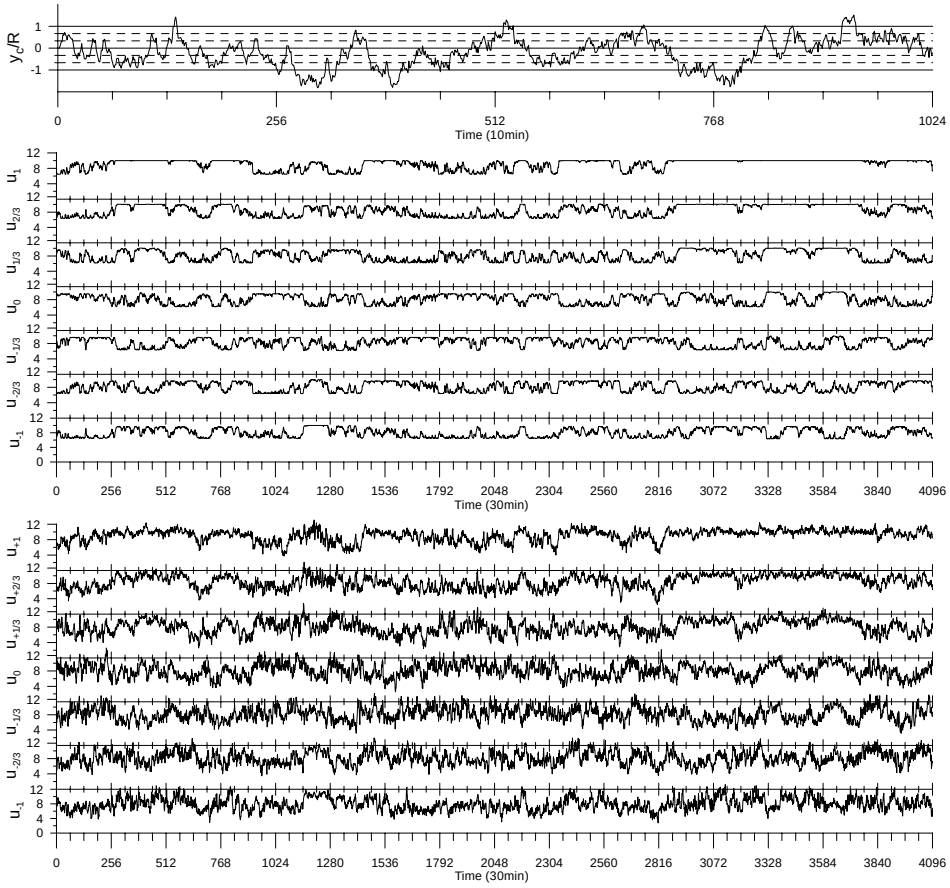

Figure 18. As figure 17 except that the moving-frame wake velocity is modelled by the most bimodal profile from figure 16.

Suppose that we have established the probability model for a set of signals and continues to measure a subset of these. Conditional simulation of the missing signals is then enabled by Cholesky decomposition, where we organize the system with the known variables before the unknown.

$$\begin{bmatrix} \mathbf{x_1} \\ \mathbf{x_2} \end{bmatrix} = \begin{bmatrix} \mu_\mathbf{1} \\ \mu_\mathbf{2} \end{bmatrix} + \begin{bmatrix} \mathbf{L_{11}} & \mathbf{0} \\ \mathbf{L_{21}} & \mathbf{L_{22}} \end{bmatrix} \begin{bmatrix} \mathbf{y_1} \\ \mathbf{y_2} \end{bmatrix}. \tag{3.41}$$

Here, $\mathbf{x_1}$ and $\mathbf{x_2}$ are vectors composed of known and unknown values, respectively, with corresponding mean values $\mu_\mathbf{1}$ and $\mu_\mathbf{2}$. With N_1 known and N_2 unknown processes, the dimensions of the Cholesky sub-matrices becomes: $\mathbf{L_{11}}$ $[N_1 \times N_1]$, $\mathbf{L_{21}}$ $[N_2 \times N_1]$, and $\mathbf{L_{22}}$ $[N_2 \times N_2]$. By elimination of the vector $\mathbf{y_1}$, we obtain the relation for conditional simulation

$$\mathbf{x_2} = \mu_\mathbf{2} + \mathbf{L_{21}}\mathbf{L_{11}^{-1}}\left(\mathbf{x_1} - \mu_\mathbf{1}\right) + \mathbf{L_{22}}\mathbf{y_2}, \tag{3.42}$$

where the inverse matrix $\mathbf{L_{11}^{-1}}$ is relatively fast to compute from the triangular matrix $\mathbf{L_{11}}$. The sum of the first two terms on the right-hand side of equation 3.42 is the conditional mean vector, and $\mathbf{L_{22}}\mathbf{L_{22}^*}$ is the conditional covariance matrix. It is easy to extend this to Fourier simulation.

Non-Gaussian conditional simulation

To initiate the simulation by Gaussian input in spectral domain, we could transform the observed time series by the reverse of equation 3.10

$$x_i\left(t\right) = g_i^{-1}\left[u_i\left(t\right)\right] = \phi^{-1}\left[F_{i,T}\left[u_i\left(t\right)\right]\right] \tag{3.43}$$

and Fourier transform. This operation will work in the context of turbulence data, which usually are close to Gaussian.

Although it should not be a problem in the context of wind loads, we note that equation 3.43 will fail for a process with finite probability of certain values, e.g. the base-line values in the process shown in Figure 7. The problem is that observations of such values would corresponds to a range of auxiliary Gaussian values, which prevents a simple translation in time domain. Instead, an alternative correction for correlation distortion must be made in frequency domain, see Figure 19. Firstly, we normalize the observed time series $u_{i,obs}(f)$, Fourier transform into frequency domain, and calculate empirical power spectra $\chi^u_{i,obs}(f)$. By inverse Fourier transformation we then calculate empirical auto-correlation functions $\xi^u_{i,obs}(\tau)$ and translate these into auto-correlation functions for Gaussian processes $\rho_{i,obs}(\tau)$ by equation 3.16 or 3.24. The Gaussian auto-correlations are Fourier transformed into Gaussian power spectra $\chi^x_{i,obs}(f)$, and finally, the last step in the alternative route in figure 19, we estimate normalized Gaussian variables representing observations in frequency domain.

$$X_{i,obs}(f) \simeq U_{i,obs}(f)\sqrt{\chi^x_{i,obs}(f)/\chi^c_{i,obs}(f)}. \tag{3.44}$$

This formula rely on the assumption that phase angles of the Fourier modes are unsensitive to the translation, which is reasonable, since peaks in observed and translated Gaussian time series are intimately related, see Seong & Peterka (2001) and Figure 7.

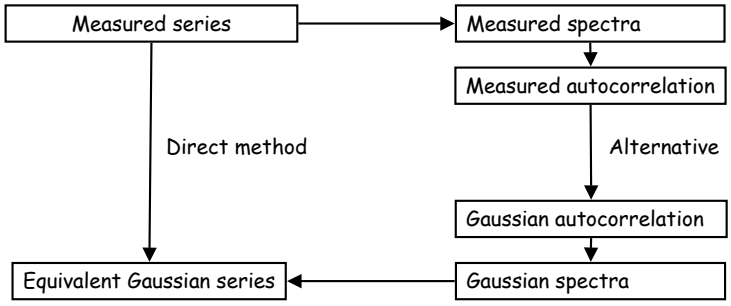

Figure 19. Two approaches for conditional simulation of non-Gaussian series.

Example 3.6: Conditional simulation by sample data

In continuation of Example 2 (Section 3.3), we make a conditional simulation considering the top signal from figure 13 as *known* and the remaining signals as *unknown*. Spectra and marginal probability density functions are estimated by data from the preceding period as detailed in Example 2.

The fat curves in the three lowest frames of Figure 20 show a random realization, and the thin curves indicates the 5% and 95% percentiles of 2000 realizations. The range of realizations is wider, and the percentiles are less detailed at the 10-m level, because this signal is less correlated with the input.

The Gaussian input representing the known process was generated by the direct method, i.e. inverse translation as in equation 3.43 followed by Fourier transformation. Keeping the seed for the random number generator is constant, the approximate alternative method, sketched in the right-hand side of Figure 19, gave similar result, i.e. when comparing the two simulation types Pearsons' correlation coefficient was found relatively high, i.e. $r > 0.995$.

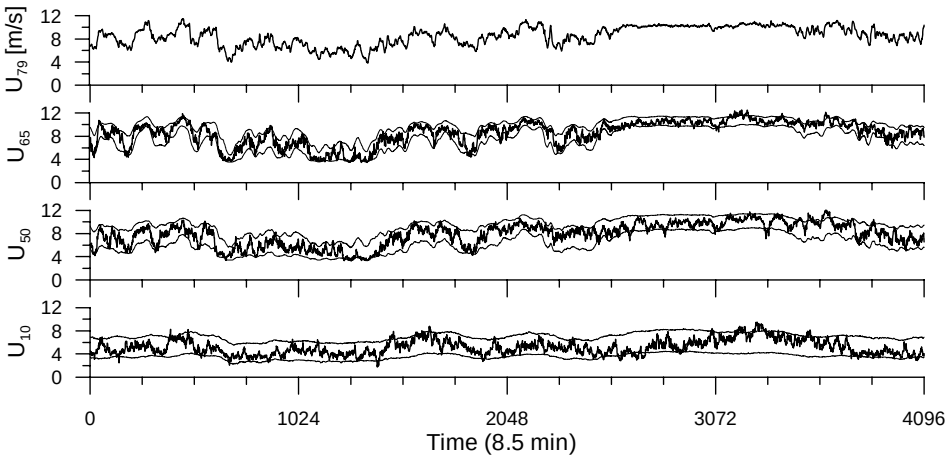

Figure 20. Conditional simulation of processes in figure 13, based on the top signal and empirical distributions and correlations in the preceding period 5:00-5:51 AM.

4 Event counting

In principle a turbulence simulator can generate any time series. This is Murphy's law: any possible event will happen sooner or later. In this chapter we investigate how soon or late. In sections 4.2 and 4.3 we set up theory for event rates and recurrence times for gaussian processes. The results are then discussed in relation to atmospheric data in an attempt to quantify the effect on non-gaussianity. But first we discuss the relation between data and simulations.

4.1 The connection to simulated data

Measured data are usually organized into ten minutes intervals. In some cases time series are available, but more often only ten minute statistics has been stored. The wind climate at a given site is characterized by the probability distribution function (pdf) of ten minute averages of the wind speed. The ten minute average wind speed therefore plays a historical role that cannot be changed easily.

Seen in this perspective, the role of simulations is to generate an estimate of the fluctuations $u'(t) = u(t) - \bar{u}$ for a given value of $\bar{u}$. It is customary to regard $u'(t)$ as a statistically stationary process, and we shall do this, but it should be emphasized that the assumption is tricky. Even when $u(t)$ is a stationary process, $u'(t)$ is in fact not. This is illustrated in figure 21 which shows measurements of the quantity

$$I(t) = \sqrt{\langle (u'(t)/\bar{u})^2 \rangle} \tag{4.1}$$

where time t is measured relative to the start of each interval. We use a bar to indicate a ten minute average and brackets $\langle \quad \rangle$ to indicate the ensemble mean value taken over a large number of ten minute intervals (in this case 2606 series with $\bar{u}$ between 8m/s and 9m/s). $I(t)$ superficially resembles a sort of time dependent turbulence intensity. From the figure it is evident that $I(t)$ is slightly larger near the beginning and the end of the ten minute period. This should not lead us to believe that the turbulence gets more intense every ten minutes! The explanation is that $\bar{u}$ makes a jump every ten minutes and these jumps are compensated by opposite jumps in u' so that u does not jump. The problem would disappear if we used the ensemble mean value $\langle u \rangle$ instead of $\bar{u}$, but only in exchange for the even worse problem of finding out what $\langle u \rangle$ is. We could find $\langle u \rangle$ for a given ten

minute series if it was a piece of a theoretical, very long stationary time series, but that is not how things are. For each ten minutes there is a relevant set of meteorological conditions and we can only pool data with the same parameters. Ideally, one of these parameters is $\langle u \rangle$, but we only have the estimate $\bar{u}$, so there is no way to find out what $\langle u \rangle$ really is. The actual continuation of a given measured ten minute time series would not do because meteorological conditions change. It is an abstract quantity that cannot actually be measured. Nonetheless, it seems plausible that $\bar{u}$ is actually a good estimate of $\langle u \rangle$. Just how good the estimate is hard to say because we cannot distinguish the random fluctuations of $\bar{u}$, which would be there even if $\langle u \rangle$ was constant, from the gradual variations of $\langle u \rangle$ over time. At least not without additional theory. However, figure 21 seems to indicate that $\bar{u}$ for ten minute intervals is not a bad estimate of $\langle u \rangle$.

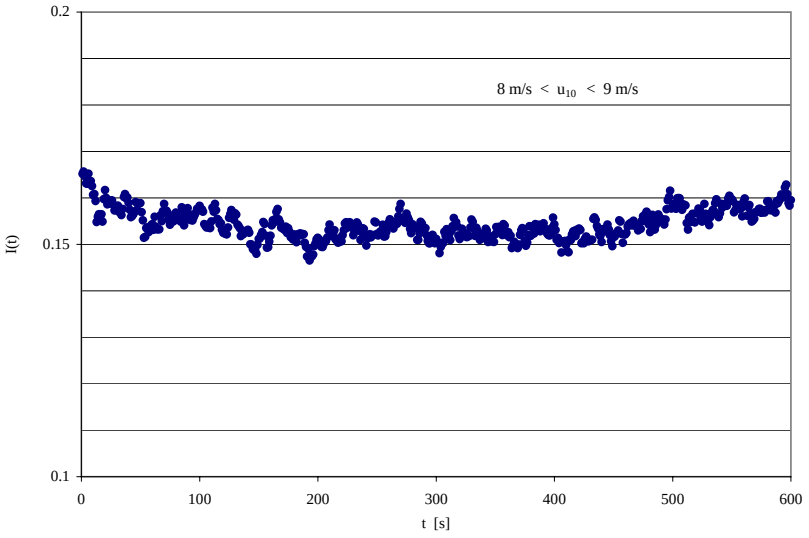

Figure 21. $I(t)$ (defined in the text) based on 2606 ten minute time series from the Lammefjord experiment with $\bar{u}$ ranging between 8 and 9 m/s.

In terms of simulations we should avoid teaching the simulator to make jumps every ten minutes. For simplicity we consider a simulator that yields samples of a stationary, periodic, gaussian process $v(t)$ with zero average ($\bar{v} = 0$ in each realization). Its properties are completely defined by the correlation function $R(t) = \langle v(t')v(t+t') \rangle$. Alternatively we specify the spectrum $S(\omega)$ which is just the Fourier transform of R. The spectrum is usually obtained from a time series by applying a discrete Fourier transform to it and take the absolute square of the result. This is faster than calculating the correlation function directly. Note that $\bar{v} = 0$ implies $S(0) = 0$, since $\bar{v}$ is the Fourier component for $\omega = 0$. A spectrum is calculated for each time series and the ensemble mean spectrum is finally made. The resulting spectrum is equal to the Fourier transform of the correlation function of u extended to a periodic function. The measured spectrum therefore corresponds to the correlation function

$$R_S(t) = \frac{T-|t|}{T} R(t) + \frac{|t|}{T} R(T-|t|) - \frac{2}{T^2} \int_0^T (T-t')R(t')dt' \tag{4.2}$$

where T is the period (ten minutes). If we make a simulator based on R_S then we actually teach it to mimic the periodic version of $u(t)$ including a spurious jump every ten minutes, on average. These jumps may of course take place anywhere, not just at the endpoints. This shows up as a discontinuity of the first derivative

$R'_S(t)$ at $t = 0$. For a differentiable process (such as the measured u) we have

$$R'(0) = \langle \frac{d}{dt} \frac{1}{2} v(t)^2 \rangle = 0 \tag{4.3}$$

but differentiating (4.2) we find

$$R'_S(t) \to \pm \frac{R(T) - R(0)}{T} \text{ for } t \to \pm 0 \tag{4.4}$$

The discontinuity shows that $v(t)$ becomes non-differentiable. In reality it is not because only a finite number of Fourier modes are used, but it will still contain unphysical swings. In order to avoid this we should derive the spectrum otherwise. Each time series is extended to double length $2T$ by filling in zeros for $T < t < 2T$. The average is not subtracted from $u(t)$. Then the convolution is found by Fourier transform, squaring and inverse transform (the zero mode is not nulled), and an ensemble mean is calculated. This procedure yields $\frac{T-|t|}{T} \langle u(t')u(t'+t) \rangle$ from which $\langle u(t')u(t'+t) \rangle$ can be found. Finally $R(t)$ is found by subtracting a constant so that $\int_0^T R(t)dt = 0$, and the spectrum can be made by Fourier transforming $R(t)$.

Although this procedure is undoubtedly more correct, it makes little difference in practice. The reason is that turbulence time series are already quite jumpy due to the $\omega^{-5/3}$ dependence in the inertial range. If the spectrum continues like this for $\omega \to \infty$ then $R(t) - R(0)$ will be proportional to $|t|^{2/3}$ for small t, so that $R'(t) \to \mp\infty$ for $t \to \pm 0$. This does not happen for real data due to the effect of viscosity and instrumental averaging which bends $R(t)$ to horizontal for very small t (a fraction of a second).

The main point we wish to make here is to emphasize the central role of the behaviour of $R(t)$ near $t = 0$, and that care should be taken when $R(t)$ is deduced from data.

4.2 Event counting

In this connection we present a theory for events. In this context an 'event' is defined by means of the function

$$F(t) = \int \phi(t - t')v(t')\, dt' \tag{4.5}$$

An event at time t is simply that $F(t)$ crosses a critical value F_c on its way up. The condition for such an up-crossing is that $F(t) = F_c$ and $\dot{F}(t) > 0$. Up-crossing rates were analysed by Rice (1944). The basic observation is to note the following identity for δ-functions.

$$\delta(f(t))\, |f'(t)| = \sum_{f(t_i)=0} \delta(t - t_i) \tag{4.6}$$

where the sum is taken over all zero points of f. If we insert $f(t) = F(t) - F_c$ then the right hand side is the density of crossings. The density of up-crossings is given by

$$n_F(t; F_c) \;=\; \theta(\dot{F}(t)) \sum_{F(t_i)=F_c} \delta(t - t_i) \;=\; \delta(F(t) - F_c)\, \dot{F}(t)\, \theta(\dot{F}(t)) \tag{4.7}$$

where $\theta(x)$ is the unit step function ($\theta(x) = 0$ for $x < 0$ and $\theta(x) = 1$ for $x > 0$). Taking the mean value on both sides we find the mean rate of up-crossings per unit time

$$N_F(F_c) = \int_0^\infty \dot{F}(t)\, P(\dot{F}, F_c)\, d\dot{F} \tag{4.8}$$

where $P(\dot{F}, F)$ is the joint pdf of $F(t)$ and $\dot{F}(t)$, Rice (1944). In our case F and $\dot{F}$ are gaussian with

$$\begin{aligned}
\langle F^2 \rangle &= \int dt' \int dt'' \phi(t') R(t' - t'') \phi(t'') = R_F(0) \\
\langle \dot{F}^2 \rangle &= -\int dt' \int dt'' \phi(t') R''(t' - t'') \phi(t'') = -\ddot{R}_F(0) \\
\langle F\dot{F} \rangle &= 0
\end{aligned} \tag{4.9}$$

where

$$R_F(t) = \langle F(t+t')F(t') \rangle = \int dt' \int dt'' \phi(t') R(t - t' + t'') \phi(t'') \tag{4.10}$$

is the correlation function for F. $F(t)$ and $\dot{F}(t)$ are uncorrelated because $\frac{1}{t}\int_0^t F\dot{F}dt \to 0$ for $t \to 0$, and uncorrelated gaussian variables are always independent. This simplifies the integration because $P(F, \dot{F}) = P(F)\,P(\dot{F})$ and $P(F)$ can be taken outside the integration and (4.8) becomes

$$N_F(F_c) = \frac{\sqrt{\langle \dot{F}^2 \rangle}\, \exp\left(-\frac{F_c^2}{2\langle F^2 \rangle}\right)}{2\pi\sqrt{\langle F^2 \rangle}} = P(F_c)\sqrt{\frac{\langle \dot{F}^2 \rangle}{2\pi}} \tag{4.11}$$

A transformed process $U(t) = g(F(t))$ defined point-wise by the increasing function g will generally not be gaussian and U and $\dot{U}$ may not be independent. However, F crossing F_c is the same as U crossing $g(F_c)$, hence $N_U(g(F_c)) = N_F(F_c)$.

In the simplest case $\phi(t) = \delta(t)$, i.e. $F(t) = v(t)$, (4.11) reduces to

$$N_v(v_c) = \frac{\sqrt{-R''(0)}\, \exp\left(-\frac{v_c^2}{2R(0)}\right)}{2\pi\sqrt{R(0)}} \tag{4.12}$$

Choosing $\phi(t) = \delta(t - t_1) - \delta(t)$, i.e. $F(t) = v(t + t_1) - v(t)$, we get

$$N_{\Delta v}(\Delta v_c) = \frac{\sqrt{2(R''(t_1) - R''(0))}\, \exp\left(-\frac{\Delta v_c^2}{2(R(0) - R(t_1))}\right)}{2\pi\sqrt{2(R(0) - R(t_1))}} \tag{4.13}$$

In these examples the result depends on $-R''(0)$ which is equal to $\langle \dot{v}^2 \rangle$, or equal to $\int S(\omega)\omega^2 d\omega$ if we prefer to use the spectrum. For isotropic turbulence it can be expressed as $R''(0) = -\frac{\bar{u}^2\varepsilon}{15\nu}$, which shows that the quantity is extremely large due to the low value of the viscosity ν. In practise it is therefore not obtainable from usual micro-meteorological data. The problem is that turbulence contains tiny structures that contribute substantially to the result for the crossing rate. The small scale fluctuations may bother a flying insect, but would not affect a large structure such as a wind turbine. It can therefore only make sense to look for maxima if the very short lived peaks have been removed by a suitable low pass filter. At the same time we can note that a low pass filter affects the mean gust only by making $R(t)$ slightly less pointed near $t = 0$ and removing some of the small fluctuations. Since the filter removes a finite part of the variance, $R(t)$ would be well defined even if the spectrum has infinitely long $\omega^{-5/3}$ tails. The 'width' of an event, defined in some way as a measure of the time interval around an event in which the constrained process differs appreciably from the unconstrained process, would therefore be finite. Nonetheless, the event rate would diverge if the filter is removed, and that can only be possible if the 'width' around one event contains many other events. Conversely, if we take a period where the filtered process does not exhibit an event, we would not expect the little extra variance to make the un-filtered process to exhibit very many extra events. In other words, the events will tend to occur in cascades, or bursts, separated by relatively long periods with no events. The following example illustrates this.

Example 4.1: Cascading events in the Ornstein-Uhlenbeck process

To illustrate (4.11) and the concept of cascading events we turn to the Ornstein-Uhlenbeck process. This is the stationary Gaussian process with exponential autocorrelation. It is continuous, but not differentiable. A simulated example with unit variance and time scale, i.e. a correlation function

$$R(t) = \exp(-|t|) \quad , \tag{4.14}$$

is shown in figure 22. A time series five time units long has been simulated with a time resolution $\Delta t = 0.01$. There are four crossings of the level 2.2.

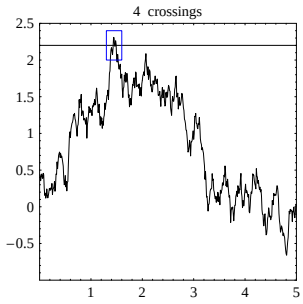

Figure 22. Realization of the Ornstein-Uhlenbeck process.

In figure 23 the small area indicated in figure 22 is enlarged. In the subsequent plots the time resolution is increased.

As seen from figure 24 the number of crossings increases without limits for $\Delta t \to 0$. The line in the figure is proportional to $(\Delta t)^{-1/2}$ indicating a fractal dimension of the set of crossings of 1/2. Indeed, (4.11) or in fact (4.12) predicts an infinite up-crossing rate, but it is also clear that the average waiting time for an event (crossing of level 2.2) to occur is finite.

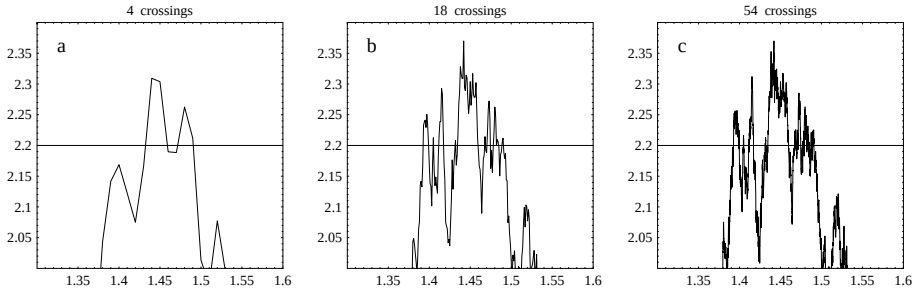

Figure 23. a: *A close up of figure 22.* b: *Same simulation but with 10 times the resolution.* c: *Resolution increased yet a factor of 10.*

4.3 Recurrence times

Closely related to the up-crossing rate is the recurrence time. The purpose of defining this concept is to take the effect of cascading into account. Various definitions of the recurrence time for an event exist, but we find the following definition most precise. Let $P_0(t)$ denote the probability that *no* event happens during the observation time t. For two very long consecutive time intervals of length t_1 and t_2 we may expect that events in the two periods are independent. For the combined

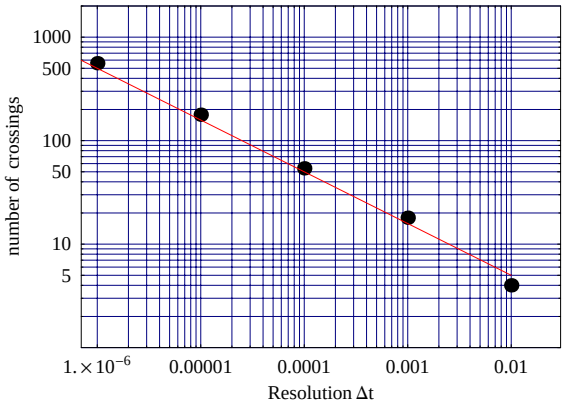

Figure 24. Number of crossings as a function of resolution.

observation period we therefore have $P_0(t_1 + t_2) = P_0(t_1)\,P_0(t_2)$. In other words, we expect an exponential form

$$P_0(t) \to \mathrm{e}^{-\lambda t} \text{ for } t \to \infty \tag{4.15}$$

where λ is independent of t. If P_0 has this property, we define the recurrence time as $1/\lambda$. Note that if the events are independent (i.e. described by a Poisson process) then the exponential form is exact (also for small t) and $1/\lambda$ is equal to the mean time between events. In this case $1/\lambda$ would also be equal to the waiting time, i.e. the mean time from a arbitrary start time to the next event. The waiting time is well defined also in the general case and in practice it is not very different from $1/\lambda$, but it is somewhat more complicated to treat theoretically than recurrence time (as we have chosen to define it). For the periodic processes produced by a simulator, the recurrence rate for F up-crossing F_c, $\lambda_F(F_c)$, should be related to the mean number of simulations needed to obtain an event. The number of events during $t = nT$ (where T is the period) should therefore be counted for n different realizations. Since events in different realizations are independent we find

$$P_0(T) = \mathrm{e}^{-\lambda_F(F_c)T} \tag{4.16}$$

Let $M_F(F_c)$ denote the mean number of up-crossings per realization given that at least one up-crossing takes place. Since the probability of having an up-crossing is $1 - P_0(T)$, we have

$$M_F(F_c)(1 - P_0(T)) = N_F(F_c)T \tag{4.17}$$

so that

$$\lambda_F(F_c) = -\frac{1}{T}\,\log\left[1 - \frac{N_F(F_c)T}{M_F(F_c)}\right] \tag{4.18}$$

If $N_F(F_c)T \ll M_F(F_c)$ we have $\lambda \approx N_F/M_F(F_c)$. The reason why the recurrence rate is smaller than the mean event rate is that events may come in cascades. It is easy to construct an example. Take a process where the up-crossings of a certain level are rare and effectively independent events so that $\lambda_F(F_c) = N_F(F_c)$ is a good approximation. Then alter the process by adding a small very high frequency component to the spectrum. This adds a small amount of jitter, so for each up-crossing of the original process there will now be a large number of crossings. The effect on $N_F(F_c)$ is therefore large while $\lambda_F(F_c)$ should stay about the same.

The average waiting time for an event (starting at a random point in the data) can be determined as

$$T_{wait} = \frac{\sum_i \Delta t_i{}^2}{2\sum_i \Delta t_i} \tag{4.19}$$

where $\{\Delta t_i\}$ is the set of all time intervals between events in the time series. The recurrence time $1/\lambda$ can be determined similarly as

$$1/\lambda = \frac{\sum_{\{i|\Delta t_i>\tau\}} (\Delta t_i - \tau)^2}{2\sum_{\{i|\Delta t_i>\tau\}} (\Delta t_i - \tau)} \tag{4.20}$$

where τ is chosen large enough to represent the limit $\tau \to \infty$. This corresponds to first deleting a period of length τ immediately following each event in the data series and then calculate the waiting time for the remaining series.

The possible cascading of events can be investigated by means of the conditional event rate $N_{F,c}(t, F_c)$ defined as the mean up-crossing rate at time t given that a crossing (up or down) took place at time $t = 0$. In order to calculate this we may use (4.8) with the conditional pdf $P(F(t), \dot{F}(t)|F(0))$, which is given by

$$P(F, \dot{F}|F_0) = \frac{1}{2\pi\sqrt{(1-r^2)R_F(0)D}} \exp\left[-\frac{\left(\dot{F} - \frac{\dot{r}(F_0 - rF)}{1-r^2}\right)^2}{2R_F(0)D} - \frac{(F - rF_0)^2}{2R_F(0)(1-r^2)}\right] \tag{4.21}$$

where

$$\begin{aligned} r &= R_F(t)/R_F(0) \\ D &= -\ddot{r}(0) - \frac{\dot{r}^2}{1-r^2} \end{aligned} \tag{4.22}$$

Inserting into (4.8) we find

$$\begin{aligned} N_{F,c}(t, F_c) = {} & \frac{1}{2\pi}\sqrt{\frac{D}{1-r^2}} \exp\left[\frac{\ddot{r}(0)(1-r)F_c^2}{2(1+r)R_F(0)D}\right] + \frac{F_c\dot{r}}{2\sqrt{2\pi R_F(0)(1-r)(1+r)^3}} \\ & \cdot \exp\left[-\frac{(1-r)F_c^2}{2(1+r)R_F(0)}\right] \left(1 + \operatorname{erf}\left[\frac{F_c\dot{r}}{(1+r)\sqrt{2DR_F(0)}}\right]\right) \end{aligned} \tag{4.23}$$

We are now in a position to calculate $M_F(F_c)$. Each realization that contains a crossing will also contain an up-crossing, and we may shift it in time so that a crossing takes place at $t = 0$. The shift does not affect the probability nor the number of up-crossings, therefore

$$M_F(F_c) = \int_0^T N_{F,c}(t, F_c)\, dt + \frac{1}{2} \tag{4.24}$$

The integral yields the number of up-crossings other than the one that might be at $t = 0$. There is a fifty-fifty chance that the crossing at $t = 0$ is an up-crossing, hence one half should be added.

For large t the conditional up-crossing rate $N_{F,c}(t, F_c)$ approaches the unconditional up-crossing rate $N_F(t, F_c)$, but for finite t it can be very different from it. This depends on the behavior of $R_F(t)$ in a quite complicated way, in

particular in the vicinity of $t = 0$. We recall that the derivatives of $R_F(t)$ for $t = 0$ are related to the variances of the derivatives of $F(t)$. Expressing $R_F(t)$ as a Taylor series we have

$$R_F(t) = \sum_{p=0}^{\infty} \frac{a_n\,(-1)^n\,t^{2n}}{(2n)!} \tag{4.25}$$

with

$$a_n = \left\langle \left(\frac{d^n F(t)}{dt^n} \right)^2 \right\rangle = \int S_F(\omega)\omega^{2n}\,d\omega = \int |\phi(\omega)|^2\,S(\omega)\omega^{2n}\,d\omega \tag{4.26}$$

where S_F is the spectrum. In (4.23) there are various terms that at a glance appear divergent for $t \to 0$, but they are in fact not. For example

$$\frac{\ddot{r}(0)(1-r)}{(1+r)D} = \frac{{a_1}^2}{{a_1}^2 - a_0\,a_2} + \frac{a_0\,a_1\,\left({a_2}^2 - a_1\,a_3\right)\,t^2}{18\left({a_1}^2 - a_0\,a_2\right)^2} + o(t^3) \tag{4.27}$$

It can be shown that both terms are negative so that the first term in (4.23) vanishes for $F_c \to \infty$ (instead of blowing up). Other terms are likewise well behaved and it can be shown that $M(F_c) \to 1$ for $F_c \to \infty$. However, a_3 appears in (4.27), so the approach to this limit is governed by the variance of the third derivative of F. Unless $S_F(\omega)\omega^6 \to 0$ fast enough for $\omega \to \infty$ we have a problem estimating a_3 directly from data because the value would depend on instrument characteristics. Therefore the filter function ϕ that defines F should effectively kill the high frequencies, i.e. $|\phi(\omega)|^2$ should roll off faster than ω^{-6}.

Returning to the example with the Ornstein-Uhlenbeck process we note that it has an infinite up-crossing rate, but a finite recurrence time. Equation (4.18) captures this behavior. To convince ourselves about this we convolute the correlation function (4.14) with a gaussian function $1/\sqrt{2\pi\mathcal{T}}\exp(-\frac{1}{2}t^2/\mathcal{T}^2)$ to get

$$R_{\mathcal{T}}(t) = \frac{1}{2}\mathrm{e}^{\mathcal{T}^2/2}\left\{\mathrm{e}^{-t}\left(1 + \mathrm{erf}\left[\frac{t-\mathcal{T}^2}{\sqrt{2}\mathcal{T}}\right]\right) + \mathrm{e}^{t}\left(1 - \mathrm{erf}\left[\frac{t+\mathcal{T}^2}{\sqrt{2}\mathcal{T}}\right]\right)\right\}. \tag{4.28}$$

It is necessary to do this filtering in order to get a finite $\ddot{r}(0)$ in (4.23). In fact all derivatives of r become finite. The filtered correlation function can now be used to evaluate (4.23) and (4.24) to get the recurrence rate (4.18). We find that recurrence rate λ approaches a constant, while the mean rate of up-crossings diverges as $\mathcal{T}^{-1/2}$ for the filter resolution going to zero, as expected looking at figure 24.

4.4 Data analysis

The Lammefjord and the Oak Creek experiments were selected for data analysis, see descriptions in Appendices A and B. The reason for selecting these sites is that turbulence at the Lammefjord site is as close to gaussian as it gets while at Oak Creak the turbulence is known to be rather non-gaussian (judged from skewness and kurtosis). The data are from cup anemometers at different heights. Figures 25 and 26 show spectra obtained from the data. It is noted that the spectra deviate substantially from conventional Kaimal spectra in the low frequency part, where there seems to be a $1/f$ range as discussed by Townsend (1979) and Kadar, Yaglom & Zubkovskii (1989).

We analyse the variable $v \equiv \frac{u-\bar{u}}{\bar{u}}$ and choose the 'spatial' variable $s \equiv \bar{u}t$ as independent variable instead of t. Fourier transforms are then expressed in terms of the wave number $k = \omega/\bar{u}$ instead of ω. This is done in order to preserve scaling of time. The data actually seem to obey this invariance and none of the statistical properties of $v(s)$ that have been investigated show any significant dependence on

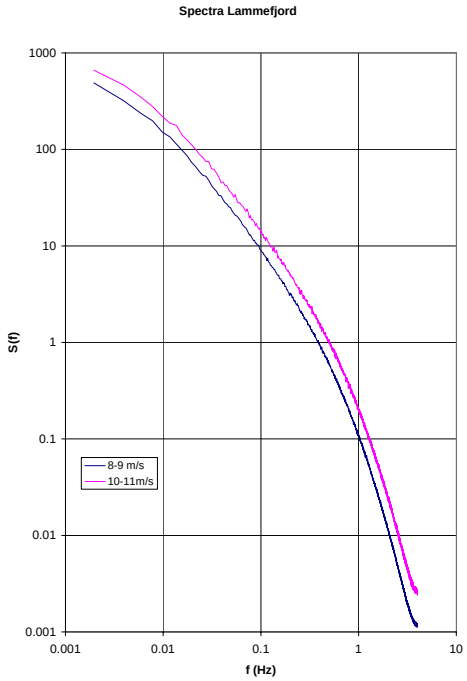

Figure 25. Spectra from the Lammefjord experiment.

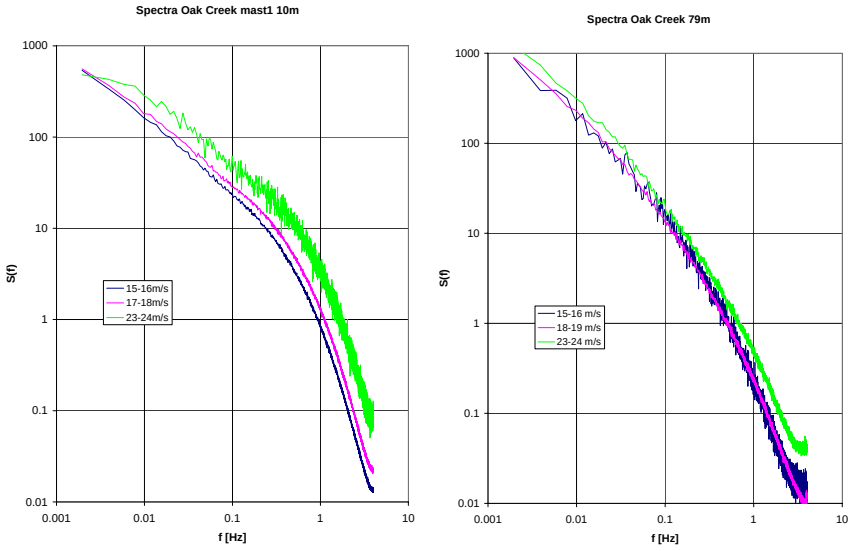

Figure 26. Spectra from the Oak Creek experiment.

$\bar{u}$. Figure 27 shows scatter plots of turbulence intensities (v and Δv are defined below). In these examples the trends with $\bar{u}$ are negligibly small.

The raw data series $u(t)$ (all sampled at 8Hz) were first filtered with a fourth order filter with a length scale l. In Fourier domain the filter transfer function can be expressed as $\psi_l(k) = \frac{1}{(1+ikl)^4}$, i.e. it is a first order filter applied four times. The reason for the high order is to eliminate event cascading as discussed above. Apart from v obtained with different filter constants, we investigate $\Delta v \equiv l\frac{dv}{ds}$. This variable has been chosen in order to emulate the response of a pitch regulated wind turbine (see example on page 54). Due to the smoothing of v by the filter

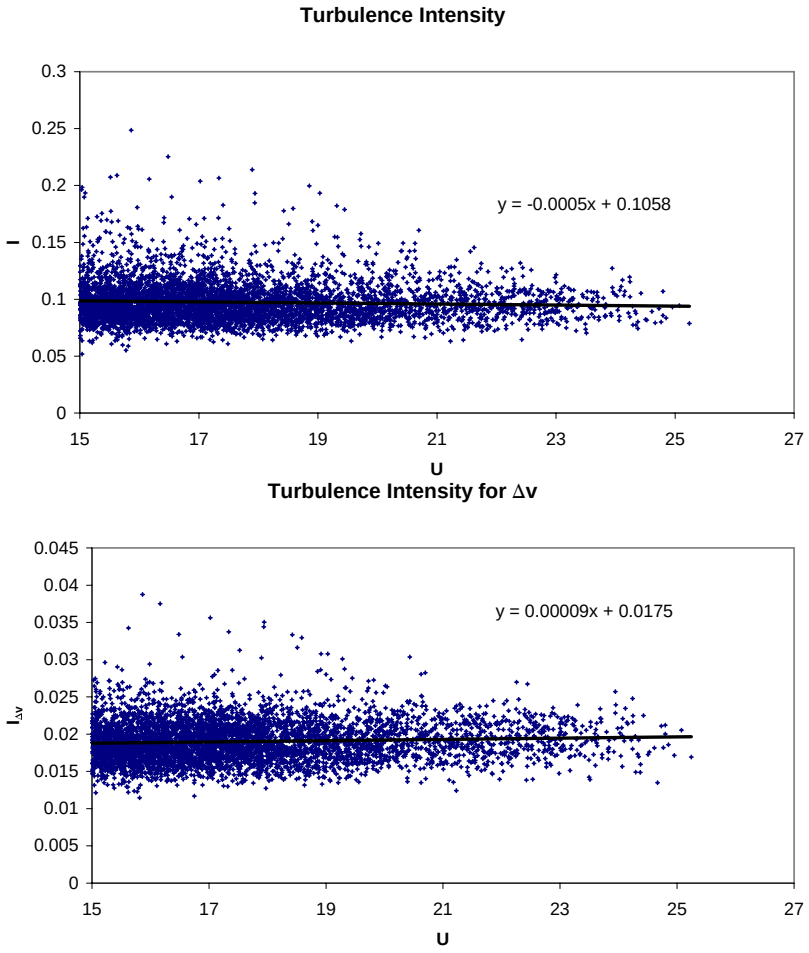

Figure 27. Turbulence intensities (standard deviations) of v (top) and Δv (bottom) vs. $\bar{u}$. Oak Creek, 10m. Filter length constant is $l = 2m$.

$\Delta v(s) \approx v(s + l/2) - v(s - l/2)$ is an excellent approximation and it is therefore permissible to think of Δv simply as a velocity difference.

As mentioned earlier (cfr. section 2) the pdf of v closely matches that of the local extrema of v, as expected for a Gaussian process, where v and $\dot{v}$ are independent. Despite non-Gaussianity this independence seem to be fulfilled almost exactly by the data, not even for v, but also for Δv. When v and $\dot{v}$ are independent, Rice's formula 4.8 reduces to

$$N_v(v) = \frac{1}{2} P_v(v) \left\langle \left| \frac{dv}{ds} \right| \right\rangle \tag{4.29}$$

for Δv and

$$N_{\Delta v}(\Delta v) = \frac{1}{2} P_{\Delta v}(\Delta v) \left\langle \left| \frac{d\Delta v}{ds} \right| \right\rangle \tag{4.30}$$

Since we use s rather than t these 'rates' come out as inverse meters and should be multiplied by $\bar{u}$ to get the real rate.

Figure 28 shows results for the Lammefjord data. Three curves are shown in each plot. The blue line is the measured 'rate'. The red is evaluated from (4.29) for v (left column) and (4.30) for Δv using the measured pdf and the measured values of $\langle |dv/ds| \rangle$ and $\langle |d\Delta v/ds| \rangle$). The green curve is the Gaussian result obtained from (4.12) or (4.30) using a Gaussian pdf. For v (left column) the Gaussian prediction is quite good for small vs, but ceases to fit at large vs, where it underpredicts by about a factor of ten. The gaussian prediction improves slightly as the filter

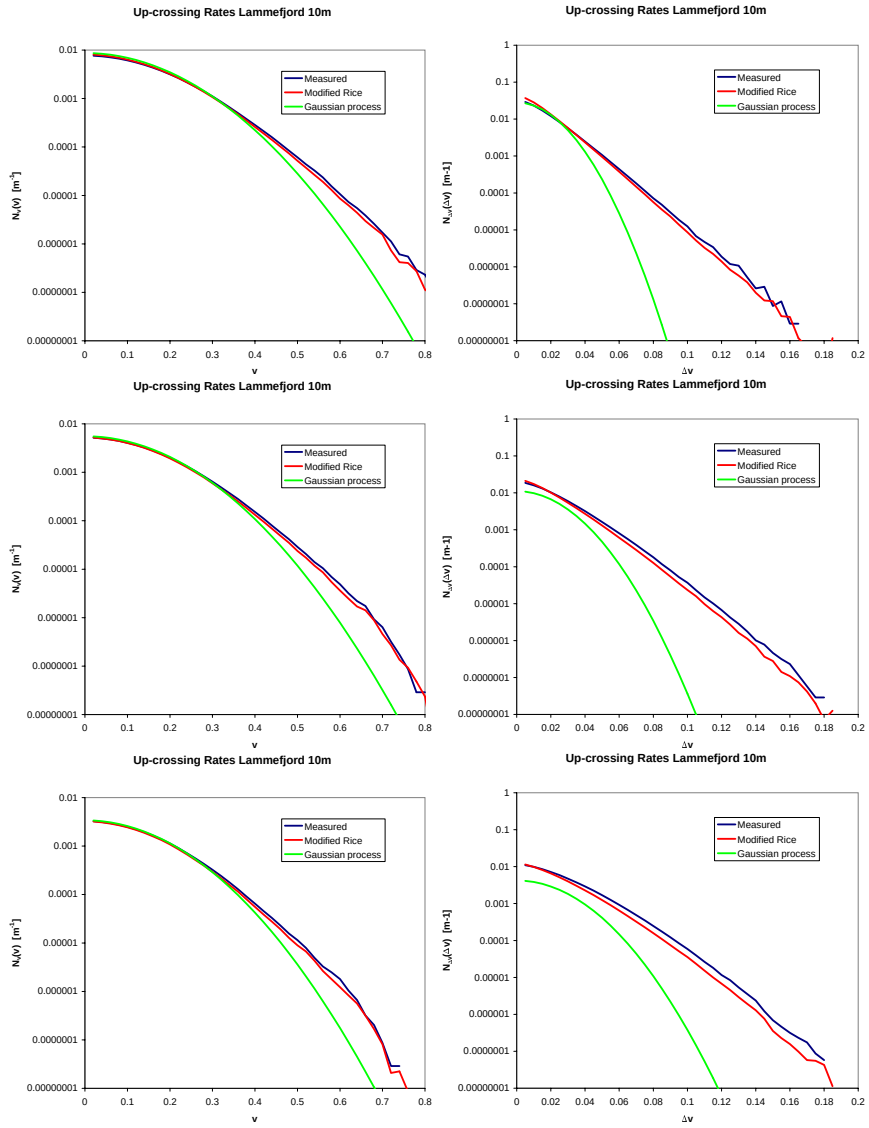

Figure 28. Up-cross rates of v (left) and Δv (right) for Lammefjord. Filter length constant: $l = 2m$ (top), $l = 4m$ (middle) and $l = 8m$ (bottom).

constant is increased, but the variation is only small. For Δv (right column) the Gaussian prediction is even worse, and the tails of the measured curves are close to exponentials (straight lines), especially for small l. In all cases the blue and the red curves match closely.

Figure 29 shows the same as figure 28 for data from Oak Creek and also at 10m. The graphs are very similar although v is more non-Gaussian for Oak Creek. The results for Δv are very similar for the two sites, and profoundly non-Gaussian.

Figure 30 shows results from Oak Creek at 79m. The trends are the same, but even more non-Gaussian in this case and the curves are all close exponentials.

These results show very large deviations from Gaussianity. For extreme events the Gaussian prediction of the event rate is far too low, in some cases many orders of magnitude below the measured value. It seems that non-Gaussianity predominantly resides on the small scales and has the most severe effect for rate of occurrence of extreme events. However, in the data the non-Gaussianity shows up as exponential tails. It seems plausible that the observed tails would continue being exponential if the data set were larger (Lammefjord covers approximately 1 year and Oak Creek almost 3 years). The simple exponential form therefore allows an

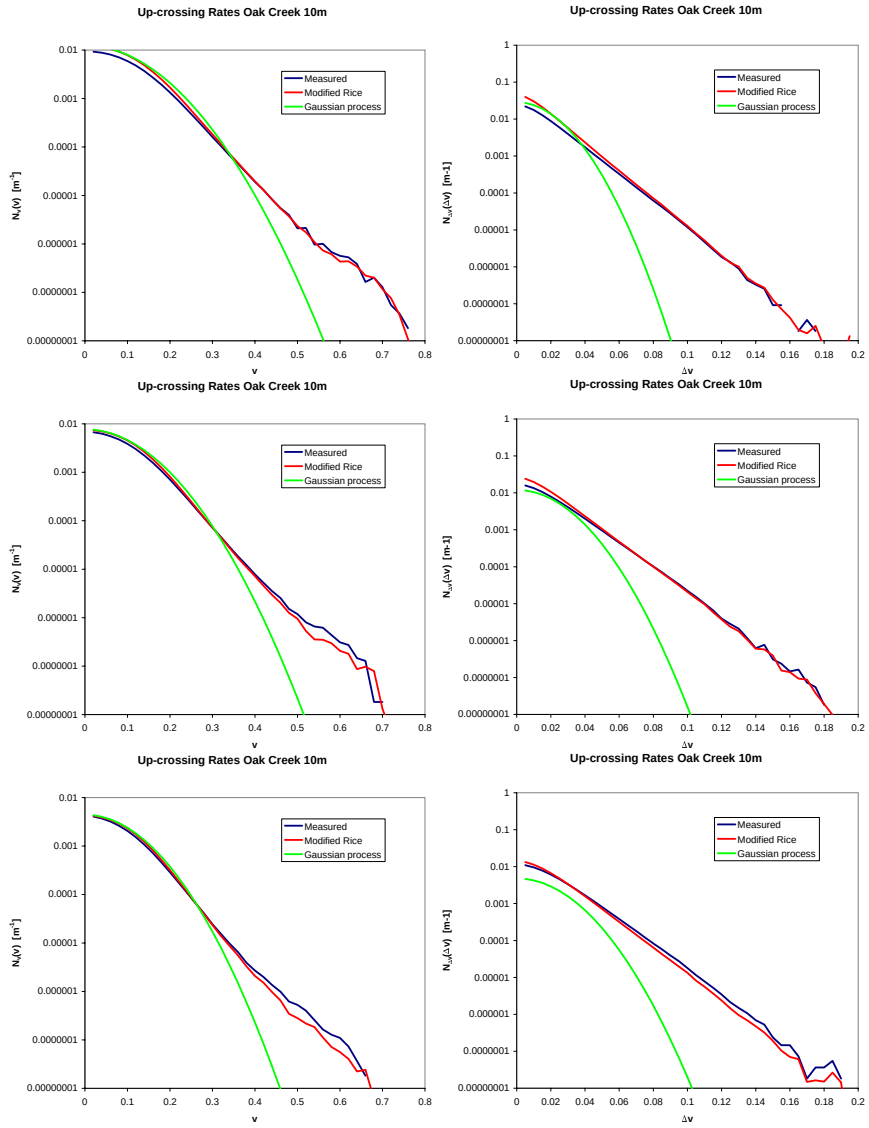

Figure 29. Up-cross rates of v (left) and Δv (right) for Oak Creek at 10m. Filter length consatant: $l = 2m$ (top), $l = 4m$ (middle) and $l = 8m$ (bottom).

extrapolation to more extreme events than covered by the data. However, extrapolation is always dangerous, and in this case we should be aware of the possibility of special and rare circumstances that could cause extreme events. Candidates are sudden wind changes in connection with cold front passages, downdraughts from thunder clouds, and in the tropics also tropical cyclones. These phenomena are governed by different physics than 'ordinary' gusts and may turn out to contribute to the tails if enough data is gathered. We also note that (4.29) and (4.30) work extremely well.

5 Front passages

Wind turbine load situations, like extreme coherent gust amplitudes and extreme direction changes can, among other, be associated with frontal passages. Unfortunately extreme situations, occurring during frontal passage, are extremely rare and seldom recorded. Examples of such situations, which demonstrate the mag-

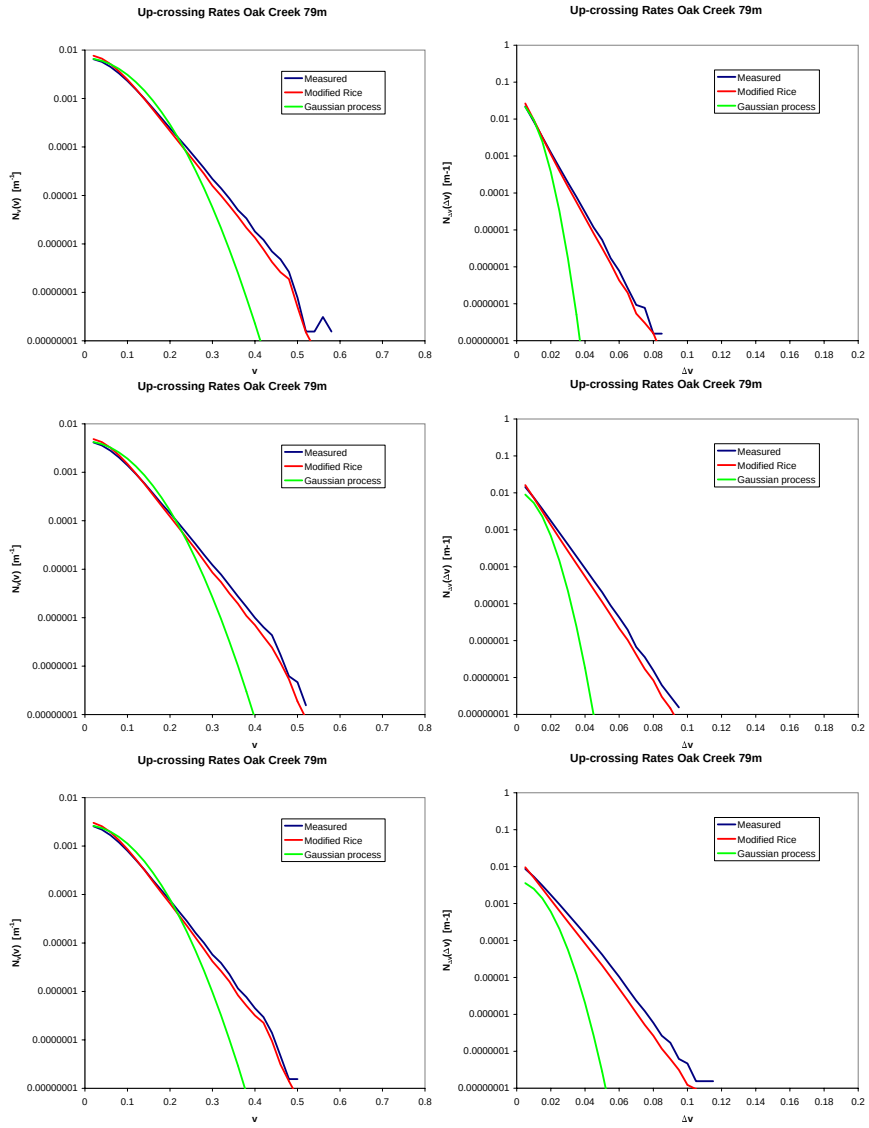

Figure 30. Up-cross rates of v (left) and Δv (right) for Oak Creek at 79m. Filter length constant: $l = 2m$ (top), $l = 4m$ (middle) and $l = 8m$ (bottom).

nitude and speed of such events, can be extracted from the IEA wind database (www.winddata.com).

Identification of frontal passages

A frontal passage is defined as a persistent level change in either the wind speed or in the wind direction. The time series are characterized with a number of statistical parameters like mean, standard deviation, minimum, maximum, skewness, kurtosis and a stationarity factor (SF) equal to the linear trend over a period of 10 minutes measured in m/s. A frontal passage might result in a high stationarity factor for either the wind speed signal, or for the wind direction signal, or a combination of these signals due to the level change.

A frontal passage can be characterized with 3 different values:

1. wind speed level shift, Δu (m/s),
2. rise time, Δt (s),
3. change in wind direction, $\Delta\theta$ (deg).

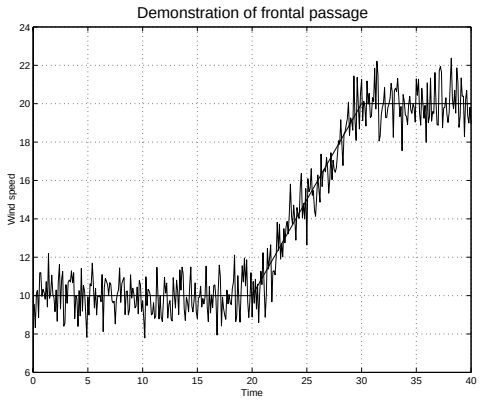

Figure 31. Demonstrates how the wind speed level shifts from 10 to 20 m/s as the result of a frontal passage.

The detection of frontal passages is based on the wind speed stationarity factor and has been limited to time series representing situations with SF $>$ 6. The extracted time series have been analysed, and this results in a limited number of time series, which are plotted on Figures 32–40. It is possible to determine the characteristic values Δu and Δt for each of the time series, which are listed in the figure captions. The remaining time series with SF $>$ 6 did not contain a distinct, clear level shift and have been omitted.

Discussion of the findings

All the resulting time series are shown on Figures 32–40, and each of these seems to represents a frontal passage. The level shifts for the resulting time series were larger than or equal to 9 m/s, but corresponds to a rather long rise time (15 - 180 s). The resulting accelerations were in the range from 0.1 - 0.9 m/s^2 during a period of 15 s as a minimum.

We were only able to identify 3 different extreme direction change cases, within this methods and the directional acceleration varies from 0.3 - 1.0 deg/s during a period of minimum 30 s

Conclusion

Only a very limited number of frontal passages, with a significant wind speed level shift, have been identified, and the accelerations seems not to be critical compared to the recommended extreme coherent gust amplitudes defined in the IEC 61400-1 standard.

Figure 32. Front passage: Middelgrunden (DK), $\Delta u = 5\mathrm{m/s}$*,* $\Delta t_u = 180\mathrm{s}$*,* $\Delta\theta = 70\mathrm{deg}$*,* $\Delta t_\theta = 250\mathrm{s}$.

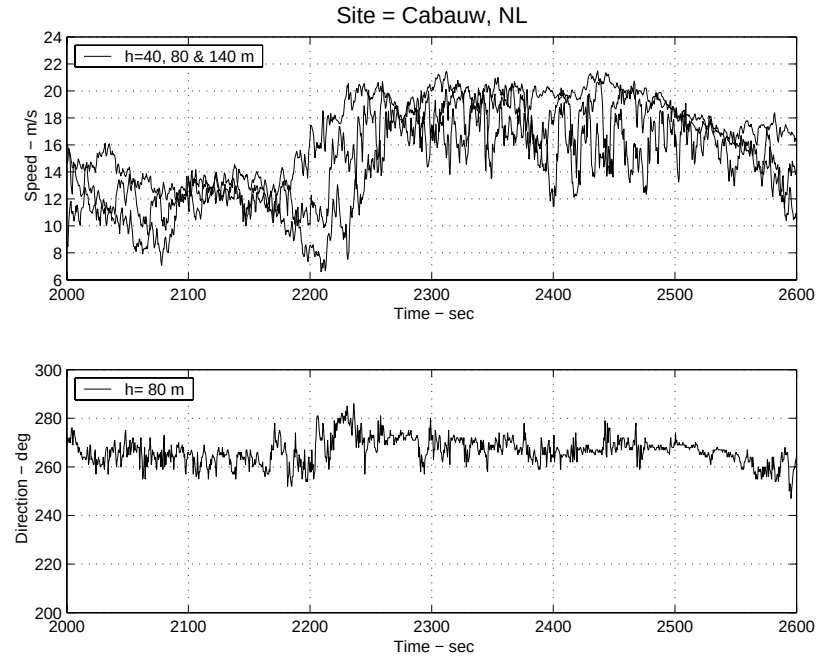

Figure 33. Front passage: Cabauw (NL), $\Delta u = 10\mathrm{m/s}$*,* $\Delta t_u = 70\mathrm{s}$*, insignificant directional change.*

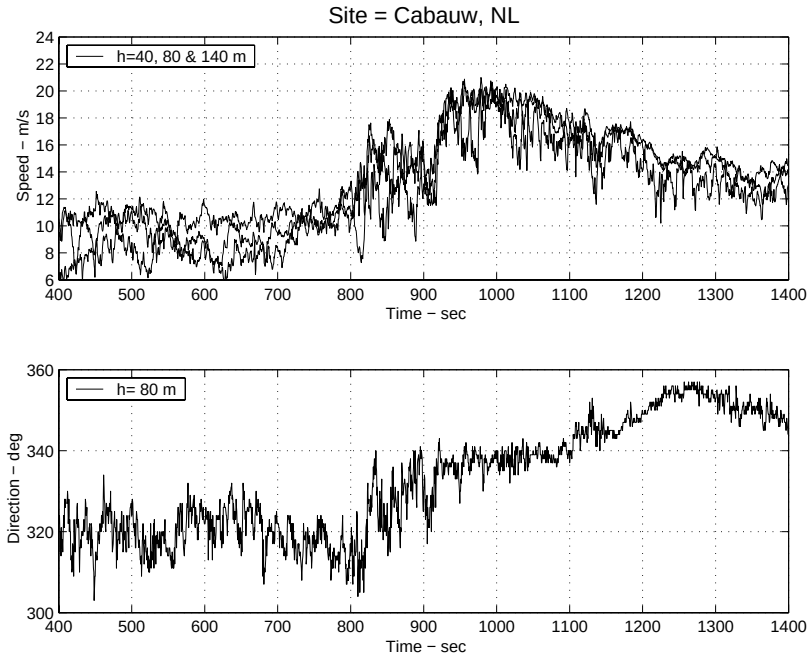

Figure 34. Front passage: Cabauw (NL), $\Delta u = 9\mathrm{m/s}$, $\Delta t_u = 100\mathrm{s}$, $\Delta\theta = 30\mathrm{deg}$, $\Delta t_\theta = 30\mathrm{s}$.

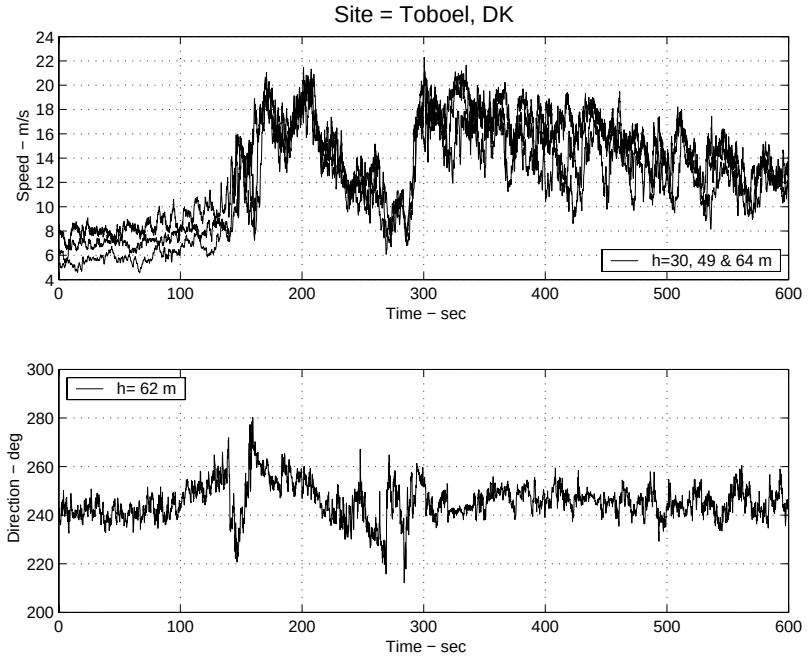

Figure 35. Front passage: Tobøl (DK), $\Delta u = 13\mathrm{m/s}$, $\Delta t_u = 15\mathrm{s}$, *insignificant directional change.*

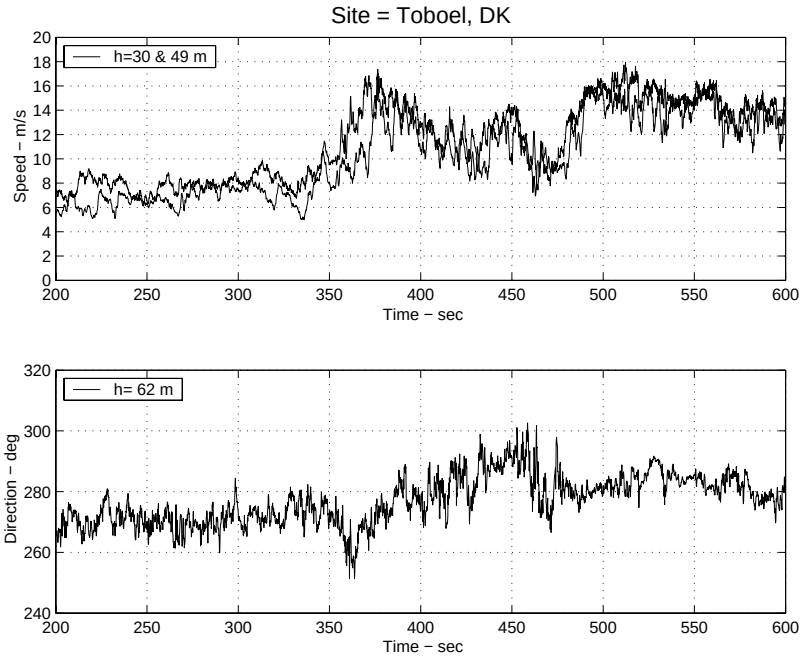

Figure 36. Front passage: Tobøl (DK), $\Delta u = 10\mathrm{m/s}$*,* $\Delta t_u = 35\mathrm{s}$*, insignificant directional change.*

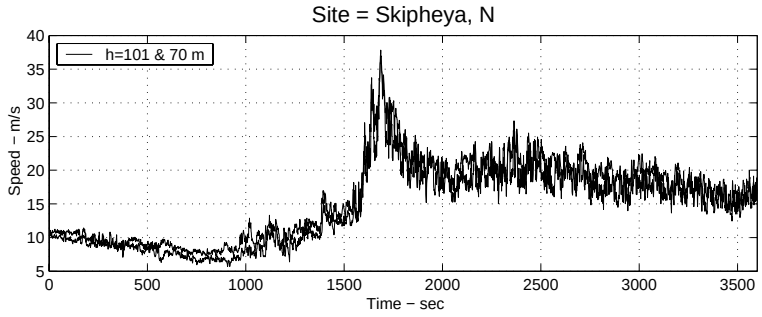

Figure 37. Front passage: Skipheya (N), $\Delta u = 23\mathrm{m/s}$*,* $\Delta t_u = 115\mathrm{s}$*.*

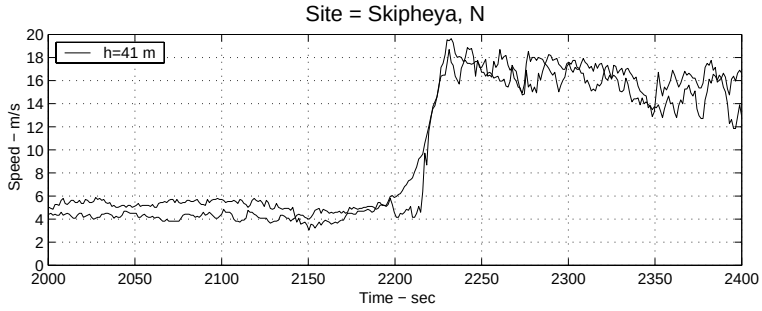

Figure 38. Front passage: Skipheya (N), $\Delta u = 11\mathrm{m/s}$*,* $\Delta t_u = 60\mathrm{s}$*.*

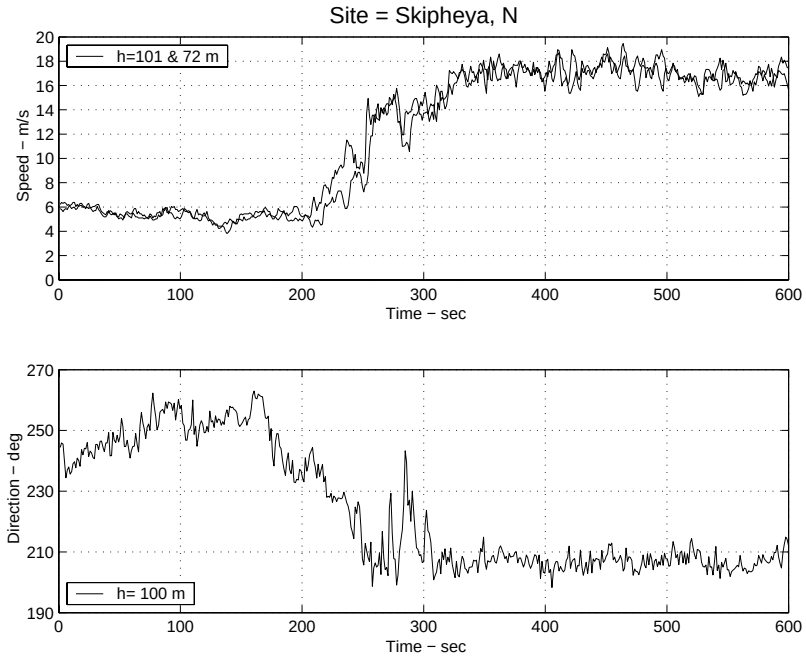

Figure 39. Front passage: Skipheya (N), $\Delta u = 12\mathrm{m/s}$, $\Delta t_u = 140\mathrm{s}$ $\Delta\theta = 45\mathrm{deg}$, $\Delta t_\theta = 110\mathrm{s}$.

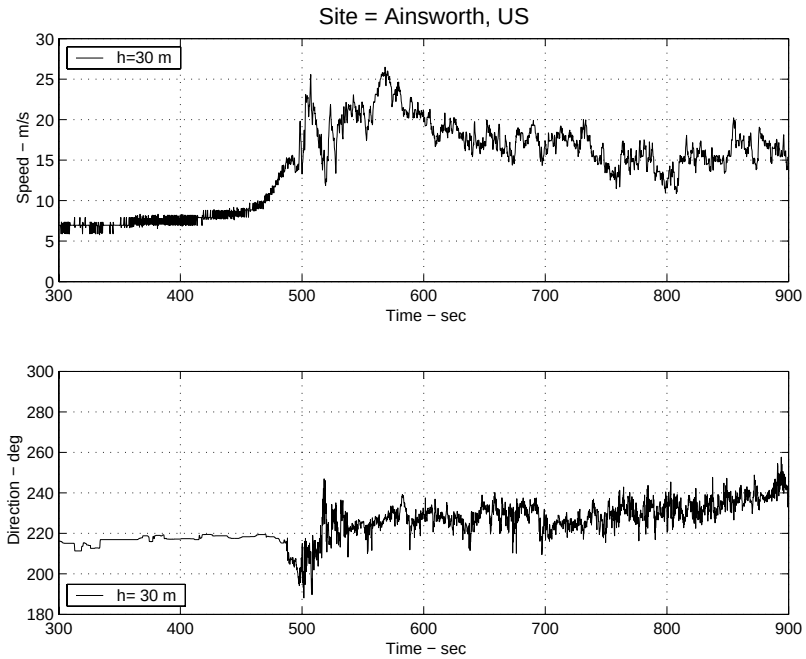

Figure 40. Front passage: Ainsworth (USA), $\Delta u = 10\mathrm{m/s}$, $\Delta t_u = 20\mathrm{s}$, *insignificant directional change.*

6 Simulation of extreme events

The present section deals with simulation of extreme events in a stochastic (turbulence) field. Both Gaussian and non–Gaussian fields are considered, however, with the main emphasis on the Gaussian case. As an introduction, the statistics of Gaussian processes are recapitulated, and the problem of a rational selection of extreme events is discussed. Subsequently, the formulation of constrained gusts in processes of various complexities is addressed.

6.1 The Gaussian generator

We have a generator of random, stationary, Gaussian time series, $v(t)$, according to a certain spectrum, and we wish to select extreme load situations. For simplicity we assume that $v(t)$ has zero mean, i.e.

$$\langle v(t) \rangle = 0\,, \tag{6.1}$$

where $\langle\rangle$ denotes the ensemble averaging operator. The conventional way to generate stationary, Gaussian time series is to sum random Fourier modes. Usually these are taken to be periodic with some period T, i.e. the frequencies are $\omega_k = 2\pi k/T$ with the integer k running from $-N$ to N. T should be larger than auto-correlation time scales, while T/N should be small compared to response times of the wind turbine.

Since the process is Gaussian, the probability that the generator yields the function $v(t)$ can be expressed as

$$P(\{v\}) = M \exp\left[-\frac{1}{2}\int\int dt'\,dt''\,v(t')\,Q(t'-t'')\,v(t'')\right]\,, \tag{6.2}$$

where M is a normalization constant (horrendously small or large), and the integration kernel Q is an even generalized function, which could involve δ-functions and derivatives of δ-functions. If we feel uneasy with this, we may change to discrete time and replace integrals with sums and get the familiar expression for a joint Gaussian probability density function

$$P(\{v\}) = M\,\exp\left[-\,v_i\,Q_{ij}\,v_j\right]\,. \tag{6.3}$$

The matrix Q_{ij} is the inverse of the correlation matrix defined as

$$R_{jk} \equiv \langle v_j\,v_k \rangle\,. \tag{6.4}$$

In other words

$$Q_{ij}\,R_{jk} = \delta_{ik}\,. \tag{6.5}$$

In continuous time this is written as

$$R(t-t') \equiv \langle v(t)\,v(t') \rangle\,, \tag{6.6}$$

and

$$\int Q(t-t')\,R(t'-t'')\,dt' = \delta(t-t'')\,. \tag{6.7}$$

We recall that the spectrum is defined as

$$S(\omega) = \frac{1}{2\pi}\int R(t)\mathrm{e}^{-i\omega t}\,dt\,. \tag{6.8}$$

In the below we shall use the following short notation

$$\begin{aligned} &\text{convolution:} \quad R*f(t) \;\equiv\; \int R(t-t')f(t')\,dt'\,,\\ &\text{inner product:} \quad (f,g) \;\equiv\; \int f(t)g(t)\,dt\,. \end{aligned} \tag{6.9}$$

6.2 The selection problem

The selected time series are to be subsequently analysed by means of an aeroelastic model. It can be expected that a 'normal' time series will not pose a problem, hence we should look for extreme and rare events. The problem is to generate extreme situations without having to generate excessive amounts of common, but uninteresting time series.

In order to select the right cases we need to know something about what we are looking for. One way of doing this would be to feed the aeroelastic model with a unit step load and observe the response $\Phi(t)$. The response could be e.g. the bending of a wind turbine blade, or it could be the strain in a structural member. In both of these examples there are upper critical values of the response (the tip of the blade hits tower, or the strength of the member is exceeded). In a simple *linear* model the derivative $\phi(t) = \Phi'(t)$ would be the response function, so that

$$f(t) = \int \phi(t-t')v(t')\,dt' = \phi * v(t) \tag{6.10}$$

would be the response for a general input $v(t)$. Aeroelastic models are generally non-linear but (6.10) could still be expected to yield a sensible selection criterion. If nothing is known, we could let ϕ be a δ-function, so that we simply look for a high wind speed. The important point is to avoid analyzing un-interesting cases, and be sure to select the interesting ones. In other words, the criterion $f(t) = f_c$ does not have to predict a critical situation with great precision (the aeroelastic model is supposed to do that), but $f(t) < f_c$ should indicate a safe situation.

6.3 Gaussian gust in a single process

Suppose we have chosen (6.10) as the selection criterion and want to generate time series for which $f(t_0)$ attains some critical value f_c. We may assume that $t_0 = 0$ without loss of generality. The most probable time series, $v_g(t)$, fulfilling $f(0) = f_c$ can be found by

$$\text{minimizing} \qquad \int\int dt'\,dt''\,v_g(t')\,Q(t'-t'')\,v_g(t'')\,, \tag{6.11}$$

$$\text{subject to the condition} \qquad \int \phi(-t')\,v_g(t')\,dt' = f_c\,. \tag{6.12}$$

We note, that for Gaussian processes the most probable time series is equal to the mean value of all time series fulfilling the condition. We may therefore refer to $v_g(t)$ as the mean gust corresponding to the condition. Variational calculus yields

$$\int Q(t-t'')\,v_g(t'')\,dt'' = \lambda\,\phi(-t)\,, \tag{6.13}$$

where λ is a Lagrangian multiplier to be determined. Convoluting both sides with R and using (6.7) and (6.12) we obtain the solution

$$v_g(t) = \frac{f_c}{\int\int dt'\,dt''\,\phi(-t')\,R(t'-t'')\,\phi(-t'')} \int R(t-t')\,\phi(-t')\,dt'$$

$$= \frac{f_c}{(\phi, R*\phi)}\,R * \check{\phi}\,, \tag{6.14}$$

where the short hand notation (6.9) has been introduced and $\check{\phi}(t) \equiv \phi(-t)$.

Time series obeying the condition $(v, \check{\phi}) = f_c$ can be generated by the following very simple method. First the Gaussian generator is used to make a time series

$w(t)$ (without any conditions). Then w is modified by adding a multiple of v_g so that the condition is fulfilled. In this way we end up with

$$v = w + \frac{f_c - (\phi, w)}{f_c}\, v_g = w + \frac{f_c - (\phi, w)}{(\phi, R * \phi)}\, R * \check{\phi}\,. \tag{6.15}$$

Apart from fulfilling the condition $(v, \check{\phi}) = f_c$, the time series is also generated at the correct rate. In order to demonstrate this we first note that those time series that end up as v via (6.15) are of the form $w = v + s\, v_g$, where s can be any real number. Therefore the method generates v at a rate proportional to $\int P(\{v + sv_g\})\, ds$. Using (6.7) and (6.14) we find that

$$(v + sv_g, Q(v + sv_g)) = (v, Qv) + (2s + s^2)\frac{f_c^2}{(\phi, R * \phi)}\,. \tag{6.16}$$

Hence $\int P(\{v + sv_g\})\, ds$ is proportional to $P(\{v\})$ as it should be.

Application of the theory outlined above is illustrated in three examples. The first two examples relates to wind events defined without any a priori knowledge to the response function of the structure on which the gust shall be imposed, whereas the third example discuss critical gust shapes based on knowledge to the system to which the gust shall be imposed.

The turbulence description in the examples are based on the von Kármán spectrum. The spectrum of the component of the wind fluctuations in the direction of the mean wind is

$$F_u(k_1) = \frac{9}{55}\alpha\varepsilon^{2/3}\frac{1}{(L^{-2} + k_1^2)^{5/6}}\,, \tag{6.17}$$

where α is the spectral Kolmogorov constant (≈ 1.7), ε the energy dissipation, L a length scale and k_1 the wave number $= 2\pi f/U$, with f the frequency and U the mean wind speed. The spectrum is normalized such that $\int_{-\infty}^{\infty} F_u(k_1)dk_1$ is equal to the variance. A stationary Gaussian simulation, which has this spectrum, is done by Fourier simulation as described in Section 3.1. The correlation function corresponding to the von Kármán spectrum is

$$R_u(x) = \frac{2^{2/3}9}{55\sqrt{\pi}\Gamma\left(\frac{5}{6}\right)}\alpha\varepsilon^{2/3}(xL)^{1/3}K_{\frac{1}{3}}(x/L)\,, \tag{6.18}$$

where $\Gamma(\cdot)$ denotes the Gamma function, and $K_{\frac{1}{3}}(\cdot)$ is the Bessel function of second kind of order 1/3.

Figure 41 shows an example of this with typical atmospheric parameters ($L =$ 100 m, $\alpha\varepsilon^{2/3} = 0.1$). In the simulation a wind speed is calculated every 0.5 m corresponding to a sampling frequency of 20 Hz for a mean wind speed of $U =$ 10 m/s. $N = 2^{15}$ points are simulated corresponding to half an hour. In Figure 41 only two minutes are shown.

A simulation with a different seed to the random number generator is shown in Figure 42.

Example 6.3.1: A gust

The simplest sensible selection criterion is perhaps that $v(t_0)$ should attain some (large) critical value v_c. We therefore let

$$\phi(t) = \delta(t - t_0)\,, \tag{6.19}$$

and $f_c = v_c$. This leads to

$$v_g(t) = \frac{v_c\, R(t - t_0)}{R(0)}\,. \tag{6.20}$$

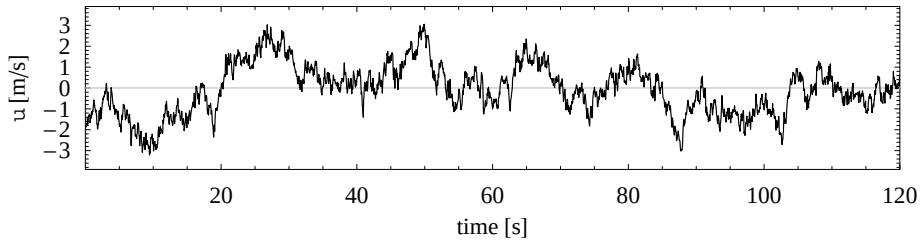

Figure 41. Fourier simulation of a stationary time series with a von Kármán spectrum.

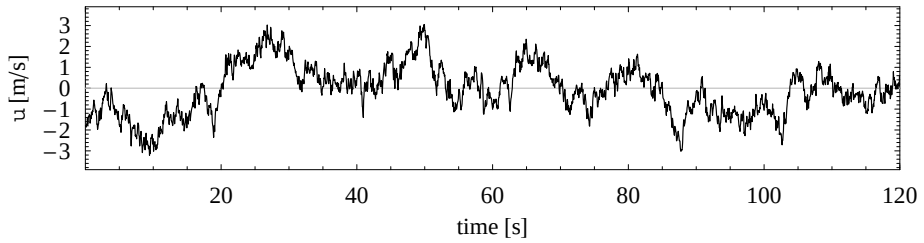

Figure 42. A different realization of the simulation. See Figure 41.

Figure 43 shows a Gaussian simulation with the constraint $u(60\text{ s}) = 5\sigma_u$, and in Figure 44 the condition is the rather extreme $u(60\text{ s}) = 20\sigma_u$. The seed to the random number generator is the same as in Figure 41, so the difference is deterministic and given by equation (6.14).

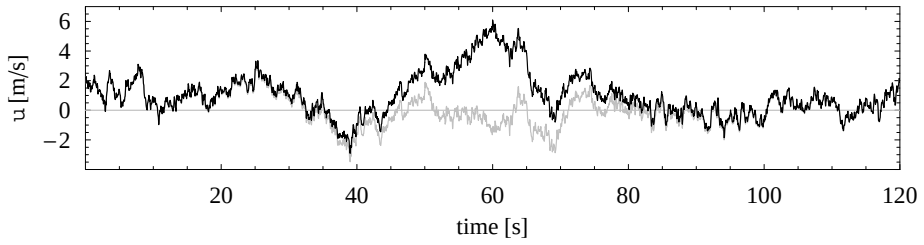

Figure 43. Similar to Figure 41 but with $\phi(t) = \delta(t - 60\text{s})$. f_c is 5 times the standard deviation of the stationary series.

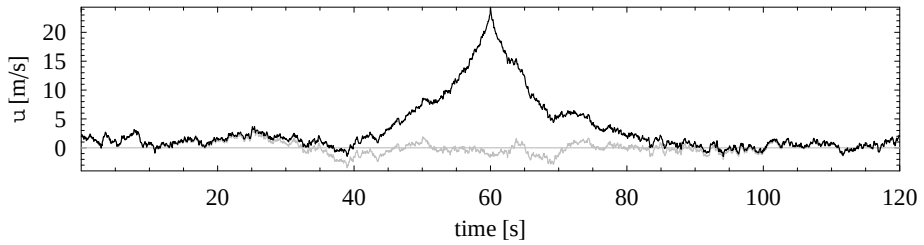

Figure 44. Same as Figure 43 but with $f_c = 20\sigma_u$.

Example 6.3.2: A velocity jump

Another relatively simple example relates to situations where the wind speed makes a jump during a time span $t_2 - t_1$, so that $v(t_2) - v(t_1) = \Delta v_c$. In this case we choose

$$\phi(t) = \delta(t - t_2) - \delta(t - t_1) \tag{6.21}$$

and get

$$v_g(t) = \frac{\Delta v_c \, (R(t - t_2) - R(t - t_1))}{2(R(0) - R(t_2 - t_1))} \tag{6.22}$$

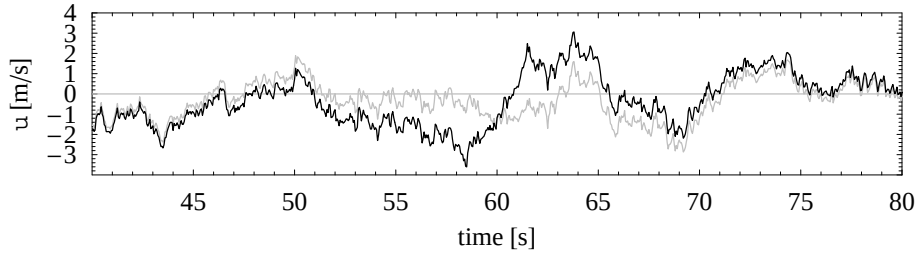

Figure 45. Simulation of velocity jump.

A jump of size $\Delta u(t) \equiv u(t + \Delta t/2) - u(t - \Delta t/2) = 5\sigma_u$ and with $\Delta t = 3$ s is shown in Figure 45. An other way to define a jump is $\Delta u_T(t) \equiv u_T(t + \Delta t/2) - u_T(t - \Delta t/2)$, where $u_T(t) = 1/T \int_{-T/2}^{T/2} u(t + t')dt'$, T being an averaging time. A simulation with $T = 1.5$ s and $\Delta u_T = 5\sigma_u$ is shown in Figure 46. The difference is that the latter jump is not so steep but slightly larger.

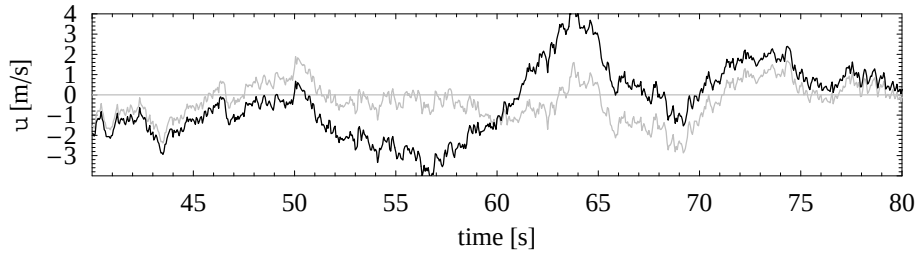

Figure 46. Simulation of velocity jump defined differently from the one in Figure 45

Example 6.3.3: Critical gusts

In the present example we illustrate the use of a constraint in a more specific case. Suppose we want to analyse a situation where a pitch-regulated wind turbine is hit by a gust, while it is operating. Starting with the wind speed measured at hub height $\bar{v}+v(t)$ we assume that the thrust on a blade can be described by the filtered velocity $U = \bar{v} + \phi_1 * v$. The filter function ϕ_1 should have a characteristic time scale, τ, which takes spatial averaging and aerodynamic response into account. $U(t)$ can be determined by measuring the production and the pitch and is thus available as input to the pitch regulator. The pitch, we imagine, is regulated so as to maximize the production at the wind speed W, i.e the regulator tries to make $W = U$. We assume that this is done by a simple proportional regulation so that

$$\frac{dW(t)}{dt} = \frac{U(t) - W(t)}{\tau_2}\,, \tag{6.23}$$

where τ_2 is another time constant. The optimum value for τ_2 is close to τ. Production is lost if $\tau_2 \gg \tau$, and the system gets 'nervous' if $\tau_2 \ll \tau$ and wears itself down. For the sake of simplicity we therefore assume that $\tau_2 = \tau$. Equation (6.23) implies that $W = \phi_2 * u$, where $\phi_2(t) = \theta(t)\mathrm{e}^{-t/\tau}/\tau$ is the usual first order filter function with

$$\theta(t) = \begin{cases} 1 & \text{for } t \geq 0 \\ 0 & \text{for } t < 0 \end{cases} . \tag{6.24}$$

Now a dangerous situation could occur if U increases rapidly while W is low. In that case the turbine is tuned to maximize the production at a low wind speed, and the gust may force the blade into the tower. This could be calculated in detail using an aeroelastic model, but we simply take the 'mis–regulation' $f(t) = U(t) - W(t)$ as an indicator of bad forcing of the blades. From (6.23) we find

$$f = \tau \frac{dW}{dt} \equiv \phi * v \,, \tag{6.25}$$

where

$$\phi = \frac{d\,\phi_2 * \phi_1}{dt} \,. \tag{6.26}$$

Both ϕ_1 and ϕ_2 are low pass filters, and the derivative represents a high pass filter. We could go on and add a second order filter to evaluate the deflection of a blade in response to the forcing, e.g. a second order low pass filter like the response function of a damped harmonic oscillator. In any case we end up with a ϕ which looks like the derivative of a low pass filter of quite high order (4), e.g. $\phi(\omega) \sim \frac{i\omega}{(1+i\omega\tau)^4}$. The derivative ($i\omega$ factor), cutting off low frequencies, is due to the effect of the regulation. The corresponding most probable gust is proportional to $R * \check{\phi}$. Figure 47 shows an example, where $\phi(\omega) = \frac{1}{2\pi}\frac{i\omega}{(1+i\omega)^2}$ and $R(t) = \mathrm{e}^{-|t|}$ setting $\tau = 1$. The gust starts going down, reaches a relatively shallow minimum and then rises rather fast to a maximum. The same general shape is found for higher order filters. The reason why this particular shape is critical must be that the regulator is 'fooled' to adjust the pitch to a low wind speed, which makes the system extra vulnerable to the gust that follows.

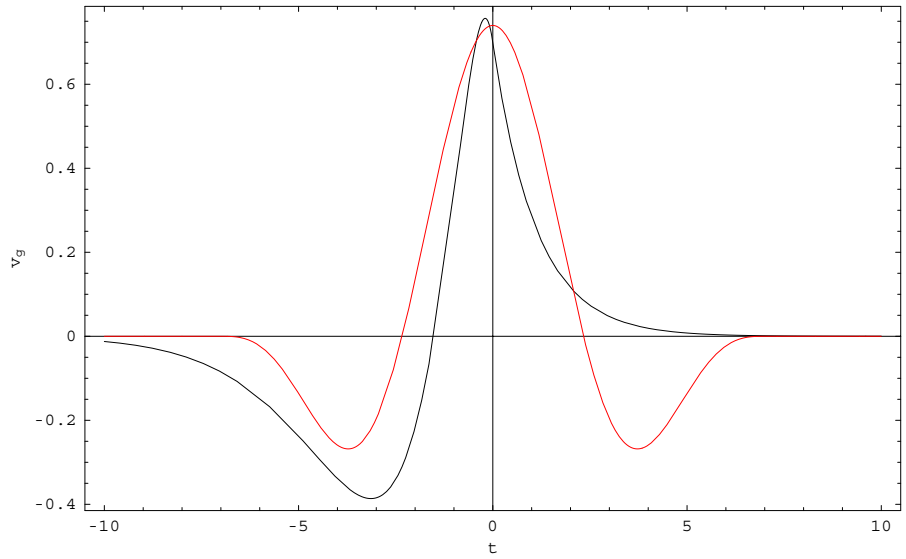

Figure 47. Black line: The mean gust in the simple model for pitch regulation. Red line: 'Extreme Operational Gust' as specified in IEC 64100-1.

We note the similarity to the 'extreme operational gust' (EOG) prescribed by the IEC 61400-1 code for this kind of load situations. The EOG also goes down before reaching a maximum. After the maximum the EOG is different, but this part is not very interesting, because any damage to the wind turbine surely happens *before* the maximum is reached. Our example is oversimplified, but even so it indicates that a simple linear indicator such as (6.25) could be useful. Not only is it associated with a mean gust, which can be used in the same way as the EOG, but we also get a chance to make statistical analysis showing how often f can be expected to exceed a critical level. The method also allows to take characteristics of the turbine and the turbulence at a specific site into account.

6.4 Gaussian gusts in multiple correlated processes

The previous section outlines the theory for generation of *one* gust event in *one* Gaussian stationary stochastic process. This theory is in the present section generalized to gust events associated with N jointly Gaussian stochastic processes subjected to M constraints involving an arbitrary number of (time separated) gust events in each process.

Without restrictions we, again for simplicity, assume that each of the stationary processes has zero mean, i.e.

$$\langle \mathbf{v}(t) \rangle = \mathbf{0}\,, \tag{6.27}$$

where the vector process $\mathbf{v}^T(t) = (v_1(t), \ldots, v_N(t))$ has been introduced, and $\mathbf{0}$ is the zero vector. An upper index T denotes transpose. In the following, a *bold lower case* letter denotes a vector, whereas a *bold upper case* letter will denote a matrix. As the considered processes are assumed joint Gaussian, the probability of the field $\mathbf{v}(t)$ resulting from a generator of random, stationary, Gaussian fields can, in analogy with equation (6.2) be expressed as

$$P(\{\mathbf{v}\}) = M \exp\left[-\frac{1}{2}\int\int dt'\,dt''\,\mathbf{v}^T(t')\,\mathbf{Q}(t'-t'')\,\mathbf{v}(t'')\right]\,, \tag{6.28}$$

where

$$\int \mathbf{R}(t-t')\,\mathbf{Q}(t'-t'')\,dt' = \mathbf{I}\delta(t-t'')\,, \tag{6.29}$$

with

$$\mathbf{R}(t-t') \equiv \left\langle \mathbf{v}(t)\,\mathbf{v}^T(t') \right\rangle\,, \tag{6.30}$$

and $\mathbf{I}$ denoting the identity matrix. Note, that $\mathbf{R}$ as well as $\mathbf{Q}$ is symmetric, and therefore

$$\int \mathbf{R}(t-t')\,\mathbf{Q}(t'-t'')\,dt' = \int \mathbf{Q}(t'-t'')\,\mathbf{R}(t-t')\,dt'\,. \tag{6.31}$$

The filter matrix function $\mathbf{\Phi}(t)$ defines the M selected constraints, $\mathbf{f}_c^T = (f_{c_1}, \ldots, f_{c_M})$, through the relation

$$\mathbf{f}_c = \int \mathbf{\Phi}(t'')\,\mathbf{v}_g(t'')\,dt''\,. \tag{6.32}$$

Note, that the constraints defined as above are *linear* in the vector process, and that the matrix function $\mathbf{\Phi}(t)$ is in general not quadratic but a M×N matrix.

The most probable field, $\mathbf{v}_g(t)$, fulfilling equation (6.28) subjected to constraints as defined by equation (6.32), is determined by the variational problem

$$\int\int dt'\,dt''\,\mathbf{v}_g^T(t')\,\mathbf{Q}(t'-t'')\,\delta\mathbf{v}_g(t'') - \boldsymbol{\lambda}^T \int \mathbf{\Phi}(t'')\,\delta\mathbf{v}_g(t'')\,dt'' = 0\,, \tag{6.33}$$

where M Lagrange multipliers, corresponding to each of the M constraints, have been introduced and collected in the vector $\boldsymbol{\lambda} = (\lambda_1, \ldots, \lambda_M)$. Selecting $\delta \mathbf{v}_g(t'')$ as $\delta(t - t'')\mathbf{1}$, where $\mathbf{1} \equiv (1, \ldots, 1)$ (note, that δ in the last context denotes the Dirac function), the equations in (6.33) de-couple and reduce to

$$\int dt' \, \mathbf{v}_g^T(t') \, \mathbf{Q}(t' - t) = \boldsymbol{\lambda}^T \, \boldsymbol{\Phi}(t) \, . \tag{6.34}$$

The requested field, $\mathbf{v}_g(t)$, is then obtained by convoluting (6.34) with $\mathbf{R}$. Thus

$$\int \int dt \, dt' \, \mathbf{v}_g^T(t') \, \mathbf{Q}(t' - t) \, \mathbf{R}(t - t'') = \boldsymbol{\lambda}^T \int dt \, \boldsymbol{\Phi}(t) \, \mathbf{R}(t - t'') \, , \tag{6.35}$$

which, by introduction of equations (6.29) and (6.31), is reduced to

$$\mathbf{v}_g^T(t'') = \boldsymbol{\lambda}^T \int dt \, \boldsymbol{\Phi}(t) \, \mathbf{R}(t - t'') \, , \tag{6.36}$$

or

$$\mathbf{v}_g(t'') = \int \mathbf{R}(t - t'') \, \boldsymbol{\Phi}^T(t) \, dt \; \boldsymbol{\lambda} \, , \tag{6.37}$$

where the symmetry of $\mathbf{R}$ has been utilized. Note, that $\boldsymbol{\Phi}$ is not symmetric and in general not even quadratic. The Lagrange multipliers are determined by introducing equation (6.37) into equation (6.32), whereby the following expression is obtained

$$\mathbf{f}_c = \int \int dt'' \, dt \, \boldsymbol{\Phi}(t'') \, \mathbf{R}(t - t'') \, \boldsymbol{\Phi}^T(t) \; \boldsymbol{\lambda} \, , \tag{6.38}$$

from which $\boldsymbol{\lambda}$ is derived as

$$\boldsymbol{\lambda} = \left(\int \int dt'' \, dt \, \boldsymbol{\Phi}(t'') \, \mathbf{R}(t - t'') \, \boldsymbol{\Phi}^T(t) \right)^{-1} \; \mathbf{f}_c \, . \tag{6.39}$$

Finally, introducing the short hand notation

$$\mathbf{T} = \int \int dt'' \, dt \, \boldsymbol{\Phi}(t'') \, \mathbf{R}(t - t'') \, \boldsymbol{\Phi}^T(t) \, , \tag{6.40}$$

equation (6.37) is finally formulated as

$$\mathbf{v}_g(t'') = \int \mathbf{R}(t - t'') \, \boldsymbol{\Phi}^T(t) \, dt \; \mathbf{T}^{-1} \, \mathbf{f}_c \, . \tag{6.41}$$

The matrix $\mathbf{T}$ is a M×M matrix, and it has an inverse (provided that the constraints defined are linear independent) even though this is in general not true for $\boldsymbol{\Phi}$ and $\boldsymbol{\Phi}^T$. Note, that equation (6.41) describes the ensemble mean gust shape of the most probably stochastic field satisfying the imposed constraints.

In case of un-correlated processes, $\mathbf{R}(t - t')$ as well as $\mathbf{Q}(t' - t'')$ degenerate to diagonal matrices, which obviously simplifies the (numerical) handling of the constrained simulation problem involving more processes considerably.

Having derived expression (6.41) for the most probable gust field time sequence, satisfying the constraints (6.32), this sequence is embedded in the un–constrained Gaussian field, $\mathbf{v}(t)$, in a straight forward way by first removing the components of the constraints already present in the Gaussian field, and then subsequently replacing the removed element by the requested constrained sequence (6.41). Using equation (6.32), the resulting field, $\mathbf{v}_r(t)$, is finally given by

$$\mathbf{v}_r(t) = \mathbf{v}(t) + \int \mathbf{R}(t' - t) \, \boldsymbol{\Phi}^T(t') \, dt' \; \mathbf{T}^{-1} \left(\mathbf{f}_c - \int \boldsymbol{\Phi}(t') \, \mathbf{v}(t') \, dt' \right) . \tag{6.42}$$

A special case of the above is the case where one process is subjected to an arbitrary number of time separated constraints. An extreme example of this kind

is the situation where all points in a measured signal is included in the definition of the constraints. In this case the present system will produce a field equivalent to the field produced by conditional simulation described in Section 3.5 of the present report. An other related application of the theory is extrapolation of a given sample of a process.

As indicated, the derived simulation methodology is extremely flexible. An example of a more unconventional application is design of gusts that have pre–described *ensemble mean* shapes. This is, however, only possible in the case where the filter matrix is diagonal, i.e. gust conditions for the involved processes are decoupled. The starting point is equation (6.41). The left hand site is assumed known (the ensemble gust shapes), and the task is to define a suitable filter matrix such that equation (6.41) is fulfilled. It is convenient to formulate the problem in the Fourier space, as the convolution in (6.41) then is replaced by a multiplication. Noting that $\mathbf{T}^{-1}\,\mathbf{f}_c$ is a constant M–dimensional vector, and denoting the complex Fourier transform by an over–tilde we obtain

$$\tilde{\mathbf{v}}_g(\omega) = \tilde{\mathbf{R}}(\omega)\,\tilde{\mathbf{\Phi}}^T(\omega)\;\mathbf{T}^{-1}\,\mathbf{f}_c\,, \tag{6.43}$$

from which the Fourier transform of the requested filter matrix is readily derived as

$$\tilde{\mathbf{\Phi}}^T(\omega) = \tilde{\mathbf{R}}^{-1}(\omega)\,\tilde{\mathbf{v}}_g(\omega)\;\left(\left(\mathbf{T}^{-1}\,\mathbf{f}_c\right)^{-1}\right)^T\,, \tag{6.44}$$

where the vector $\left(\mathbf{T}^{-1}\,\mathbf{f}_c\right)^{-1}$ denotes the vector with elements equal to the inverse of the elements in $\mathbf{T}^{-1}\,\mathbf{f}_c$.

Applying the inverse Fourier transform to equation (6.44), we obtain the following equivalent expression in the time domain for the requested filter matrix

$$\mathbf{\Phi}^T(t) = \int \mathbf{R}^{-1}(t'-t)\,\mathbf{v}_g(t')\,dt'\;\left(\left(\mathbf{T}^{-1}\,\mathbf{f}_c\right)^{-1}\right)^T\,. \tag{6.45}$$

An alternative strategy for obtaining a stochastic field with a pre–described gust shape embedded is based on wavelet transformation (Larsen, Hansen & Pedersen 2002). A relatively simple example, related to the IEC–64100 Extreme Operational Gust wind turbine load case, is described in Appendix D.

Simulation of stochastic fields are often formulated in the Fourier space, as the input to these simulations, as e.g. spectral tensors or spectra and coherence functions, are formulated in the Fourier space. The analogy to equation (6.42) in the Fourier space is

$$\tilde{\mathbf{v}}_r(\omega) = \tilde{\mathbf{v}}(\omega) + \tilde{\mathbf{R}}(\omega)\,\tilde{\mathbf{\Phi}}^T(\omega)\;\mathbf{T}^{-1}\;\left(\mathbf{f}_c - \int \mathbf{\Phi}(t')\,\mathbf{v}(t')\,dt'\right)\,. \tag{6.46}$$

Two classes of external wind load conditions are traditionally considered in a wind turbine design process – fatigue loading and ultimate loading. The extreme load conditions specified in design codes reflect, among other things, peak loading caused by rapid changes in wind speed and direction. In the codes, these load cases are specified as deterministic and coherent events. A more physical consistent modeling of these load cases can be obtained as special cases of the theory outlined above.

The capabilities of the theory outlined is illustrated in the examples below covering 1D as well as 3D simulations. The Gaussian simulation in the 1D situation use a turbulence description based on the von Kármán spectrum and is analogue to the description used in the examples shown in the previous section. The three-dimensional homogeneous simulations are done according to (Mann 1998). The addition of the constraints are done according to equation (6.42) by substituting the integrals with finite sums. As with the one-dimensional examples $\alpha\varepsilon^{2/3}$ is 0.1.

In all examples wind is simulated in a square representing the rotor plane of 64 by 64 meters. The resolution in the two directions perpendicular to the mean wind, y and z, is 1 meter, and it is 2 meters in the x direction. Because x increases in the direction of the mean wind, and because we are consistently using Taylor's frozen turbulence hypothesis, the relation between x and t can be written as $x = -Ut$.

Example 6.4.1: Gaussian process with two constraints

This 1D example relates to *one* Gaussian process subjected to two constraints. The example is identical to Example 1 in Section 3.3, except that an additional constraint has been imposed on the process. Referring to the theory derived above, we define

$$\mathbf{f}_c = \begin{pmatrix} v_c \\ v_c \end{pmatrix} , \tag{6.47}$$

and

$$\mathbf{\Phi} = \begin{pmatrix} \delta(t - t_0) \\ \delta(t - t_0 - \Delta t) \end{pmatrix} , \tag{6.48}$$

where Δt denotes the time resolution. Equation (6.40) then yields

$$\begin{aligned} \mathbf{T} &= \int\int dt'' \, dt \begin{pmatrix} \delta(t'' - t_0) \\ \delta(t'' - t_0 - \Delta t) \end{pmatrix} R(t - t'') \, (\delta(t - t_0), \delta(t - t_0 - \Delta t)) \\ &= \begin{pmatrix} R(0) & R(\Delta t) \\ R(-\Delta t) & R(0) \end{pmatrix} , \end{aligned} \tag{6.49}$$

from which we readily derive

$$\mathbf{T}^{-1}\mathbf{f} = \frac{v_c}{R(0)^2 - R(\Delta t)^2} \begin{pmatrix} R(0) - R(\Delta t) \\ -R(\Delta t) + R(0) \end{pmatrix} , \tag{6.50}$$

where it has been utilized that $R(\cdot)$ is an even function. The requested ensemble mean gust shape is thus finally obtained from equation (6.41) as

$$v_g(t'') = v_c \frac{(R(t_0 - t'') + R(t_0 + \Delta t - t'')) \, (R(0) - R(\Delta t - t''))}{R(0)^2 - R(\Delta t)^2} . \tag{6.51}$$

The present formulation represents essentially constraints on derivatives. It is clear that the procedure in this respect is an approximation, however, a good one as the time resolution can be chosen arbitrary high. An (exact) alternative way of achieving the additional constraint on the derivative of a stochastic process is described in Appendix F. However, for situations where the derivative of the stochastic process in question has a *non–linear* relationship with the turbulence components, as e.g. a wind speed direction change[2], the exact method is not

[2] A wind speed direction change, θ, can be expressed in terms of the mean wind speed, $\bar{u}$, the longitudinal turbulence component, u, and the lateral turbulence component,v, as

$$\theta = \arctan\left(\frac{v}{u + \bar{u}}\right) , \tag{6.52}$$

or alternatively

$$v = \tan(\theta) \, (u + \bar{u}) . \tag{6.53}$$

For a constraint on the wind speed direction change, θ is specified and thus known. Therefore, equation (6.53) is seen to constitute a linear relationship between the stochastic processes u and v. The derivative of the wind direction change, however, is expresses as

$$\dot{\theta} = \frac{(\bar{u} + u) \, \dot{v} - v\dot{u}}{1 + v^2} , \tag{6.54}$$

where $\dot{()}$ denotes a time derivative. Equation (6.54) is clearly highly non–linear. A linearisation of the expression with respect to u and v is not appropriate for the present purpose, as extreme events are considered to involve large turbulence components.

compatible with the present gust framework that requires constraints formulated as linear combinations of the turbulence components, c.f. equation (6.32). In these situations the presented approximation offers an attractive alternative.

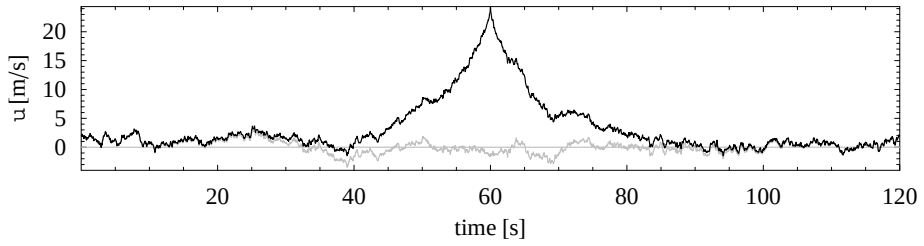

Figure 48. Same as Figure 44 but now with two conditions: $u(60\text{s}) = 20\sigma_u$ *and* $du/dt(60\text{s}) = 0$

Figure 48 shows a Gaussian simulation with the constraints $u = 20\sigma_u$ and $du/dt = 0$ imposed at $t = 60$s. The difference between Figure 44 (illustrating the situation with the constraint $u = 20\sigma_u$ only) and Figure 48 is hardly visible, indicating the fact that (for large gust amplitudes) the situation of essential excursions above the defined gust amplitude is very unlikely. Strictly speaking, to assure a maximum event, we also need to assure that the double derivative is negative at the maximum. However, for the same reason the situation of a positive second derivative is very unlikely for large gust amplitudes as also argued in (Bierbooms & Dragt 2000).

Example 6.4.2: Gust in 3D isotropic turbulence

In the example illustrated in Figure 49, $\Gamma = 0$ in the Mann model (Mann 1998), i.e. the turbulence is isotropic, and $L = 100$ m. We impose the condition that $u = 10$ m/s at $\{x, y, z\} = \{40, 20, 30\}$ m. The u-field is shown in several slices along the x– or time–axis. On the front of the box this velocity component is also shown along a horizontal line going through the gust. A similar simulation with $\Gamma = 3$ (typical anisotropy for flat terrain) shows similar gusts shapes, but the w component is generally negative in the vicinity of the gust. This is due to the negative correlation between u and w present in surface-layer turbulence.

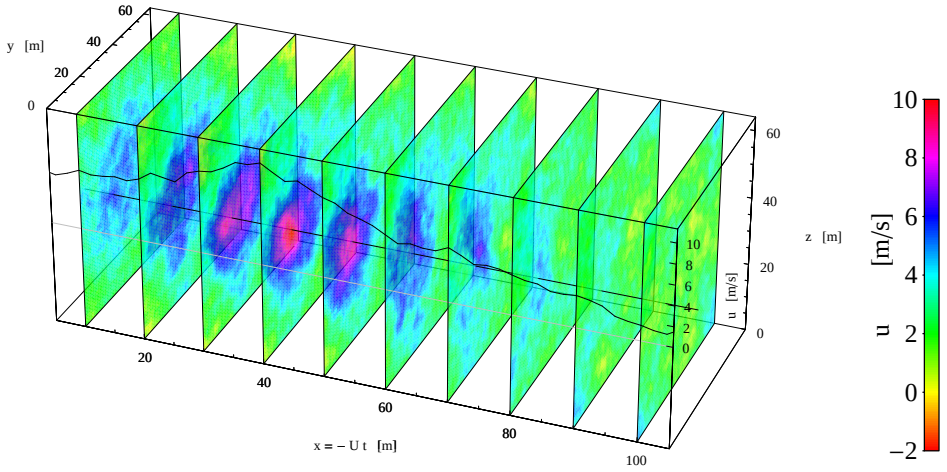

Figure 49. Three-dimensional isotropic turbulence simulation with a gust.

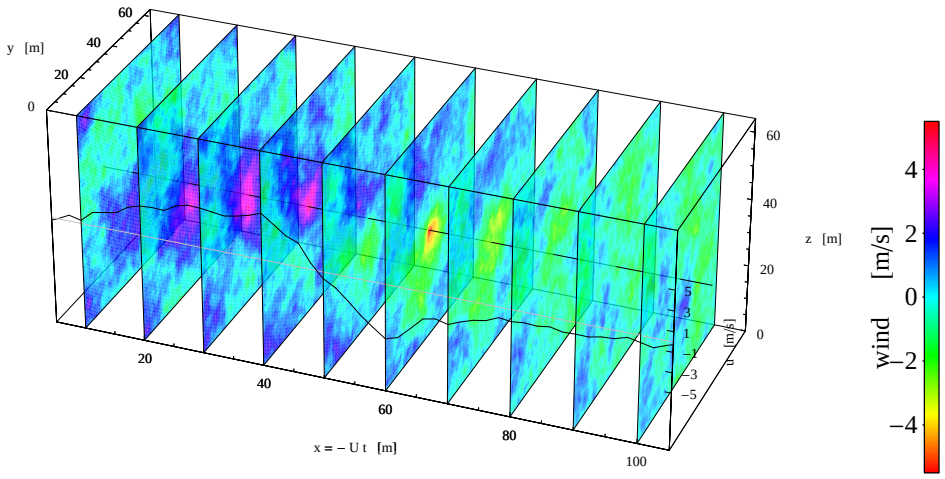

Figure 50. Anisotropic three-dimensional turbulence simulation of velocity jump. The colors shown are u given by the scale shown in Figure 51.

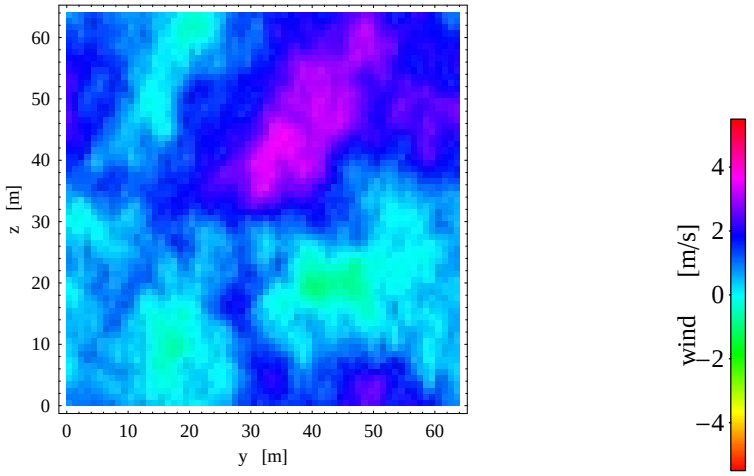

Figure 51. A vertical cut of the vertical component w of the velocity field at $x = 50$ m.

Example 6.4.3: Velocity jump in 3D anisotropic turbulence

In the example shown in Figures 50 and 51, $\Gamma = 3$ and $L = 50$ m as it is in the rest of the three-dimensional examples. Now the conditions is that the difference in u between $\mathbf{x}_1 = \{40, 32, 32\}$ m and $\mathbf{x}_2 = \{60, 32, 32\}$ m is 10 m/s. The condition is such that at the horizontal center axis of the simulation box, the u-flow converges between $x = 40$ and 60 m. Due to the incompressibility of the flow, which is reflected in $R_{ij}(\mathbf{x})$ of the Mann model, this implies that the flow must diverge in the two other components. Exactly this is seen in Figure 51 for w. It is positive above the center axis and negative below.

Example 6.4.4: Imposed change of wind direction

In the example shown in Figure 52, the double condition is that the rotor average (defined as the average on a vertical slice) of u should increase 10 m/s going from $x = 200$ to 100 m and that the rotor average of v should increase by 5 m/s; i.e. a simultaneous change of wind speed and direction. On the top of the box the vector $(U + u(x), v(x))$ along the center axis of the simulation box is shown, and

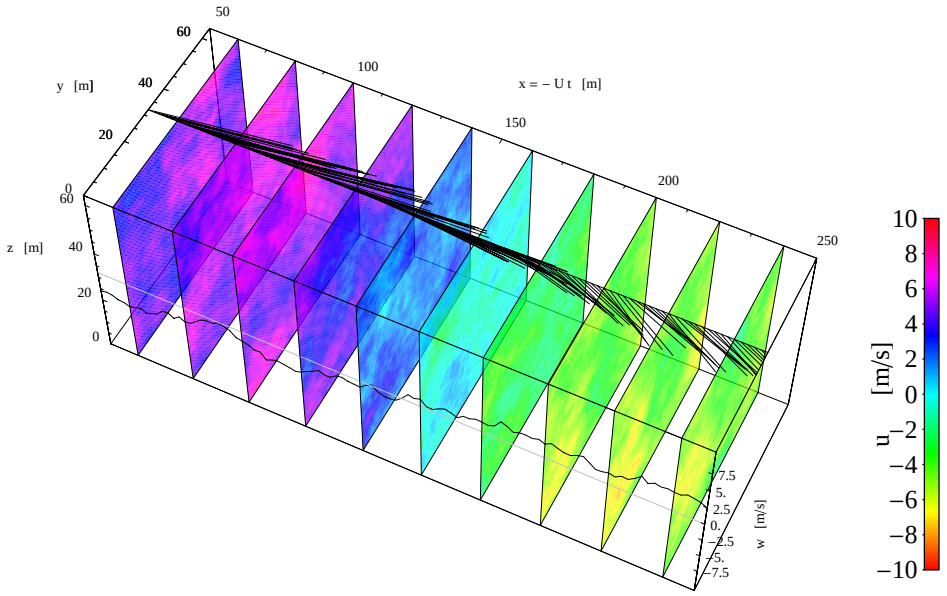

Figure 52. Turbulence with an imposed change in rotor averaged wind vector.

on the front w is displayed. It is seen that when u is strong, w is negative and *vice versa*, again culprit of the anisotropy.

Example 6.4.5: Imposed velocity shear

In the final 3D example, illustrated in Figure 53, an instantaneous "shear" is imposed at $x = 100$ m. Specifically the difference in u at 15 m directly above and below the center axis must be 10 m/s. As seen on w this implies a tendency for downward air movement to the right of the shear and upward to the left.

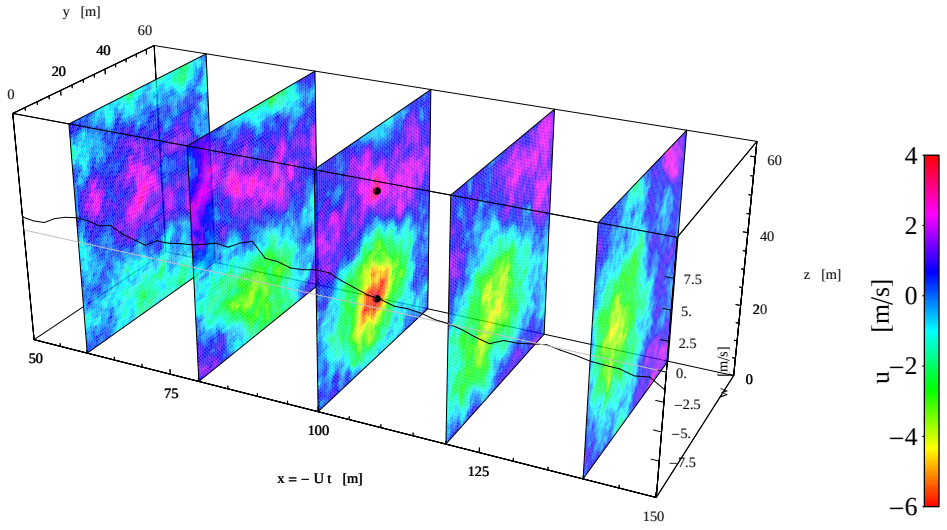

Figure 53. The difference in u at the two black point is 10 m/s.

6.5 Non-Gaussian gusts for a single process

For many atmospheric flow conditions (orography, atmospheric stability conditions, terrain roughness etc.) a Gaussian description of the turbulence components is adequate. The Gaussian assumption is equivalent with an interpretation of turbulence wind fluctuations as being the integrated effect of a large number of (un-correlated) eddy contributions, each associated with a certain frequency and spatial extend. The distribution of the turbulence components thus approximates a Gaussian distribution as a consequence of the Central Limit Theorem. However, for certain, usually complex, terrain terrain conditions, deviations from the Gaussian behavior can be observed. These deviations is usually not dramatic, however, on the other hand not so marginal that they can be neglected. They are mainly associated with large turbulence structures that couples to the terrain orography. The present section addresses constrained turbulence simulation associated with a priori defined gust events in the non–Gaussian situation.

The basic assumption is that the non–Gaussian stochastic process can be expressed as a *strictly monotone transformation* of an associated Gaussian process. Denoting the Gaussian process by $v(t)$, the non–Gaussian process by $u(t)$ and the transformation by $g(\cdot)$ we have

$$u(t) = g\left(v(t)\right) . \tag{6.55}$$

The class of non–Gaussian processes defined by the transformation (6.55) is not complete. The limitations are not related to the requirement of monotone transformation, since it is hard to imagine a sensible transformation of the above kind that is not unique. More restrictive, however, is the fact that the introduced transformation excludes "deformations" of the process time–axis. The most serious consequence is that the third order structure function of the transformed process is always identical zero (as is also true for the "mother" process), which, strictly speaking, conflicts with the characteristics of observed turbulence fields. To realize that the third order structure function is identical zero, we define the stochastic variables $v_1 = v(t)$ and $v_2 = v(t+\tau)$ with the joint Gaussian probability density function $p_v(v_1, v_2)$. Observing that the variances of v_1 and v_2 are identical, $p_v(v_1, v_2)$ is seen to be symmetric in v_1 and v_2. Therefore, the third order structure function for the Gaussian process, $S_v^3(\tau)$, defined by

$$S_v^3(\tau) = \int\int dv_1\, dv_2\, p_v(v_1, v_2)\, \left(v_1 - v_2\right)^3 , \tag{6.56}$$

is identical zero. For the transformed process, $u(t)$, the third order structure function, $S_u^3(\tau)$, is given by

$$\begin{aligned} S_u^3(\tau) &= \int\int du_1\, du_2\, p_u(u_1, u_2)\, \left(u_1 - u_2\right)^3 \\ &= \int\int du_1\, du_2\, \frac{p_v(u_1, u_2)}{g'(u_1)g'(u_2)}\, \left(u_1 - u_2\right)^3 , \end{aligned} \tag{6.57}$$

using an analogous nomenclature. As the joint probability density function of the transformed process is seen to be symmetric, it follows that the third order structure function is identical zero.

The cumulative probability functions, F_u and F_v, for the Gaussian and the defined non–Gaussian processes relate as

$$\begin{aligned} F_u(u) = P\left(u(t) \le u\right) &= P\left(g^{-1}\left(v(t)\right) \le u\right) \\ &= P\left(v(t) \le g^{-1}\left(u\right)\right) = F_v(v) . \end{aligned} \tag{6.58}$$

The relationship between the probability density functions is thus readily obtained from (6.58) as

$$f_u(u) = \frac{F_u(u)}{du} = \frac{F_v(v)}{dv}\,\frac{dv}{du} = f_v(v)\,\frac{dv}{du} = f_v(v)\,\frac{1}{g'\,(v)}\,. \tag{6.59}$$

In analogy with the assumptions adopted for the Gaussian processes we also here, without restrictions, assume that the non–Gaussian stationary process satisfy the condition

$$\left\langle g^{-1}\,(u(t))\right\rangle = 0\,. \tag{6.60}$$

The probability distribution for the non–Gaussian process $u(t)$ can be expressed in terms of the joint Gaussian distribution for the associated Gaussian process $v(t)$ and the transformation $g(\cdot)$ as

$$\begin{aligned} P_u(\{u\}) &= P_v(\{g^{-1}\,(u)\} \\ &= M\exp\left[-\frac{1}{2}\int\int dt'\,dt''\,g^{-1}\,(u(t'))\;Q(t'-t'')\,g^{-1}\,(u(t''))\right]\,, \end{aligned} \tag{6.61}$$

M being a normalization constant, and with Q even and defined according to

$$\int R(t-t')\,Q(t'-t'')\,dt' = \delta(t-t'')\,, \tag{6.62}$$

where

$$R(t-t') \equiv \left\langle g^{-1}\,(u(t))\;g^{-1}\,(u(t'))\right\rangle\,. \tag{6.63}$$

Adopting strategy and nomenclature similar to the ones applied in the previous sections, the most likely non–Gaussian process satisfying the constraint (gust event)

$$f_c = \int \phi(t')\,u_g(t')\,dt'\,, \tag{6.64}$$

is determined by introducing the Lagrange multiplier, λ, and subsequently minimizing the functional

$$\begin{aligned} \Pi = \int\int dt'\,dt''\,g^{-1}\,(u_g(t'))\;Q(t'-t'')\,g^{-1}\,(u_g(t'')) \\ -\lambda\left(\int \phi(t'')\,u_g(t'')\,dt'' - f_c\right) \end{aligned} \tag{6.65}$$

with respect to $u_g(t'')$. The variation of Π with respect to $u_g(t'')$ is denoted $\delta\Pi_{u_g}$, and the stationary values of Π is thus obtained for $\delta\Pi_{u_g} = 0$. As the transformation $g(\cdot)$ is assumed strictly monotone, the inverse transformation $g^{-1}(\cdot)$ is also strictly monotone, and the stationary values of Π are equally well obtained from

$$\delta\Pi_{g^{-1}(u_g)} = 0\,, \tag{6.66}$$

where $\delta\Pi_{g^{-1}(u_g)}$ denotes the variation of Π with respect to $g^{-1}\,(u_g(t''))$. Introducing the identity

$$u_g(t'') = g\left(g^{-1}\,(u_g(t''))\right)\,, \tag{6.67}$$

into equation (6.65), and subsequently introducing the resulting expression into equation (6.66) yields

$$\begin{aligned} \int\int dt'\,dt''\,g^{-1}\,(u_g(t'))\;Q(t'-t'')\,\delta g^{-1}\,(u_g(t'')) \\ -\lambda\int \phi(t'')\,g'\left(g^{-1}\,(u_g(t''))\right)\;\delta g^{-1}\,(u_g(t''))\;dt'' = 0\,, \end{aligned} \tag{6.68}$$

where $g'(\cdot)$ denotes the gradient of the transformation function $g(\cdot)$. Selecting the arbitrary variation $\delta g^{-1}\left(u_g(t'')\right)$ specifically as $\delta(t-t'')$, where δ in the last context denotes the Dirac function, equation (6.68) simplifies to

$$\int dt'\, g^{-1}\left(u_g(t')\right)\, Q(t'-t) = \lambda\, \phi(t)\, g'\left(g^{-1}\left(u_g(t)\right)\right)\,. \tag{6.69}$$

The equation for the requested process, $u_g(t)$, is simplified by convoluting (6.69) with the autocorrelation function R, whereby we arrive at

$$\int\int dt'\, dt\, g^{-1}\left(u_g(t')\right)\, Q(t'-t)\, R(t-t'') \\ = \lambda \int dt\, \phi(t)\, g'\left(g^{-1}\left(u_g(t)\right)\right)\, R(t-t'')\,, \tag{6.70}$$

which, by means of equation (6.62), reduces to

$$g^{-1}\left(u_g(t'')\right) = \lambda \int dt\, \phi(t)\, g'\left(g^{-1}\left(u_g(t)\right)\right)\, R(t-t'')\,. \tag{6.71}$$

Thus

$$u_g(t'') = g\left(\lambda \int dt\, \phi(t)\, g'\left(g^{-1}\left(u_g(t)\right)\right)\, R(t-t'')\right)\,. \tag{6.72}$$

Equation (6.72) is an integral equation for determination of the requested process, $u_g(t)$. Apart from the process $u_g(t)$, the equation also involve the unknown Lagrange multiplier λ. The system of equations is finally closed by adding a supplementing (implicit) equation for the Lagrange multiplier, obtained by introducing equation(6.72) into equation(6.64), whereby

$$f_c = \int dt' \phi(t')\, g\left(\lambda \int dt\, \phi(t)\, g'\left(g^{-1}\left(u_g(t)\right)\right)\, R(t-t')\right)\,. \tag{6.73}$$

Summarizing, the requested process and the introduced Lagrange multiplier are determined by the system of equations constituted by equation (6.72) and equation (6.73). For the transformation $g(\cdot)$ degenerating to the identity transformation (i.e. $v(t) = g\left(v(t)\right)$, $g'\left(\cdot\right) \equiv 1$), and expressions (6.72) and (6.73) simplifies to

$$v_g(t'') = \lambda \int dt\, \phi(t)\, R(t-t'')\,, \tag{6.74}$$

and

$$f_c = \lambda \int dt'\, \phi(t') \int dt\, \phi(t)\, R(t-t')\,, \tag{6.75}$$

respectively, which is the expressions for the Gaussian case derived separately in Section 5.3.

A general closed form solution of the system of equations (6.72) and (6.73) is not possible, and even a numerical solution is not straight forward. In the general case an iterative procedure outlined below is suggested, but it remains to be shown that the algorithm always converges. For special cases of the system of equations (6.72) and (6.73), usually associated with specific definition of the filter function $\phi(t)$, dedicated and simpler solution strategies may be appropriate (cf. the examples following the general description).

The general solution strategy consists of 3 main elements. The first element is to use the analog Gaussian gust event as a start guess for an iteration in the non–Gaussian system of equations (6.72) and (6.73). An explicit solution for the Gaussian case is obtained by solving equation (6.75) for the Lagrange multiplier λ and subsequently, using this solution, determine $v_g(t)$ from equation (6.74).

The second element is to determine the i'th iteration of the non–Gaussian gust process, $u_g^i(t)$, based on the known characteristics associated with the (i-1)'th iteration. Thus

$$u_g^i(t'') = g\left(\lambda^{i-1}\int dt\,\phi(t)\,g'\left(g^{-1}\left(u_g^{i-1}(t)\right)\right)\,R(t-t'')\right)\,. \tag{6.76}$$

The third and last element is an iterative procedure for updating the Lagrange multiplier λ. By way of introduction, we note that as the transformation function $g(\cdot)$ is assumed strictly monotone, f_c, as given by equation (6.73), is strictly monotone in λ. The gradient of f_c with respect to λ in an arbitrary expansion point is determined by

$$\frac{\partial f_c}{\partial\lambda}^{i-1} = \int dt'\phi(t')\,g'\left(\lambda^{i-1}\int dt\,\phi(t)\,g'\left(g^{-1}\left(u_g^i(t)\right)\right)\,R(t-t')\right)$$
$$\int dt\,\phi(t)\,g'\left(g^{-1}\left(u_g^i(t)\right)\right)\,R(t-t')\,, \tag{6.77}$$

and the "updated" λ value is then approximated by

$$\lambda^i = \frac{f_c - f_c^{i-1}}{\frac{\partial f_c}{\partial\lambda}^{i-1}} + \lambda^{i-1}\,, \tag{6.78}$$

where f_c^{i-1} is expressed by

$$f_c^{i-1} = \int dt'\phi(t')\,g\left(\lambda^{i-1}\int dt\,\phi(t)\,g'\left(g^{-1}\left(u_g^i(t)\right)\right)\,R(t-t')\right)\,. \tag{6.79}$$

The second and third step is repeated until satisfactory convergence is obtained.

Embedding of the derived non–Gaussian gust, $u_g(t)$, in the un–constrained non–Gaussian field, $u(t)$, is slightly more complicated than for the Gaussian situation, where the Lagrange multiplier turned out to be proportional to the value, f_c, defining the constraint (cf. equation (6.14)). The basic idea, however, is the same. The component of the requested gust, f_p, already present in the un–constrained process is determined from

$$f_p = \int \phi(t')\,u(t')\,dt'\,. \tag{6.80}$$

The analogy to the system of equations (6.72) and (6.73), but with f_c replaced by f_p, can be expressed as

$$u_p(t'') = g\left(\lambda_p\int dt\,\phi(t)\,g'\left(g^{-1}\left(u_p(t)\right)\right)\,R(t-t'')\right)\,, \tag{6.81}$$

and

$$f_p = \int dt'\phi(t')\,g\left(\lambda_p\int dt\,\phi(t)\,g'\left(g^{-1}\left(u_p(t)\right)\right)\,R(t-t')\right)\,, \tag{6.82}$$

where λ_p denotes the Lagrange multiplier associated with the gust specification f_p. Solving the system of equations constituted by equation (6.81) and equation (6.82), the resulting non–Gaussian process, $u_r(t)$, with the requested gust embedded, is given by

$$u_r(t) = u(t) - u_p(t) + u_g(t)\,. \tag{6.83}$$

Let us finally specialize the above outlined theory to two important special cases. The first example relates to an extreme gust wind speed, and the second example relates to an extreme peak–peak wind speed gust value associated with a time lag $\Delta\tau$.

Example 6.5.1: Gust in non-Gaussian turbulence

The filter function associated with the occurrence of a gust wind speed peak at time t_0 is given by

$$\phi(t) = \delta(t_0 - t)\,. \tag{6.84}$$

According to equation (6.73), the *predefined* gust amplitude relates to the filter function, the Lagrange multiplier and the requested process as

$$f_c = \int dt' \phi(t')\, g\left(\lambda \int dt\, \phi(t)\, g'\left(g^{-1}\left(u_g(t)\right)\right)\, R(t-t')\right)\,. \tag{6.85}$$

Introducing equation (6.84) into equation (6.85) we obtain

$$\begin{aligned} f_c &= \int dt'\, \delta(t_0 - t')\, g\left(\lambda \int dt\, \delta(t_0 - t)\, g'\left(g^{-1}\left(u_g(t)\right)\right)\, R(t-t')\right) \\ &= \int dt'\, \delta(t_0 - t')\, g\left(\lambda g'\left(g^{-1}\left(u_g(t_0)\right)\right)\, R(t_0 - t')\right) \\ &= g\left(\lambda\, g'\left(g^{-1}\left(u_g(t_0)\right)\right)\, R(0)\right)\,, \end{aligned} \tag{6.86}$$

from which λ can be *explicitly* determined as

$$\lambda = \frac{g^{-1}\left(f_c\right)}{R(0) g'\left(g^{-1}\left(u_g(t_0)\right)\right)}\,. \tag{6.87}$$

A closed form expression for the requested process is now easily obtained by introducing equations (6.84) and (6.87) into equation (6.71). Thus

$$\begin{aligned} g^{-1}\left(u_g(t'')\right) &= \lambda \int dt\, \delta(t_0 - t)\, g'\left(g^{-1}\left(u_g(t)\right)\right)\, R(t - t'') \\ &= \lambda\, g'\left(g^{-1}\left(u_g(t_0)\right)\right)\, R(t_0 - t'') \\ &= \frac{g^{-1}\left(f_c\right)}{R(0) g'\left(g^{-1}\left(u_g(t_0)\right)\right)}\, g'\left(g^{-1}\left(u_g(t_0)\right)\right)\, R(t_0 - t'') \\ &= \frac{g^{-1}\left(f_c\right)}{R(0)}\, R(t_0 - t'')\,, \end{aligned} \tag{6.88}$$

or

$$u_g(t'') = g\left(\frac{g^{-1}\left(f_c\right)}{R(0)}\, R(t_0 - t'')\right)\,. \tag{6.89}$$

Hence, using equation (6.83), the resulting process is given by

$$u_r(t'') = u(t) - g\left(\frac{g^{-1}\left(f_p\right)}{R(0)}\, R(t_0 - t'')\right) + g\left(\frac{g^{-1}\left(f_c\right)}{R(0)}\, R(t_0 - t'')\right)\,, \tag{6.90}$$

where f_p results from equation (6.80).

As an illustration, we let the transformation function, g, be a Winterstein transformation with the parameters: $\{0.97634107, -0.1472108, 0.02386092\}$ (c.f. Section 3.3). The correlation function is still von Kármán (6.18) as in the one-dimensional Gaussian examples. Figure 54 shows a stationary simulation. In Figure 55 the condition is $u(60\text{s}) = 5\sigma_u$.

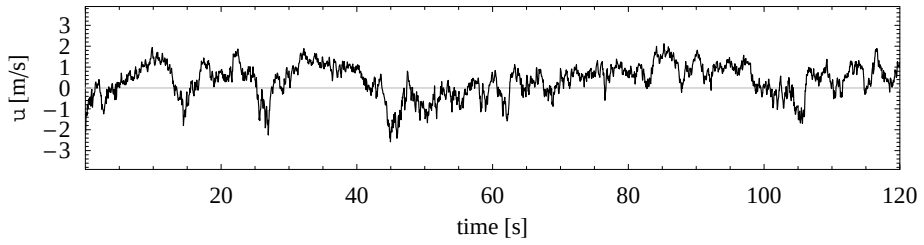

Figure 54. Stationary simulation of a non-Gaussian time series by use of the Winterstein transformation.

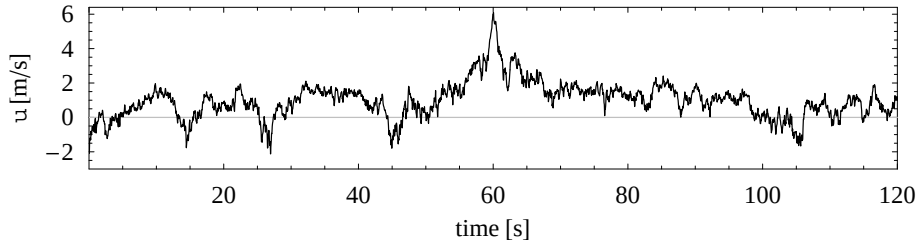

Figure 55. A gust in a non-Gaussian simulation.

Example 6.5.2: Velocity jump in non-Gaussian turbulence

The filter function associated with the peak–peak gust wind speed event, related to an arbitrary time lag $\Delta\tau$, can be expressed as

$$\phi(t) = \delta(t_0 + \Delta\tau - t) - \delta(t_0 - t)\,. \tag{6.91}$$

Introducing equation (6.91) into equation (6.73), we obtain a relation between the pre–defined peak–peak value, f_c, the Lagrange multiplier, λ, and the requested stochastic process $u_g(t)$ which, utilizing that $R(\cdot)$ is an even function, is reduced as follows

$$\begin{aligned} f_c &= \int dt' \; [\delta(t_0 + \Delta\tau - t') - \delta(t_0 - t')] \qquad (6.92)\\ &\quad g\left(\lambda \int dt \; [\delta(t_0 + \Delta\tau - t) - \delta(t_0 - t')] \; g'\left(g^{-1}\left(u_g(t)\right)\right) \; R(t - t')\right) \\ &= \int dt' \; [\delta(t_0 + \Delta\tau - t') - \delta(t_0 - t')] \\ &\quad g\left(\lambda \; \left[g'\left(g^{-1}\left(u_g(t_0 + \Delta\tau)\right)\right)\right.\right. \\ &\qquad \left.\left. R(t_0 + \Delta\tau - t') - g'\left(g^{-1}\left(u_g(t_0)\right)\right) \; R(t_0 - t')\right]\right) \\ &= g\left(\lambda \; \left[g'\left(g^{-1}\left(u_g(t_0 + \Delta\tau)\right)\right) \; R(0) - g'\left(g^{-1}\left(u_g(t_0)\right)\right) \; R(\Delta\tau)\right]\right) \\ &\quad -g\left(\lambda \; \left[g'\left(g^{-1}\left(u_g(t_0 + \Delta\tau)\right)\right) \; R(\delta\tau) - g'\left(g^{-1}\left(u_g(t_0)\right)\right) \; R(0)\right]\right)\,. \end{aligned}$$

Thus, for constraints involving more than *one* time instant, it is in general not possible to obtain an explicit expression for the Lagrange multiplier, λ, in terms of the constant defining the constraint, f_c, the requested process, $u_g(t)$ taken at the time instants involved in the definition of the constraints, and the transformation $g(\cdot)$. To overcome this, we now introduce the general expression (6.71) which, for

the constraint in question, reduces to

$$g^{-1}\left(u_g(t'')\right) = \lambda \int dt\ \left[\delta(t_0+\Delta\tau-t')-\delta(t_0-t')\right]\ g'\left(g^{-1}\left(u_g(t)\right)\right)\ R(t-t'') \\ \lambda\left[R(t_0+\Delta\tau-t'')\,g'\left(g^{-1}\left(u_g(t_0+\Delta\tau)\right)\right)-R(t_0-t'')\,g'\left(g^{-1}\left(u_g(t_0)\right)\right)\right], \tag{6.93}$$

whereby

$$u_g(t'') = g\left(\lambda\ \left[R(t_0+\Delta\tau-t'')\,g'\left(g^{-1}\left(u_g(t_0+\Delta\tau)\right)\right)\right.\right. \\ \left.\left.-R(t_0-t'')\,g'\left(g^{-1}\left(u_g(t_0)\right)\right)\right]\right). \tag{6.94}$$

The values of the requested process at time instants t_0 and $t_0+\Delta\tau$, respectively, is then easily obtained from equation (6.94) as

$$u_g(t_0) = g\left(\lambda\ \left[R(\Delta\tau)\,g'\left(g^{-1}\left(u_g(t_0+\Delta\tau)\right)\right)\right.\right. \\ \left.\left.-R(0)\,g'\left(g^{-1}\left(u_g(t_0)\right)\right)\right]\right), \tag{6.95}$$

and

$$u_g(t_0+\Delta\tau) = g\left(\lambda\ \left[R(0)\,g'\left(g^{-1}\left(u_g(t_0+\Delta\tau)\right)\right)\right.\right. \\ \left.\left.-R(\Delta\tau)\,g'\left(g^{-1}\left(u_g(t_0)\right)\right)\right]\right). \tag{6.96}$$

Introducing equations (6.95) and (6.96) in equation (6.92) we obtain the relation

$$u_g(t_0+\Delta\tau) = f_c + u_g(t_0), \tag{6.97}$$

which, of course, also could have been derived directly by introducing equation (6.91) into equation (6.64).

Summarizing, the requested process is determined from (6.94) with the three involved constants $\lambda, u_g(t_0)$ and $u_g(t_0+\Delta\tau)$ obtained by solving the system of equations (6.95), (6.96) and (6.97). Introducing equation (6.97) in equations (6.95) and (6.96) yields

$$g^{-1}\left(u_g(t_0)\right) = \lambda\ \left[R(\Delta\tau)\,g'\left(g^{-1}\left(u_g(t_0)+f_c\right)\right)\right. \\ \left.-R(0)\,g'\left(g^{-1}\left(u_g(t_0)\right)\right)\right], \tag{6.98}$$

and

$$g^{-1}\left(u_g(t_0)+f_c\right) = \lambda\ \left[R(0)\,g'\left(g^{-1}\left(u_g(t_0)+f_c\right)\right)\right. \\ \left.-R(\Delta\tau)\,g'\left(g^{-1}\left(u_g(t_0)\right)\right)\right]. \tag{6.99}$$

Isolating λ from equation (6.98), and subsequently introducing the result in equation (6.99), finally yields

$$\lambda = \frac{g^{-1}\left(u_g(t_0)\right)}{R(\Delta\tau)\,g'\left(g^{-1}\left(u_g(t_0)+f_c\right)\right)-R(0)\,g'\left(g^{-1}\left(u_g(t_0)\right)\right)}, \tag{6.100}$$

and

$$u_g(t_0) = -f_c + g\left(g^{-1}\left(u_g(t_0)\right)\right. \\ \left.\frac{R(0)\,g'\left(g^{-1}\left(u_g(t_0)+f_c\right)\right)-R(\Delta\tau)\,g'\left(g^{-1}\left(u_g(t_0)\right)\right)}{R(\Delta\tau)\,g'\left(g^{-1}\left(u_g(t_0)+f_c\right)\right)-R(0)\,g'\left(g^{-1}\left(u_g(t_0)\right)\right)}\right). \tag{6.101}$$

Equation (6.101) is an implicit equation for $u_g(t_0)$. As the requested process is defined as the most probably process fulfilling the requirements, and as only *one* process can be the most probable, the solution of equation (6.101) must be unique. The solution can (at least) be obtained in two different ways.

One method is to determine an initial solution $v_g(t_0)$ equal to the solution corresponding to the analogue Gaussian problem, and subsequently iterate in equation (6.101) until a satisfactory convergence is obtained. Another method is simply to determine $u_g(t_0)$ as the intersection between a straight line with gradient 1 and the graph defined by the points $(u_g(t_0), f\left(u_g(t_0)\right))$ with

$$f\left(u_g(t_0)\right) = -f_c + g\left(g^{-1}\left(u_g(t_0)\right)\right. \\ \left. \frac{R(0)\, g'\left(g^{-1}\left(u_g(t_0)+f_c\right)\right) - R(\Delta\tau)\, g'\left(g^{-1}\left(u_g(t_0)\right)\right)}{R(\Delta\tau)\, g'\left(g^{-1}\left(u_g(t_0)+f_c\right)\right) - R(0)\, g'\left(g^{-1}\left(u_g(t_0)\right)\right)}\right) . \quad (6.102)$$

Having determined $u_g(t_0)$, the Lagrange multiplier is determined directly from equation (6.100), and finally the requested process is obtained from equation (6.94) with (6.97) inserted

$$u_g(t'') = g\left(\lambda\, \left[R(t_0+\Delta\tau-t'')\, g'\left(g^{-1}\left(u_g(t_0)+f_c\right)\right)\right.\right. \\ \left.\left. -R(t_0-t'')\, g'\left(g^{-1}\left(u_g(t_0)\right)\right)\right]\right) . \quad (6.103)$$

The translation of the general algorithm for embedding a non–Gaussian constrained event, in a un–constrained non–Gaussian "mother process", to the present example is straight forward. From equation (6.82), combined with equations (6.100), (6.101) and (6.103), we obtain the following supplementary system of equations for determination of $u_p(t)$

$$\lambda_p = \frac{g^{-1}\left(u_p(t_0)\right)}{R(\Delta\tau)\, g'\left(g^{-1}\left(u_p(t_0)+f_p\right)\right) - R(0)\, g'\left(g^{-1}\left(u_p(t_0)\right)\right)} , \quad (6.104)$$

$$u_p(t_0) = -f_p + g\left(g^{-1}\left(u_g(t_0)\right)\right. \\ \left. \frac{R(0)\, g'\left(g^{-1}\left(u_p(t_0)+f_p\right)\right) - R(\Delta\tau)\, g'\left(g^{-1}\left(u_p(t_0)\right)\right)}{R(\Delta\tau)\, g'\left(g^{-1}\left(u_p(t_0)+f_p\right)\right) - R(0)\, g'\left(g^{-1}\left(u_p(t_0)\right)\right)}\right) , \quad (6.105)$$

and

$$u_p(t'') = g\left(\lambda_p\, \left[R(t_0+\Delta\tau-t'')\, g'\left(g^{-1}\left(u_p(t_0)+f_p\right)\right)\right.\right. \\ \left.\left. -R(t_0-t'')\, g'\left(g^{-1}\left(u_p(t_0)\right)\right)\right]\right) . \quad (6.106)$$

The resulting requested process, $u_r(t'')$ is thus finally expressed as

$$u_r(t'') = u(t'') - u_p(t'') + u_g(t'') . \quad (6.107)$$

Using the same non–Gaussian generator as applied in the previous example, Figure 56 illustrates the case where the condition is $u(75\text{s}) - u(60\text{s}) = 5\sigma_u$. It is seen that for the velocity jump there is an affinity for the negative excursion, in good agreement with the negative skewness of the process. The plots have some resemblance of wind time series of the complex site Oak Creek, where occasional strong lulls are observed.

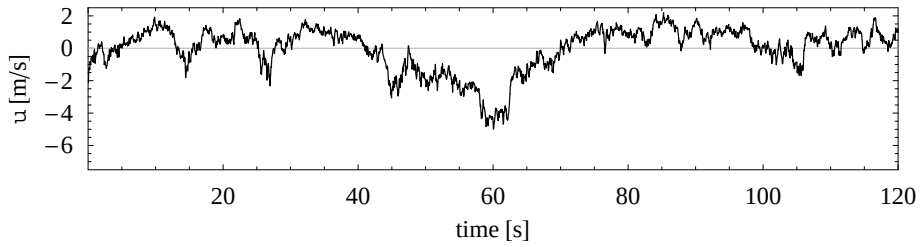

Figure 56. A velocity jump in a non-Gaussian simulation.

6.6 Non–Gaussian gusts in multiple correlated processes

The previous section outlines the theory for generation of *one* gust event in *one* non–Gaussian stationary stochastic process. In analogy with the Gaussian case, a theory for gust events in associated with N non–Gaussian stochastic processes subjected to M constraints, that might involve an arbitrary number of (time separated) gust events in each process, is developed in the present section. The formalism, however, diverts slightly from the formulation used in the Gaussian case, as a frozen turbulence formalism is adopted, meaning that the time coordinate is replaced by spatial coordinate. The non–Gaussian turbulence vector field is thus described as $\mathbf{u}^T(\mathbf{x}) = (u_1(x_1,x_2,x_3),(u_2(x_1,x_2,x_3),(u_3(x_1,x_2,x_3))$, with u_i; $i = 1,2,3$, being the 3 turbulence components and x_i; $i = 1,2,3$, the spatial coordinates. The along wind turbulence component is u_1, the transversal turbulence component is u_2, and the vertical turbulence component is u_3.

For incompressible flows mass conservation requires the divergence of the turbulence field to vanish in every point in space. Thus

$$\nabla \cdot \mathbf{u}(\mathbf{x}) = 0\,. \tag{6.108}$$

In the Gaussian case, equation (6.108) is automatically satisfied if the Mann (Mann 1994) spectral tensor is applied for the generation of a 3D field, as the wave number is forced to be perpendicular to every Fourier mode. For non–Gaussian fields, defined along the lines introduced for the single non–Gaussian process, equation (6.108) imposes limitations on the transformation from a Gaussian to a non–Gaussian process. In analogy with equation (6.55), the basic assumption for definition of the 3D non–Gaussian field, is that the three velocity components of the non–Gaussian field, $\mathbf{u}$, are related to the respective velocity components of the Gaussian field, $\mathbf{v}$, as

$$\mathbf{u}^T = (u_1,u_2,u_3) = (g_1(v_1),g_2(v_1),g_3(v_3)) \equiv \mathbf{g}(\mathbf{v})^T\,, \tag{6.109}$$

where the independent spatial coordinates have been omitted here and in the following for convenience, and g_i; $i = 1,2,3$, are *strictly monotone transformations*. The divergence theorem applied on the transformed processes implies that

$$\nabla \cdot \mathbf{g}(\mathbf{v}) = 0\,, \tag{6.110}$$

or

$$g_1'(v_1)\frac{\partial v_1}{\partial x_1} + g_2'(v_2)\frac{\partial v_2}{\partial x_2} + g_3'(v_3)\frac{\partial v_3}{\partial x_3} = 0\,. \tag{6.111}$$

Knowing the divergence theorem is satisfied for the associated Gaussian field, we have

$$\frac{\partial v_3}{\partial x_3} = -\frac{\partial v_1}{\partial x_1} - \frac{\partial v_2}{\partial x_2}\,, \tag{6.112}$$

which introduced in equation (6.111) yields

$$[g_1'(v_1) - g_3'(v_3)] \frac{\partial v_1}{\partial x_1} + [g_2'(v_2) - g_3'(v_3)] \frac{\partial v_2}{\partial x_2} = 0\,. \tag{6.113}$$

As equation (6.113) shall be satisfied identically for all possible values of $\frac{\partial v_1}{\partial x_1}$ and $\frac{\partial v_2}{\partial x_2}$, the quantities in the square brackets must vanish, implying that $g_i; i = 1, 2, 3$ must be linear transformations with identical gradients. As a linear transformation of a Gaussian field results in another Gaussian field, a different strategy must be applied unless we want to relax on the divergence condition.

We now rephrase equation (6.108) as

$$\frac{\partial u_2}{\partial x_2} = -\frac{\partial u_1}{\partial x_1} - \frac{\partial u_3}{\partial x_3}\,. \tag{6.114}$$

Based on equation (6.114), each of the turbulence components can in principle be expressed in terms of the two remaining. Selecting ("almost"[3]arbitrary) the u_2 component as the "slave" we obtain

$$u_2 = -\int_0^{x_2} dx_2 \left[\frac{\partial u_1}{\partial x_1} + \frac{\partial u_3}{\partial x_3}\right] + u_2\left(x_1, 0, x_3\right)\,. \tag{6.115}$$

To proceed, we now reformulate the 3D non–Gaussian problem in the following way: Consider initially a 2D problem defined by the two correlated, but other wise "free", turbulence components u_1 and u_3. Solve subsequently this 2D problem, and derive, by means of equation (6.115), the consistent full 3D field. The "initial conditions", $u_2\left(x_1, 0, x_3\right)$, for the integration in (6.115) is determined as $g_2(v_2(x_1, 0, x_3))$, where v_2 is obtained from the associated Gaussian 3D field. The choice of initial conditions do not affect fulfillment of the divergence theorem, but in general the condition $u_2(x_1, x_2, x_3) = g_2(v_2(x_1, x_2, x_3))$ will only be satisfied for $x_2 = 0$.

Thus, the 2D non–Gaussian stochastic field is expressed as strictly *monotone*, but otherwise free, transformations of an associated Gaussian field. We introduce the following notation: The restricted 2D Gaussian turbulence field, represented by the v_1 and the v_3 turbulence components, is denoted by $\mathbf{v}_{13}$, and the restricted 2D non–Gaussian turbulence field, represented by the u_1 and the u_3 turbulence components, is denoted by $\mathbf{u}_{13}$. The Gaussian and the non–Gaussian restricted 2D fields are thus connected by the transformations $g_1(\cdot)$ and $g_3(\cdot)$ as

$$\mathbf{u}_{13}^T = (u_1, u_3) = \left(g_1\left(v_1\right), g_3\left(v_3\right)\right) \equiv \mathbf{g}_{13}\left(\mathbf{v}_{13}\right)^T\,. \tag{6.116}$$

Without restrictions we assume that each of the involved stationary processes satisfy the condition

$$E_{x_1}\left[g_1^{-1}\left(v_1\right)\right] = E_{x_1}\left[g_1^{-1}\left(v_3\right)\right] = 0\,, \tag{6.117}$$

where x_1 denotes the along wind spatial direction, and the operator $E_{x_1}[\cdot]$ yields the average for fixed x_2, x_3 and running x_1.

Adopting the nomenclature from the section dealing with multiple Gaussian processes, it is now straight forward to extend the theory for *one* gust event in a *single* non–Gaussian process to gust events associated with N non–Gaussian stochastic processes subjected to M constraints, involving an arbitrary number of (time separated) gust events.

Introducing $\mathbf{g}_{13}^{-1}\left(\mathbf{u}_{13}\right)^T$ as $\left(g_1^{-1}\left(u_1\right), g_3^{-1}\left(u_3\right)\right)$, the probability distribution of the 2D non–Gaussian field, $\mathbf{u}_{13}$, resulting from a generator of random, stationary,

[3]For "well behaving" turbulence fields, u_1 and u_3, *referring to the same point*, are correlated, whereas u_2 is un–correlated with the two others (again for identical points). Considering different spatial points, all three turbulence components are correlated. In order to be able to specify the correlation between u_1 and u_3, u_2 has been selected as the slave.

non–Gaussian fields, is expressed in terms of the joint Gaussian distribution for the associated Gaussian (restricted) field as

$$P(\{\mathbf{u}_{13}\}) =$$
$$M \exp\left[-\frac{1}{2}\int\int d\mathbf{x}'\, d\mathbf{x}''\, \mathbf{g}_{13}^{-1}\left(\mathbf{u}_{13}\left(\mathbf{x}'\right)\right)^T\, \mathbf{Q}(\mathbf{x}'-\mathbf{x}'')\, \mathbf{g}_{13}^{-1}\left(\mathbf{u}_{13}\left(\mathbf{x}''\right)\right)\right], \quad (6.118)$$

with

$$\int \mathbf{R}(\mathbf{x}-\mathbf{x}')\, \mathbf{Q}(\mathbf{x}'-\mathbf{x}'')\, d\mathbf{x}' = \mathbf{I}\delta(\mathbf{x}-\mathbf{x}''), \quad (6.119)$$

and

$$\mathbf{R}\left(\mathbf{x}-\mathbf{x}'\right) \equiv \left\langle \mathbf{g}_{13}^{-1}\left(\mathbf{u}_{13}\left(\mathbf{x}\right)\right)\, \mathbf{g}_{13}^{-1}\left(\mathbf{u}_{13}\left(\mathbf{x}'\right)\right)^T \right\rangle . \quad (6.120)$$

Note, that $\mathbf{R}$ as well as $\mathbf{Q}$ is symmetric, and therefore

$$\int \mathbf{R}(\mathbf{x}-\mathbf{x}')\, \mathbf{Q}(\mathbf{x}'-\mathbf{x}'')\, d\mathbf{x}' = \int \mathbf{Q}(\mathbf{x}'-\mathbf{x}'')\, \mathbf{R}(\mathbf{x}-\mathbf{x}')\, d\mathbf{x}' . \quad (6.121)$$

The M selected constraints, $\mathbf{f}_c^T = (f_{c_1}, \ldots, f_{c_M})$, are now introduced in terms of the filter matrix function, $\mathbf{\Phi}(\mathbf{x})$, through the relation

$$\mathbf{f}_c = \int \mathbf{\Phi}(\mathbf{x}'')\, \mathbf{u}_{13g}(\mathbf{x}'')\, d\mathbf{x}'', \quad (6.122)$$

where $\mathbf{u}_{13g}$ denotes a stochastic field satisfying the prescribed constraints. Again, we note that the constraints defined as above are *linear* in the vector process, and that the matrix function $\mathbf{\Phi}(\mathbf{x})$ is in general not quadratic but a M×N matrix.

The most probable field, $\mathbf{u}_{13g}$, fulfilling equation (6.118) subjected to the constraints defined by equation (6.122), is determined by the variational problem

$$\int\int d\mathbf{x}'\, d\mathbf{x}''\, \mathbf{g}_{13}^{-1}\left(\mathbf{u}_{13}\left(\mathbf{x}'\right)\right)^T\, \mathbf{Q}(\mathbf{x}'-\mathbf{x}'')\, \delta\mathbf{g}_{13}^{-1}\left(\mathbf{u}_{13g}\left(\mathbf{x}''\right)\right)$$
$$- \boldsymbol{\lambda}^T \int \mathbf{\Phi}(\mathbf{x}'')\, \mathbf{G}'_{13}\left(\mathbf{g}_{13}^{-1}\left(\mathbf{u}_{13g}\left(\mathbf{x}''\right)\right)\right) \delta\mathbf{g}_{13}^{-1}\left(\mathbf{u}_{13g}\left(\mathbf{x}''\right)\right)\, d\mathbf{x}'' = 0, \quad (6.123)$$

where M Lagrange multipliers, corresponding to each of the M prescribed constraints, have been introduced and collected in the vector $\boldsymbol{\lambda}$, and the matrix $\mathbf{G}'_{13}(\cdot)$ is introduced as

$$\mathbf{G}'_{13}\left(\mathbf{g}_{13}^{-1}\left(\mathbf{u}_{13g}\left(\mathbf{x}''\right)\right)\right) = \begin{pmatrix} g_1'\left(g_1^{-1}\left(u_{1g}\right)\right) & 0 \\ 0 & g_3'\left(g_3^{-1}\left(u_{3g}\right)\right) \end{pmatrix} . \quad (6.124)$$

To achieve relation (6.123), the strictly monotone behavior of the transformation $\mathbf{g}_{13}$, and thus the inverse transformation $\mathbf{g}_{13}^{-1}$, has been utilized to replace variations with respect to $\mathbf{u}_{13}$ with variations with respect to $\mathbf{g}_{13}^{-1}(\mathbf{u}_{13})$, and further the identity

$$\mathbf{u}_{13g} = \mathbf{g}_{13}\left(\mathbf{g}_{13}^{-1}\left(\mathbf{u}_{13g}\right)\right) , \quad (6.125)$$

has been introduced.

Selecting $\delta\mathbf{g}_{13}^{-1}\left(\mathbf{u}_{13g}\left(\mathbf{x}''\right)\right)$ as $\delta(\mathbf{x}-\mathbf{x}'')\mathbf{1}$, where δ in the last context denotes the Dirac function and where $\mathbf{1} \equiv (1, \ldots, 1)$, the equations in (6.123) de-couple and reduce to

$$\int d\mathbf{x}'\, \mathbf{g}_{13}^{-1}\left(\mathbf{u}_{13}\left(\mathbf{x}'\right)\right)^T\, \mathbf{Q}(\mathbf{x}'-\mathbf{x}) = \boldsymbol{\lambda}^T\, \mathbf{\Phi}(\mathbf{x})\, \mathbf{G}'_{13}\left(\mathbf{g}_{13}^{-1}\left(\mathbf{u}_{13g}\left(\mathbf{x}\right)\right)\right) . \quad (6.126)$$

The requested field, $\mathbf{u}_{13g}(\mathbf{x})$, is then obtained by convoluting (6.126) with the correlation matrix $\mathbf{R}$. Thus

$$\int\int d\mathbf{x}\, d\mathbf{x}'\, \mathbf{g}_{13}^{-1}\left(\mathbf{u}_{13}\left(\mathbf{x}'\right)\right)^T\, \mathbf{Q}(\mathbf{x}'-\mathbf{x})\, \mathbf{R}(\mathbf{x}-\mathbf{x}'') = \boldsymbol{\lambda}^T \int d\mathbf{x}\, \boldsymbol{\Phi}(\mathbf{x})\, \mathbf{G}'_{13}\left(\mathbf{g}_{13}^{-1}\left(\mathbf{u}_{13g}\left(\mathbf{x}\right)\right)\right)\, \mathbf{R}(\mathbf{x}-\mathbf{x}'')\,. \quad (6.127)$$

By introducing equations (6.119) and (6.121) in equation (6.127), the requested non–Gaussian field is expressed as

$$\mathbf{g}_{13}^{-1}\left(\mathbf{u}_{13g}\left(\mathbf{x}'\right)\right)^T = \boldsymbol{\lambda}^T \int d\mathbf{x}\, \boldsymbol{\Phi}(\mathbf{x})\, \mathbf{G}'_{13}\left(\mathbf{g}_{13}^{-1}\left(\mathbf{u}_{13g}\left(\mathbf{x}\right)\right)\right)\, \mathbf{R}(\mathbf{x}-\mathbf{x}'')\,, \quad (6.128)$$

which is equivalent to

$$\mathbf{g}_{13}^{-1}\left(\mathbf{u}_{13g}\left(\mathbf{x}'\right)\right) = \int \mathbf{R}(\mathbf{x}-\mathbf{x}'')\, \mathbf{G}'_{13}\left(\mathbf{g}_{13}^{-1}\left(\mathbf{u}_{13g}\left(\mathbf{x}\right)\right)\right)^T\, \boldsymbol{\Phi}(\mathbf{x})^T\, d\mathbf{x}\ \boldsymbol{\lambda}\,, \quad (6.129)$$

or

$$\mathbf{u}_{13g}\left(\mathbf{x}'\right) = \mathbf{g}_{13}\left(\int \mathbf{R}(\mathbf{x}-\mathbf{x}'')\, \mathbf{G}'_{13}\left(\mathbf{g}_{13}^{-1}\left(\mathbf{u}_{13g}\left(\mathbf{x}\right)\right)\right)^T\, \boldsymbol{\Phi}(\mathbf{x})^T\, d\mathbf{x}\ \boldsymbol{\lambda}\,,\right) \quad (6.130)$$

where the symmetry of $\mathbf{R}$ has been utilized. Note, that $\boldsymbol{\Phi}$ is not symmetric and in general not even quadratic. Equation (6.130) is a system of coupled integral equations for determination of the requested non–Gaussian field $\mathbf{u}_{13}\left(\mathbf{x}'\right)$. The system of integral equations involves the yet unknown Lagrange multipliers. The system of equations is closed by adding a supplementing implicit system of equations for the Lagrange multipliers obtained by introducing equation (6.130) into equation (6.122). Thus

$$\mathbf{f}_c = \int d\mathbf{x}''\, \boldsymbol{\Phi}(\mathbf{x}') \, \mathbf{g}_{13}\left(\int \mathbf{R}(\mathbf{x}-\mathbf{x}'')\, \mathbf{G}'_{13}\left(\mathbf{g}_{13}^{-1}\left(\mathbf{u}_{13g}\left(\mathbf{x}\right)\right)\right)^T\, \boldsymbol{\Phi}(\mathbf{x})^T\, d\mathbf{x}\ \boldsymbol{\lambda}\right)\,. \quad (6.131)$$

The requested process and the introduced Lagrange multiplier are determined by the system of equations constituted by equation (6.130) and equation (6.131).

In case of un-correlated processes, $\mathbf{R}(t-t')$ as well as $\mathbf{Q}(t'-t'')$ degenerate to diagonal matrices, which obviously simplifies the (numerical) handling of the constrained simulation problem involving more processes considerably as the system of equations then decouples.

For the transformation $\mathbf{g}_{13}(\cdot)$ degenerating to the identity transformation (i.e. $u(\mathbf{x}) = \mathbf{g}_{13}\left(u(\mathbf{x})\right)$, $\mathbf{g}'_{13}\left(\cdot\right) \equiv \mathbf{1}$, expressions (6.130) and (6.131) simplifies to

$$\mathbf{u}_{13g}\left(\mathbf{x}'\right) = \int \mathbf{R}(\mathbf{x}-\mathbf{x}'')\, \mathbf{I}\, \boldsymbol{\Phi}(\mathbf{x})^T\, d\mathbf{x}\ \boldsymbol{\lambda} \quad (6.132)$$

and

$$\mathbf{f}_c = \int d\mathbf{x}''\, \boldsymbol{\Phi}(\mathbf{x}'') \int \mathbf{R}(\mathbf{x}-\mathbf{x}'')\, \mathbf{I}\, \boldsymbol{\Phi}(\mathbf{x})^T\, d\mathbf{x}\ \boldsymbol{\lambda}\,, \quad (6.133)$$

respectively, where $\mathbf{I}$ is the identity matrix. Identifying $\mathbf{u}_{13}$ with $\mathbf{v}$, the above simplified equations is seen to degenerate to the system of equations, (6.37), (6.38), describing the Gaussian multiple process case.

Having determined the ensemble mean gust shape from equations (6.130) and (6.131), it still remains to be embedded in the non–Gaussian "undisturbed" turbulence field. The procedure is analogue to the procedure applied for a single

non–Gaussian process. First the component of the specified gust event already present in the undisturbed field is quantified as

$$\mathbf{f}_p = \int \mathbf{\Phi}(\mathbf{x}'')\,\mathbf{u}_{13}(\mathbf{x}'')\,d\mathbf{x}'' \tag{6.134}$$

Subsequently, the analogy to the system of equations (6.130) and (6.131), but with $\mathbf{f}_c$ replaced by $\mathbf{f}_p$, is formulated as

$$\mathbf{u}_{13p}\left(\mathbf{x}'\right) = \mathbf{g}_{13}\left(\int \mathbf{R}(\mathbf{x}-\mathbf{x}'')\,\mathbf{G}'_{13}\left(\mathbf{g}_{13}^{-1}\left(\mathbf{u}_{13p}\left(\mathbf{x}\right)\right)\right)^T\,\mathbf{\Phi}(\mathbf{x})^T\,d\mathbf{x}\,\boldsymbol{\lambda}_p\right), \tag{6.135}$$

and

$$\mathbf{f}_p = \int d\mathbf{x}'\,\mathbf{\Phi}(\mathbf{x}')\,\mathbf{g}_{13}\left(\int \mathbf{R}(\mathbf{x}-\mathbf{x}'')\,\mathbf{G}'_{13}\left(\mathbf{g}_{13}^{-1}\left(\mathbf{u}_{13p}\left(\mathbf{x}\right)\right)\right)^T\,\mathbf{\Phi}(\mathbf{x})^T\,d\mathbf{x}\,\boldsymbol{\lambda}\right). \tag{6.136}$$

Solving the system (6.135) and (6.136), the resulting non–Gaussian field, $\mathbf{u}_{13r}$, with the prescribed gust event embedded, is finally expressed as

$$\mathbf{u}_{13r} = \mathbf{u}_{13} - \mathbf{u}_{13p} + \mathbf{u}_{13g}\,. \tag{6.137}$$

The last step in the procedure is now to supplement the simulated two–component field with the third component, using the formalism described in equation (6.115). To fulfill the divergence theorem, it is, for obvious reasons, important that the algorithm generating the third turbulence component is applied on the *resulting 2D field* with the gust events embedded.

The proposed procedure has some limitations, as the imposed gust conditions can not be defined as arbitrary linear combinations between the three turbulence components, as is the case for the Gaussian situation. The defined constraints can involve only two turbulence components in the non–Gaussian field, however, associated with arbitrary locations in the frozen turbulence box. In principle, the gust events can be defined involving arbitrary two turbulence components. It just requires that the "slave" component is selected as the turbulence component not involved in the gust definition. The system of equations for these situations are easily derived from the above described algorithm by replacing adequate lower indices.

If we, within the present formalism, insist to define gust events involving all three turbulence components, such a gust generator is easily formulated along the same lines as the present deduction involving only two turbulence components. The system of equations is easily obtained from the above derived formalism by removing the lower indices, 1 and 3, and discharging the simulation step associated with the "slave" component. The expense is that we can not assure that the divergence theorem is fulfilled which, especially for large gust events, is considered unfortunate.

7 Conclusions

- Cup anemometer data from two sites (Lammefjord and Oak Creek) were analysed in order to determine probability density functions of $v(t) = (u(t) - \bar{u})/\bar{u}$, where $u(t)$ was made from data by applying a filter. The data shows no significant dependence of $v(t)$ on $\bar{u}$ which enables pooling of the data, thereby improving estimates. For small v the pdfs are observed to be close to Gaussian, but the tails of the distributions are very different and much closer to (double sided) exponentials than Gaussians. The same trend is observed for distributions of velocity differences, where it is even more pronounced. The exponential tails seem generally to appear more clearly for variables that probe the high frequency part of the spectrum. For large values of Δv the observed $P(\Delta v)$ can be as much as a million times larger than the Gaussian prediction.

  observed non-Gaussian velocities

- Basic theory has been developed, enabling the rate of events generated by a Gaussian simulator to be determined. The investigation shows that the events may occur in cascades if the definition of the event does not involve a low pass filter of order three or higher. It is argued that exactly this type of filtering is representative for the response of a regulated wind turbine.

  cascading events in an unfiltered process

- Event rates for dimensionless wind speed and dimensionless wind speed jump, both defined from properly filtered data, were also determined from data. The results show marked deviations from the theoretical prediction based on the assumption that the wind speed is a Gaussian process. In particular very high jumps are considerably more frequent than predicted from Gaussian theory, where the discrepancy amounts to several orders of magnitude. The Gaussian theory is therefore totally inadequate for the prediction of recurrence times for rare, and potentially damaging, events.

  non-Gaussian extreme events

- The data shows that event rates for events that involve small time scales are the most non-Gaussian. At the same time these show a simple exponential behaviour which, nonetheless, enables an extrapolation to events more rare than covered by the data at hand. Furthermore, the event rates are in all cases very nearly equal to $P(v)\langle|\dot{v}|\rangle/2$. This is consistent with Rice's exact theoretical prediction if the assumption is made that v and $\dot{v}$ statistically independent. In order to make the extrapolation it therefore suffices to determine the pdf $P(v)$ and $\langle|\dot{v}|\rangle$. The same result applies to the variable Δv.

  Rice's exceedence theory works with modification

- Examples of persistent and simultaneous changes of speed and wind direction were extracted form the database www.winddata.com. These special events cannot be modelled by a stationary process.

  fronts passages

- Standard turbulence models often describe velocity fluctuations as a Gaussian process. This assumption implies that Fourier modes of a spectral representation are Gaussian and offers a simulation method based on the efficient FFT algorithm. The method may be extended in several ways, e.g. to multiple correlated time series or 3D fields of all velocity components. In either approach the target correlation between individual series of velocity components are is achieved by 'square-root' decomposition of cross-spectral matrices. This soon becomes a considerable numerical task in the case of multiple series and several computational tricks are discussed in this report.

  Fourier simulation

- A simple simulation method for non-Gaussian processes is to simulate auxiliary Gaussian time series and transform these by monotonic function designed for a match with the target probability distributions. This operation

  non-Gaussian simulation

alters spectra and correlation functions, and to compensate for this effect, the auxiliary processes are specified by distorted correlation functions, which are related to transformation functions of individual processes. The computational work of this operation is much eased when the mapping functions are expanded by Hermite polynomials. The simples version of this technique is called Winterstein's transformation, in which the transformation to non-Gaussianity is specified by a third-order polynomial designed to match the skewness and kurtosis of the target process. Also series of non-Gaussian time increments could be simulate by this method and integrated into processes, which due to the central limit theorem will be asymptotically Gaussian.

- Simulation of non-stationary processes with time-dependent probability distribution and correlation is feasible by Bezier interpolation between a set stationary simulations, produced by the same random seeds. Examples of non-stationary processes are turbulence in a front passage, turbulence near an undulating internal boundary layer, or velocities behind a wind turbine, where the unsteady wind directions tend to sweep the wake past a fixed observer. *non-stationary simulation*

- Another extension of Fourier simulation is the simulation of multiple correlated series given the measurements of a subset of these. In this way field data, e.g. from a mast at a site with unexpected turbulence features, could be used for simulation of turbulence on a rotor plane. *conditional simulation*

- A method for simulation of extreme events has been developed. This is obtained by solution of a variational problem, in which the most probable adjustment of a simulated stationary Gaussian process, subject to relevant event conditions, is found. The event conditions are formulated as linear combination of points in the realization of the process. The extreme event generator is quite versatile and will generate gusts, velocity jumps, specified averages over finite periods, extreme velocity shears, sudden changes of wind direction, or similar events. Furthermore, it is compatible with Fourier simulation. *extreme event simulation*

- The extreme event generator is generalized in various ways, i.e.: *generalization of extreme event simulation*
  1. Extreme events in multiple correlated processes. This is useful, e.g. for simulation of an extreme velocity shear and wind direction change.
  2. Extreme events with multiple conditions. An example with an extreme value where the time derivative was exactly equal to zero was presented. The extra condition did, however, not affect the simulation much.
  3. Extreme events in 3D turbulent fields. This was implemented in a quite similar to Mann's (1998) turbulence generator for anisotropic turbulence including the correlated response of all velocity components.

- The extreme event generator was generalized for non-Gaussian processes subject to relatively simple conditions, i.e. gusts and velocity jumps. An additional generalization for gusts in multiple correlated non-Gaussian processes was suggested. *extreme event in non-Gaussian processes*

- The method may be used to detect the gust shape with the largest response of a dynamic system, e.g. a turbine blade with pitch control. *the critical gust shape*

- The extreme event generator might be generalized for forecasts or other problems, in which part of the process could be considered a (complicated) condition. It is, however, not yet known whether this would be a practical approach. *possible use in forecasts problems*

- A paper on gust detection by wavelet analysis is included as an Appendix. The approach was to detect gust of a specified shape, similar to the "Extreme *wavelet analysis*

Operational Gust" in the IEC 61400-1 design code, and make extreme analysis of their recurrence rate. Wavelets might have been used for simulation, but this project preferred Fourier simulation.

Acknowledgement

The Danish Energy Agency funded the present work under the contract ENS 1363/02-0013. Further, the analysis has benefited from measurements downloaded from the internet database: "Database of Wind Characteristics" located at D-TU, Denmark, www.winddata.com. Wind field time series from the following sites has been applied: Cabauw (Royal Netherlands Meteorogical Institute, KNMI), Lammefjord, Oak Creek, Middelgrunden and Tobøl (Risø National Laboratories, Denmark), Skipheia (Norwegian University of Science and Technology, Norway), and Ainswort (National Renewable Energy Laboratory, USA)

References

Bierbooms, W., Cheng, P.-W., Larsen, G. C. & Pedersen, B. J. (2001). Modelling of Extreme Gusts for Design Calculations - Newgust, JOR3-CT98-0239 - Final Report, *IWE-011170*, Institute fir Wind Energy. Delft University of Technology, Roskilde, Denmark.

Bierbooms, W. & Dragt, J. (2000). A Probabilistic Method to Determine the Extreme Response of a Wind Turbine, *IWE-00168R*, Institute fir Wind Energy, Delft University of Technology, NL.

Davenport, A. G. (1977). The prediction of the response of structures to gusty wind, *in* I. Holland, D. Kavlie, G. Moe & R. Sigbjörnssons (eds), *Safety of Structures under Dynamic Loading*, Norwegian Institute of Technology, Trondheim, 257–284.

Deodatis, G. (1996). Non-stationary stochastic vector processes: seismic ground motion applications, *Prob. Engn. Mech.*, **11**, 149–168.

Di Paola, M. & Gullo, I. (2001). Digital simulation of multivariate wind field processes, *Prob. Engn. Mech.*, **16**, 1–10.

Ditlevsen, O., Mohr, G. & Hoffmeyer, P. (1996). Integration of non-Gaussian fields, *Prob. Engn. Mech.*, **11**, 15–23.

Dragt, J. & Bierbooms, W. (1996). Modelling of extreme gusts for design calculations, *EUWEC96, Göteborg, 20-24 May*, 842–845.

Dutton, J. A. & Højstrup, J. (1976). A model for the probability structure of atmospheric turbulence, *Conference and workshop on wind characteristics and wind energy siting, Portland, Oregon, June 19-21, 1979*, 59–69.

Gallivan, K. A., Thirumalai, S., Dooren, P. V. & Vermaut, V. (1996). High performance algorithms for Toeplitz and block Toeplitz matrices, *Linear Algebra and its Applications*, **241–243**, 343–388.

Gioffrè, M., Gusella, V. & Grigoriu, M. (2000). Simulation of non-Gaussian field applied to wind pressure fluctuations, *Prob. Engn. Mech.*, **15**, 309–389.

Grigoriu, M. (1993). On the spectral representation method in simulation, *Prob. Engn. Mech.*, **8**, 75–90.

Grigoriu, M. (1995). Parametric models of nonstationary Gaussian processes, *Prob. Engn. Mech.*, **10**, 95–102.

Grigoriu, M. (2000). Non-gaussian models for stochastic mechanics, *Prob. Engn. Mech.*, **15**, 15–23.

Gurley, K. R., Kareem, A. & Tognarelli, M. A. (1996). Simulation of a class of non-normal random processes, *Int. J. Non–Lin. Mech.*, **31**, 601–617.

Gurley, K. R., Tognarelli, M. A. & Kareem, A. (1997). Analysis and simulation tools for wind engineering, *Prob. Engn. Mech.*, **12–1**, 9–32.

IEC 61400-1 Wind Turbine Safety System: part 1, Safety Requirements (n.d.).

Johnson, G. E. (1994). Construction of particular random processes, *Proc. IEEE*, **82**, 270–285.

Kadar, A., Yaglom, A. & Zubkovskii (1989). Spatial Correlation Functions of Surface-Layer Atmospheric Turbulence in Neutral Stratification, *Boundary-Layer Meteorol.*, **47**, 233–249.

Kolmogorov, A. N. (1941). Dissipation of energy in locally isotropic turbulence, *Dokl. Akad. Nauk SSSR*. English translation in *Proc. R. Soc. Lond. A* (1991) **434**, 15–17.

Kristensen, L. & Kirkegaard, P. (1986). Sampling problems with spectral coherence, *Risø-R-526*, Risø National Laboratory.

Larsen, G. C., Bierbooms, W. & Hansen, K. S. (2004). Mean Gust Shapes, *Risø–R–1133(EN)*, Risø National Laboratory.

Larsen, G., Hansen, K. & Pedersen, B. (2002). Constrained simulation of critical wind speed gusts by means of wavelets, *Proceedings CD-ROM. 2002 global windpower conference and exhibition, Paris (FR), 2-5 Apr 2002*, European Wind Energy Association, Brussels, p. 6 p.

Lenschow, D. H., Mann, J. & Kristensen, L. (1994). How long is long enough when measuring fluxes and other turbulence statistics, *J. Atmos. Ocean. Technol.*, **11**, 661–673.

Li, Y. & Kareem, A. (1991). Simulation of multivariate nonstationary random processes by FFT, *J. Engng. Mech. ASCE*, **117**, 1037–1058.

Mann, J. (1994). The spatial structure of neutral atmospheric surface-layer turbulence, *J. Fluid Mech.*, **273**, 141–168.

Mann, J. (1998). Wind field simulation, *Prob. Engn. Mech.*, **13**, 269–282.

Nielsen, M., Chatwin, P., Jørgensen, H. E., Mole, N., Munro, R. & Ott, S. (2002). Concentration fluctuations in gas releases by industrial accidents – final report, *Risø–R–1329(EN)*, Risø national laboratory.

Nielsen, M., Hansen, K. & Pedersen, B. (2000a). Validity of the assumption of Gaussian turbulence, *Risø-R-1195(EN)*, Risø National Laboratory.

Nielsen, M., Hansen, K. S. & Pedersen, B. J. (2000b). Gyldigheden af antagelsen om Gaussisk Turbulens, *Risø–R–1195(DA)*, Risø National Laboratory.

Øye, S. (1992). *FLEX4 - Computer code for wind turbine load simulation.*

Press, W. H., Flannery, B. P., Teukolsky, S. A. & Vetterling, W. T. (1992). *Numerical Recipes in C, second edition*, Cambridge University Press.

Rice, S. O. (1944). Mathematical analysis of random noise, *Bell Systems Tech. J.*, **23**, 282.

Seong, S. H. & Peterka, J. A. (1997). Computer simulation of non-Gaussian multiple wind pressure time series, *J. Wind Eng. Ind. Aerodyn.*, **72**, 95–105.

Seong, S. H. & Peterka, J. A. (2001). Experiments on Fourier phases for synthesis of non-Gaussian spikes in turbulence time series, *J. Wind Eng. Ind. Aerodyn.*, **89**, 421–443.

Townsend, A. (1979). *The Structure of Turbulent Shear Flow, 2nd edn.*, Cambridge University Press.

van der Geest, P. A. G. (1998). An algorithm to generate samples of multivariate distributions with correlated marginals, *Comput. Statist. Data Anal.*, **27**, 271–289.

Veers, P. S. (1988). Three-dimensional Wind Simulation, *SAND88–0152*, Sandia National Laboratories.

Winkelaar, D. (1991). Fast three-dimensional wind simulation and the prediction of stochastic blade loads, *The 10^{th} ASME wind energy symposium, Houston, 20–24 January 1991.*

Winterstein, S. R. (1988). Nonlinear vibration models for extreemes and fatigue, *J. Engng. Mech. ASCE*, **114**, 1772–1790.

A Lammefjord Measurements

From www.winddata.com

Basic information

Institution	Risø National Laboratory
Address	Post box 49, DK-4000, Roskilde Denmark
Tel/fax	+45 4677 5017 / +45 4675 5619
Contacts	Michael Courtney
Links	http://www.risoe.dk/vea
Fund Agents	European Commision
Period	1987-06-01 to 1988-06-01
Classification	flat and pastoral
Country	Denmark
Position	55°47′41″N 52°11′26″E
Altitude	-3m

Mast	Height	Position
1	45m	(0,0,0)
2	30m	(-13.12,15.09,0)
3	30m	(-17.06,19.62,0)
4	10m	(-20.67,8.53,0)

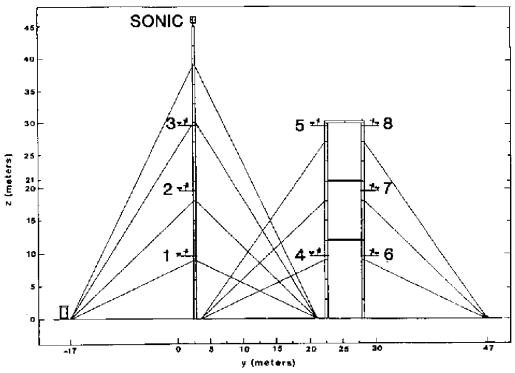

Project Description

An attempt to gather data continuously for one year with sufficient spatial and temporal resolution for wind turbine design studies. Completed with around 90% availability with a longest uninterrupted series of 103 days. The Measuring Site: The current project built upon a previous field experiment conducted to collect data for lateral coherence research (Courtney 1988). For this purpose, a site was required possessing homogeneous flow, preferably when the wind was from the prevailing south-westerly direction. A site was located at Lammefjord, a reclaimed fjord on the Danish island of Zealand. Lammefjord is amongst the flattest terrain in Denmark. Much of the land lies slightly below sea-level and because of difficulties with drainage, most of the buildings are grouped together on areas that were above water level prior to reclamation. The remainder of the land is used for agriculture, predominantly with root crops such as carrots and potatoes. To the south-east and north-west lie the towns of Faarvejle Stationby and Faarvejle respectively. To the south-east (Faarvejle Stationby) the nearest buildings are about 1 km from the measuring masts whilst in the opposite direction (Faavejle) the distance is about 0.5 km. A road connects the two towns and this passes about 150 m to the north-east of the masts. Apart from the road, the terrain to the north-east is open with the nearest buildings about 800 m away. To the south and south-west, the terrain is flat and completely unobstructed for a distance of between 2.5 and 3.0 km. Between the south-west and north-west the terrain is identical but the fetch reduces sharply to a little over 1 km. The old sea bed is bounded by

a drainage canal, beyond which the terrain rises steeply, especially between west and north-west.

Measurement System

An array of cups, vanes and one sonic anemometer were sampled by a pc. Data were stored on a magneto-optisk WORM drive. Data were recorded at 16 Hz for the sonic and 8 Hz for the cups and vanes. Measuring Masts: Since the data are primarily intended for wind turbine research, the aim was to instrument a vertical plane corresponding to that formed by the rotor of a medium sized wind turbine. This was accomplished by using three measuring masts erected so as to form a vertical plane 30 × 30m, perpendicular to the prevailing wind. An array of cup anemometers and wind direction vanes were distributed over this area as shown in the Figure. A sonic anemometer was mounted at a height of 46m. In relation to the vertical plane formed by the three masts, a 10m mast was erected 15m upstream (in the prevailing wind direction). This was instrumented with a cup anemometer and a wind vane at 10m height. The masts are referred to as masts 1-4, with the mast to the left in the Figure as number 1, the mast in the centre as 2 and that to the right as mast 3.The upstream 10m mast is mast 4. The following table gives the (x,y) coordinates of the instruments mounted on each mast (including boom offset) in a coordinate system with x in the plane of the masts pointing towards north-west (319 deg) and y pointing perpendicular to the mast plane towards the south-west (229 deg). Dimensions are in meters. Mast x y Instrumentation 1 0.0 0.0 cups(3), vanes(3), sonic, climatology 2 20.0 0.0 cups(2), vanes(2) 3 30.0 0.0 cups(3), vanes(3) 4 22.7 15.3 cup, vane ("upstream" mast) Instrument station numbers have been assigned according to the following table. Station Mast Height Instrumentation sonic 1 46 Sonic (X, Y, Z, T) 1 1 10 Cup and vane (cos, sin) 2 1 20 Cup and vane (cos, sin) 3 1 30 Cup and vane (cos, sin) 4 2 10 Cup and vane (cos, sin) 5 2 30 Cup and vane (cos, sin) 6 3 10 Cup and vane (cos, sin) 7 3 20 Cup and vane (cos, sin) 8 3 30 Cup and vane (cos, sin) 9 4 10 Cup and vane (cos, sin) 10 1 various Cup Climatological Measuring System: An independent climatological measuring system was also installed, with all the relevant sensors mounted on mast 1. This instrumentation comprised: cup anemometers at 3, 10 and 45m wind direction vane at 10m global radiation relative humidity (horse-hair hygrometer) absolute temperature at 10m difference temperature 10m - 2m difference temperature 40m - 10m barometric pressure Observations were recorded every 10 minutes using an Aanderaa battery powered data logging system. Note that with the exception of the cup anemometer speed, all recorded observations are instantaneous values once per 10 minutes. Cup mean speed is derived by counting pulses over the 10 minute period. Cup Anemometer: The cup anemometers used were the Risoe model 70, fitted with carbon fibre cups. This instrument has a length constant of 1.7m. A two-pole magnet driven by the cup shaft is used to open and close a reed-contact switch, producing two pulses per revolution. Wind speed was derived using the Risø P1225 Wind Speed Transmitter. This device is a microprocessor controlled frequency to voltage converter. The output voltage is updated on each incoming pulse such that the signal is proportional to the frequency derived from the preceding two pulses. Before installation, but following a two month "run-in" period, the cup anemometers were calibrated in a wind tunnel. Re-calibration of the cup anemometers after the completion of the experiment showed that the instrument characteristics had remained essentially constant. Individual calibrations have been used for each of the cup anemometers. Wind speed signals were sampled at 16 Hz through a first order RC filter with a -3db frequency of 35 Hz. Each two consecutive 16 Hz scans were averaged so that the data are stored at 8 Hz.

Acknowledgements

The Lammefjord measurements were partly funded by the CEC, Directorate- General for Science, Research and Development under contract number EN-3W-002-DK(B). Preparation of the CD-ROMs has been partially supported by the EU funded JOULE project "Measuring and modelling in complex terrain", contract number JOUR-0067-C(MB).

Reference

Courtney, M. (1988), An Atmospheric Turbulence Data Set for Wind Turbine Research, In: Milborrow, D.J. (Ed.), *Proceedings. 10. British Wind Energy Association Conference, London, 22-24 Mar 1988.*, Mechanical Engineering Publications Limited, London.

B Oak Creek Measurements

From www.winddata.com, by Gunner Larsen and Søren M. Petersen, 10-05-99

Basic information

project code	Oak Creek
Institution	Risø National Laboratory
Person	Gunner C. Larsen and Søren M. Petersen
email1	Gunner.Larsen@risoe.dk
email2	Soeren.M.Petersen@risoe.dk
Address	Wind Energy and Atmospheric Physics Department, Post Office Box 49, DK-4000 Roskilde, Denmark
Telephone	+45 4677 5056 and +45 4677 5043
Telefax	+45 4677 5083
Collaborators	M.S. Courtney, I. Antoniou, S.O. Lind
Funding agencies	Danish Ministry of Energy
project start	January 1th 1997
project end	December 31th 1999

Project Motivation

Verification of the structural integrity of a wind turbine involves analysis of fatigue loading as well as ultimate loading. With the trend of persistently growing turbines, the ultimate loading seems to become relatively more important. For wind turbines designed according to the wind conditions prescribed in the IEC-61400 code, the ultimate load is often identified as the leading load parameter. The objective of the Oak Creek project is to conduct a combined experimental and theoretical investigation of blade-, rotor- and tower loads caused by extreme wind load conditions occuring during normal operation as well a in stand still situations (where mean wind speeds exceeds the cut-out wind speed), with the purpose of establishing an improved description of the ultimate loading of three bladed pitch- and stall controlled wind turbines.

Measurement System

The measurements are performed in a wind farm situated at a high wind site in Oak Creek, near Tehachapi in California. The wind farm consists of wind turbines erected on a ridge in a very complex terrain. The prevailing wind direction is 320 degrees and thus perpendicular to the ridge. The turbines are closely spaced - the inter turbine spacing is 53 m, corresponding to approximately 1.2 rotor diameters. The wind turbines are tree bladed NECMicon 650 kW stall regulated turbines with hub heights and rotor diameters equal to 55 m and 44 m, respectively. The wind field is measured from two 80 m high meteorological towers erected less than one rotor diameter in front of one of the wind turbines (in the direction of the prevailing wind direction), and the distance between the two meteorological towers is 25.5 m, corresponding to 0.58 rotor diameters. Thus, detailed information of the inflow field to the particular turbine rotor is provided. The instrumentation of the meteorological towers included sensors at multiple levels. Basically, similar instruments on each of the two masts have been installed in roughly the same level relative to the terrain level. The monitoring system is running continuously, and the data are reduced and stored as 10-minutes statistics supplemented with intensive time series recordings covering periods where the mean wind speed exceeds a specified threshold (15 m/s). Consequently, there are time gaps in the time series. The monitoring sample rate is 8 and 16 Hz. Detailed information on the individual sensors is provided from the Master Sensor List. In general, all specified instrument heights are given relative to the base of the relevant meteorological tower.

Reference

S.M. Petersen, G.C. Larsen, I. Antoniou, and M.S. Courtney (1999). Experimental Investigation of Ultimate Loads. EWEC99, Nice, 1-5 March.

C Efficiency of truncated Karhuen-Loève expansion

It has been suggested to truncate the sum in equation 3.5 to include only the largest eigenvalues and thereby improve the efficiency of simulation with Karhunen-Loève expansion (Di Paola & Gullo 2001). Here, we examine whether this improvement is significant in the context of Fourier simulation with Veers' model.

- A polar grid covers the rotor plane with nodes distributed evenly on 18 azimuth angles and 10 radial stations plus a centre node, giving 181 nodes in total;
- The turbulence coherence is modelled by a simple exponential decay (Davenport 1977) $\mathrm{Coh} = \exp\left[-c\sqrt{\Delta y^2 + \Delta z^2} f \cdot u^{-1}\right]$, where $c \approx 10$ for the longitudinal wind component;
- The 181×181 coherence matrix is decomposed by Karhunen-Loève expansion for a range of frequencies f;
- Eigenvalues are sorted and the number of these needed to explain 99% of the variance is counted.

Figure 57 shows the number of eigenvalues needed to explain 99% of the variance in a Veers-type simulation with 181 nodes, as function of the dimensionless frequency

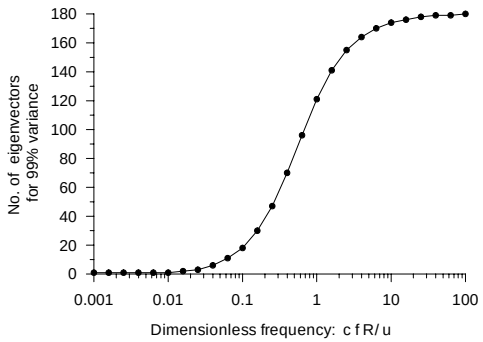

Figure 57. Evaluation of the efficient of Karhunen-Loève expansion for the present purpose.

$cRf \cdot u^{-1}$, where R is the rotor radius. The improvement is better than a factor of two for dimensionless frequencies up to 0.6.

As an example, take $R = 25$m, $c = 10$, and $u = 10$m/s with a 10-Hz simulation and 8192 samples ($\approx 14:51$ min). The basic frequency step is $\Delta f = 1.22\,10^{-3}$ Hz translating to a dimensionless frequency of 0.03 in the Figure, and the dimensionless Nykvist frequency is 250. From the figure we se that a truncated Karhunen-Loève expansion will not reduce the computational work load significantly.

D Cubic-spline and Bezier interpolation

Cubic-spline is a method for smooth interpolation between a set of N values y_j at the reference points x_j. Curvatures at the reference points y''_j are estimated by the relations

$$\frac{\Delta x_{j-1}}{6} y''_{j-1} + \frac{\Delta x_j - \Delta x_{j-1}}{3} y''_j + \frac{\Delta x_j}{6} y''_{j+1} = \frac{\Delta y_j}{\Delta x_j} - \frac{\Delta y_{j-1}}{\Delta x_{j-1}}, \quad j \in [2, N-1], \quad \text{(D.1)}$$

with $\Delta x_j = x_{j+1} - x_j$ and $\Delta y_j = y_{j+1} - y_j$. Boundary conditions for the ends must be specified, e.g. $y''_1 = y''_N = 0$. Local third-order polynomials for interpolation between the reference points are derived from the values y_j, y_{j+1}, y''_j, and y''_{j+1}, see Press et al. (1992).

The Bezier spline, sketched in figure 58, is an alternative formulation based on

$$y(t) = y_j(1-t)^3 + 3y_{j+1/3}(1-t)^2 t + 3y_{j+2/3}(1-t)t^2 + y_{j+1}t^3, \quad \text{(D.2)}$$

where $t = (x - x_j)/\Delta x \in [0, 1]$, and auxiliary Bezier control points are defined by

$$\begin{aligned} y_{j+1/3} &= y_j + y'_j \Delta x_j / 3 \quad \text{(D.3)} \\ y_{j+2/3} &= y_{j+1} - y'_{j+1} \Delta x_j / 3. \end{aligned}$$

We can reformulate a standard cubic-spline solution as a Bezier spline by estima-

tion of gradients at the reference points.

$$y'_j = \frac{\Delta y_j}{\Delta x_j} - \frac{1}{6}\Delta x_j(2y''_j + y''_{j+1}) \tag{D.4}$$

$$y'_{j+1} = \frac{\Delta y_j}{\Delta x_j} - \frac{1}{6}\Delta x_j(y''_j + 2y''_{j+1}).$$

It is noted that $y(t)$ is a linear combination of the four values y_j, $y_{j+1/3}$, $y_{j+2/3}$, and y_{j+1}.

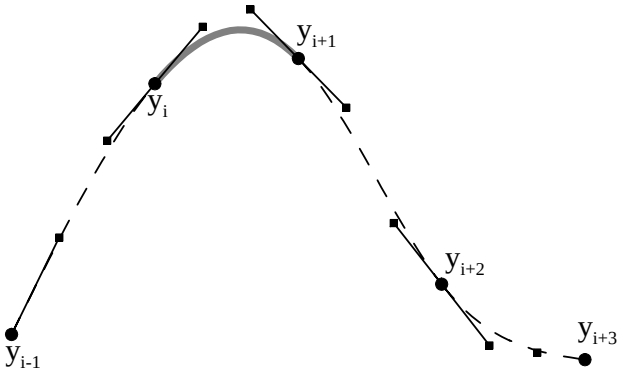

Figure 58. Bezier interpolation.

E Velocity fluctuations induced by wake meandering

Turbulence inside a wind farm is affected by upwind turbines. The large-scale ambient turbulence alters the short-term wind direction and sweep the wakes from side to side in a process, which we call wake meandering. According to this concept the velocity fluctuations emerge from three sources:

- turbulent mixing in the wake,
- the combination of wake meandering and a mean wake velocity deficit, and
- atmospheric background turbulence.

In this Appendix, we focus on meander-induced variations, and for this purpose we define a mowing frame of reference following the instantaneous wake centreline and model the mean wake velocity deficit in this system. Fixed-frame statistics are then calculated by combination of the moving-frame profile and a simple stochastic model for the centre-line movements.

Wake movements

Wake position y_c at a fixed downwind distance is assumed to have a Gaussian probability distribution

$$p\left(y_c\right) = \frac{1}{\sqrt{2\pi}\sigma_y} \exp\left[-\frac{y_c^2}{2\sigma_y^2}\right], \tag{E.1}$$

and the time variations are modelled by a Langevin process

$$\frac{dy_c\,(t)}{dt} = -\frac{y_c\,(t)}{T} + a\,(t)\ . \tag{E.2}$$

Here, T is a suitable time scale, the random accelerations $a\,(t)$ is a memory-less Gaussian process with the variance $\langle a\,(t')\,a\,(t)\rangle = \delta\,(t'-t)\cdot 2\sigma_y^2/T^2$, and zero mean giving the centre-line standard deviation σ_y. The auto-correlation of the process becomes

$$\rho = \exp\left(-\left|t-t'\right|/T\right)\ . \tag{E.3}$$

The joint probability distribution for centre-line positions at two distinct times is the two-dimensional Gaussian distribution:

$$p\,(y_c, y_c'\,|t,t'\,) = \frac{1}{2\pi\sigma_y^2\,(1-\rho^2)}\exp\left[-\frac{y_c^2(t)+y_c^2(t')-2\rho y_c(t)y_c(t')}{2\sigma_y^2\,(1-\rho^2)}\right]\ . \tag{E.4}$$

Moving-frame profile

The moving-frame cross-wind profile of the velocity deficit in a wind-turbine wake evolves from a ring shape in the near region to a bell shape in the far region. For simplicity we model this by 2D Gaussian kernels with spreading s distributed evenly on a circle with radius a. The combined momentum deficit at a position with radius r relative to the centreline is found by integration over all kernel positions, i.e. at the distance a from the centre and azimuth angle θ measured relative to the direction from centre to reference point. The squared distance between a point on the circle and the reference point is given by $a^2+r^2-2ar\cos\theta$, and thus the integral velocity deficit becomes

$$\begin{aligned}\Delta u_{\mathrm{mov}}(r) &= U_0\int_0^{2\pi}\frac{A}{2\pi s^2}\exp\left(-\frac{a^2+r^2-2ar\cos\theta}{2s^2}\right)d\theta \\ &= U_0\frac{A}{s^2}\exp\left(-\frac{a^2+r^2}{2s^2}\right)\mathrm{I}_0\left(\frac{ar}{s^2}\right),\end{aligned} \tag{E.5}$$

where $\mathrm{I}_0(x)$ is the modified Bessel function of first kind and zero order. The scaling factor A is found by a match with the wind-turbine thrust

$$\begin{aligned}\frac{1}{2}C_T\rho U_0^2\frac{\pi d^2}{4} &= 2\pi\rho\int_0^\infty r\Delta u(r)\left[U_0-\Delta u(r)\right]dr = \\ &2\pi\rho U_0^2\,A\left[1-\frac{A}{2s^2}\exp\left(-\frac{a^2}{2s^2}\right)\mathrm{I}_0\left(\frac{a^2}{2s^2}\right)\right]\end{aligned} \tag{E.6}$$

giving

$$\frac{A}{s^2} \;=\; \frac{1}{\exp\left(-\frac{a^2}{2s^2}\right)\mathrm{I}_0\left(\frac{a^2}{2s^2}\right)}\left[1-\sqrt{1-C_T\frac{d^2}{8s^2}\exp\left(-\frac{a^2}{2s^2}\right)\mathrm{I}_0\left(\frac{a^2}{2s^2}\right)}\right], \tag{E.7}$$

and so the moving-frame velocity deficit becomes

$$\begin{aligned}&\frac{\Delta u_{\mathrm{mov}}(r)}{U_0} = \\ &\left[1-\sqrt{1-C_T\frac{d^2}{8s^2}\exp\left(-\frac{a^2}{2s^2}\right)\mathrm{I}_0\left(\frac{a^2}{2s^2}\right)}\right]\cdot\frac{\exp\left(-\frac{r^2}{2s^2}\right)\mathrm{I}_0\left(\frac{ar}{s^2}\right)}{\mathrm{I}_0\left(\frac{a^2}{2s^2}\right)}.\end{aligned} \tag{E.8}$$

Fixed-frame profile

The fixed-frame profile is found by convolution of the moving-frame profile and the probability distribution of possible centre-line positions. The vertical velocity fluctuations are smaller and have less spatial correlation than the horizontal fluctuations, so we assume that centre-line movements are essentially horizontal with a normal probability distribution with spreading σ_y. By substitution of equation E.8 we find

$$\begin{aligned}\Delta u_{\mathrm{fix}}(y,z) &= \int \Delta u_{\mathrm{mov}}(y-y_c,z)p(y_c)d\,y_c \\ &= U_0 B\left(C_T,\frac{a}{s},\frac{d}{s}\right)\int_{-\infty}^{\infty}\exp\left(-\frac{(y-y_c)^2+z^2}{2s^2}\right)\mathrm{I}_0\left(\frac{a\sqrt{(y-y_c)^2+z^2}}{s^2}\right) \\ &\qquad\cdot\frac{1}{\sqrt{2\pi}\sigma}\exp\left(-\frac{y_c^2}{2\sigma^2}\right)dy_c \quad \text{(E.9)}\end{aligned}$$

This integral is not standard, and numerical computation by Fourier transformation is probably the most efficient method. An analytic form is, however, possible by expansion of the Bessel function

$$\mathrm{I}_0(x)=\sum_{n=0}^{\infty}\frac{x^{2n}}{(2n!!)^2}, \quad \text{(E.10)}$$

where $n!! = n(n-2)(n-4)\ldots$ denotes the double factorial. For convenience of notation we normalize all distances by s, e.g. $\tilde{r}=r/s$. Insertion of this series lead to

$$\begin{aligned}\frac{\Delta u_{\mathrm{fix}}(\tilde{y},\tilde{z})}{U_0} &= \frac{B\left(C_T,\tilde{a},\tilde{d}\right)}{\sqrt{2\pi}\tilde{\sigma}}\exp\left(-\frac{\tilde{z}^2}{2}\right) \\ &\quad\cdot\sum_{n=0}^{\infty}\frac{\tilde{a}^{2n}}{(2n!!)^2}\int_{-\infty}^{\infty}\exp\left(-\frac{(\tilde{y}-\tilde{y}_c)^2}{2}-\frac{\tilde{y}_c^2}{2\tilde{\sigma}_y^2}\right)\left((\tilde{y}-\tilde{y}_c)^2+\tilde{z}^2\right)^n d\tilde{y}_c, \quad \text{(E.11)}\end{aligned}$$

which involves simpler integrals of the following type

$$\begin{aligned}\int_{-\infty}^{\infty}\tilde{y}_c^p\exp\left(-\frac{(\tilde{y}-\tilde{y}_c)^2}{2}-\frac{\tilde{y}_c^2}{2\tilde{\sigma}_y^2}\right)d\tilde{y}_c = \\ \sqrt{2\pi}\exp\left(-\frac{\tilde{y}^2}{2(1+\tilde{\sigma}_y^2)}\right)\left(\frac{\tilde{\sigma}_y^2}{1+\tilde{\sigma}_y^2}\right)^{\frac{p+1}{2}}F_p\left(\frac{\tilde{y}\tilde{\sigma}_y}{\sqrt{1+\tilde{\sigma}_y^2}}\right), \quad \text{(E.12)}\end{aligned}$$

where the last term is a polynomial of the form

$$\begin{aligned} F_0(x)&=1 & F_4(x)&=x^4+6x^2+3 \\ F_1(x)&=x & F_5(x)&=x^5+10x^3+15x \\ F_2(x)&=x^2+1 & F_6(x)&=x^6+15x^4+45x^2+15 \\ F_3(x)&=x^3+3x & F_{n+1}(x)&=xF_n(x)+nF_{n-1}(x). \end{aligned} \quad \text{(E.13)}$$

The power of the relative position is expanded by the multinomial formula

$$\left[(y-y_c)^2+z^2\right]^n=\sum_{i=0}^{n}\sum_{j=0}^{n-i}\frac{n!}{(n-i-j)!i!j!}(y^2+z^2)^{n-i-j}(-2y)^i y_c^{2j+i}, \quad \text{(E.14)}$$

and finally we obtain an expression for the fixed-frame profile of the velocity deficit.

$$\frac{\Delta u_{\text{fix}}(y,z)}{U_0} = \frac{B\left(C_T,\tilde{a},\tilde{d}\right)}{\tilde{\sigma}_y}\exp\left(-\frac{\tilde{y}^2}{2(1+\tilde{\sigma}_y^2)}-\frac{\tilde{z}^2}{2}\right)$$
$$\cdot\sum_{n=0}^{\infty}\sum_{i=0}^{n}\sum_{j=0}^{n-i}\frac{\tilde{a}^{2n}}{(2n!!)^2}\frac{n!}{(n-i-j)!i!j!}(\tilde{y}^2+\tilde{z}^2)^{n-i-j}(-2\tilde{y})^i$$
$$\cdot F_{2j+i}\left(\frac{\tilde{y}\tilde{\sigma}_y}{\sqrt{1+\tilde{\sigma}_y^2}}\right)\left(\frac{\tilde{\sigma}_y}{\sqrt{1+\tilde{\sigma}_y^2}}\right)^{2j+i+1}. \quad \text{(E.15)}$$

The profile shapes in the bottom row of in Figure 59 are calculated by equation E.8 and show the moving-frame wake profile for variable spreading of the gaussian kernels. The plots above are calculated by a truncated version of equation E.15, i.e. $n = 0 \ldots 4$, for variable degree of meander intensity. Wake meandering is seen to smear out the profile in the y-direction.

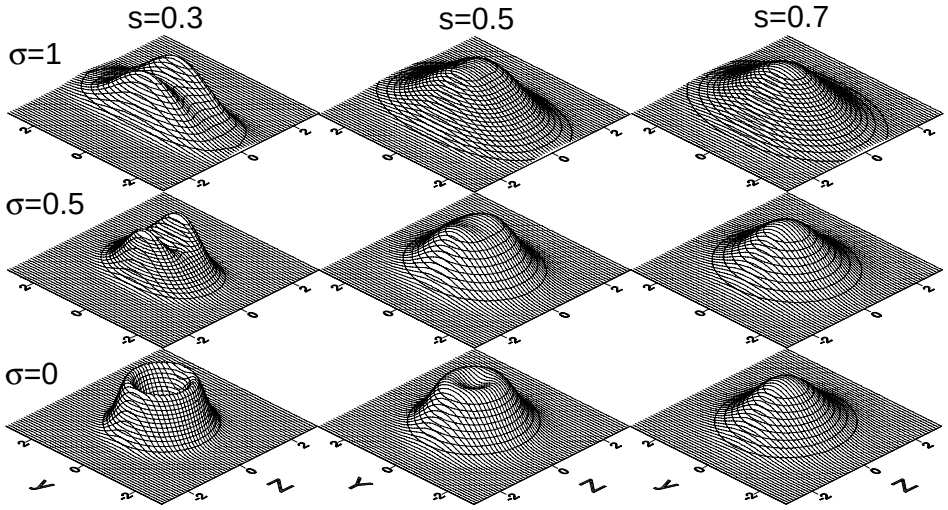

Figure 59. Fixed-frame profiles of wake velocity deficit shown for variable spreading of the gaussian kernel (columns) and variable meander intensities (rows).

Gaussian moving-frame profile

To study the meander-induced velocity fluctuations we consider a gaussian moving-frame profile with the maximum velocity deficit A and the wake dimension is σ_w.

$$\Delta u_{\text{mov}}(y,y_c) = A\exp\left[-\frac{(y-y_c)^2}{2\sigma_w^2}\right] \quad \text{(E.16)}$$

This model is computationally more convenient than the above expressions and expected to match the real profile in the far field. The fixed frame average profile is

$$\Delta u_{\text{fix}}(y) = \int \Delta u_{\text{mov}}(y,y_c)p\left(y_c\right)\,dy_c = \frac{A}{\sqrt{1+M^2}}\exp\left[-\frac{\Delta^2}{2(1+M^2)}\right], \quad \text{(E.17)}$$

where $M = \sigma_y/\sigma_w$ is the dimensionless meander intensity, and $\Delta = y/\sigma_w$ is a dimensionless position measured relative to the average centre-line position.

Fixed-frame cross statistics of fluctuations with spatial and temporal separation is found by the joint probability distribution

$$\langle \Delta u(y_1,t_1)\Delta u(y_2,t_2)\rangle = \iint \Delta u_w(y_1,y_{c,1})\Delta u_w(y_2,y_{c,2}) \\ p\,(y_{c,1},y_{c,2}\,|t_1,t_2\,)\;dy_{c,1}dy_{c,2}, \quad \text{(E.18)}$$

where $y_{c,1}$ and $y_{c,2}$ is short-hand notation for time-dependent wake-positions $y_c(t_1)$ and $y_c(t_2)$. Evaluating this double integral and subtracting the long-term average we obtain the time-lagged covariance function

$$R_{ij}(\tau) = A^2 \left\{ \frac{\exp\left[-\frac{(1+M^2)(\Delta_i^2+\Delta_j^2)-2\rho(\tau)M^2\Delta_i\Delta_j}{2[(1+M^2)^2-\rho^2(\tau)M^4]}\right]}{\sqrt{(1+M^2)^2-\rho^2(\tau)M^4}} - \frac{\exp\left[-\frac{\Delta_i^2+\Delta_j^2}{2(1+M^2)}\right]}{1+M^2} \right\}, \quad \text{(E.19)}$$

where $\Delta_i = y_i/\sigma_w$ and $\Delta_j = y_j/\sigma_w$. The meander-induced variance is found by insertion of $i=j$ and $\rho=1$

$$\sigma^2_{u,\mathrm{fix}} = A^2 \left[\frac{\exp\left[-\frac{\Delta^2}{1+2M^2}\right]}{\sqrt{1+2M^2}} - \frac{\exp\left[-\frac{\Delta^2}{1+M^2}\right]}{1+M^2} \right]. \quad \text{(E.20)}$$

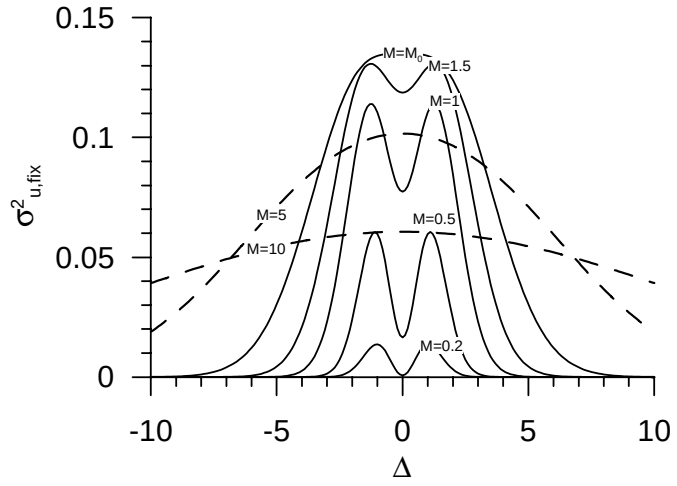

Figure 60. Fixed-frame variance as a function of position shown for a range of meander intensities.

This function is shown in Figure 60 for a range of meander intensities. The maximum is

$$\max\left(\sigma^2_{u,\mathrm{fix}}\right) = \begin{cases} \dfrac{A^2\,M^2\left(1+M^2\right)^{2\left(1+M^{-2}\right)}}{\left(1+2\,M^2\right)^{3/2\left(2+M^{-2}\right)}} & \text{at } \Delta=\Delta_{\max} \quad \text{for } M \le M_0 \\ A^2\left[\frac{1}{\sqrt{1+2\,M^2}} - \frac{1}{1+M^2}\right] & \text{at } \Delta = 0 \qquad \text{for } M > M_0, \end{cases} \quad \text{(E.21)}$$

as shown in Figure 61. For small meander movements the maximum is observed near the steepest gradients of the moving-frame profile, but for larger meander movements it gradually changes position

$$\Delta_{\max}(M) = \frac{\sqrt{1+3\,M^2+2\,M^4}}{M}\left[\ln\left(\frac{\left(1+2\,M^2\right)^{3/2}}{\left(1+M^2\right)^2}\right)\right]^{1/2} \quad \text{(E.22)}$$

until it reaches the centreline for a meander intensity given by

$$M_0^6 - 4M_0^4 - 6M_0^2 = 2 \Rightarrow M_0 \simeq 2.285 \quad \text{(E.23)}$$

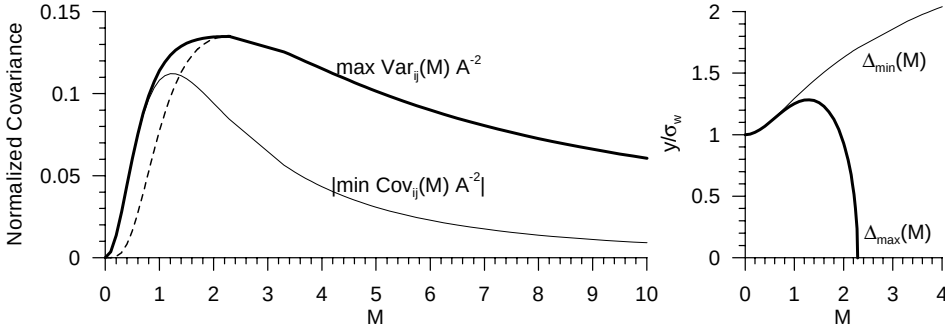

Figure 61. Maximum variance (fat line) and minimum covariance (thin line) as a function of meander intensity. Also shown are the centre-line variance (dashed line) and the positions of these extremes.

The covariance is found by insertion of $\rho(0) = 1$ in equation E.19 leading to the function

$$\mathrm{Cov}_{ij} = A^2 \left\{ \frac{\exp\left[-\frac{\Delta_i^2+\Delta_j^2+(\Delta_i-\Delta_j)^2M^2}{2(1+2M^2)}\right]}{\sqrt{1+2M^2}} - \frac{\exp\left[-\frac{\Delta_i^2+\Delta_j^2}{2(1+M^2)}\right]}{1+M^2} \right\} \tag{E.24}$$

which is shown in Figure 62 for three meander intensities. The minimum covariance

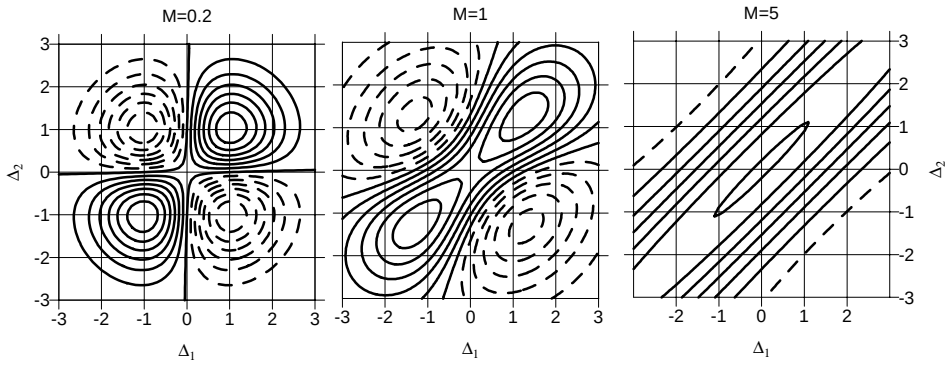

Figure 62. Contours of the covariance function Cov_{ij} *normalized by its maximum value at three different meander intensities. Dashed lines indicates negative covariance.*

$$\min\left(\mathrm{Cov}_{ij}\right) = -\frac{M^2(1+2\,M^2)^{1/(2M^2)}}{(1+M^2)^{2(1+M^{-2})}} \tag{E.25}$$

is found at $\pm\Delta_i = \mp\Delta_j = \Delta_{\min}$ where

$$\Delta_{\min} = \frac{\sqrt{1+M^2}}{M}\left[\ln\left(\frac{\left(1+M^2\right)^2}{\left(1+2\,M^2\right)^{1/2}}\right)\right]^{1/2} \tag{E.26}$$

This distance, and the value of the minimum covariance, are shown by thin curves in Figure 61. In a wind farm, the wake dimension and rotor radius are fairly similar and the relevant separations are limited, say $|\Delta_i - \Delta_j| \lesssim 2$. Therefore we are mostly interested in the covariance near the bottom-left to top-right diagonals in Figure 62.

Bimodal moving-frame profile

Real wakes have an initially bimodal shape reflecting the radial dependence of the rotor thrust. To investigate this effect, we study an approximate profile composed of two Gaussian shapes.

$$\Delta u_{\mathrm{mov}}(y, y_c) = A' \left\{ \exp\left[-\frac{(y - y_c - d)^2}{2(\sigma_w^2 - d^2)} \right] + \exp\left[-\frac{(y - y_c + d)^2}{2(\sigma_w^2 - d^2)} \right] \right\} \quad \text{(E.27)}$$

To facilitate comparison with the Gaussian profile, this bimodal profile is designed to match the second spatial moment of the wake profile σ_w^2. The peak positions must be inside the wake dimension $d < \sigma_w$ and the profile will only be bimodal when $d > \sigma_w/\sqrt{2}$. The amplitude is chosen for a match of the momentum deficits of 2D cross-sections

$$A\, 2\pi \int_0^\infty r\, \exp\left[-\frac{r^2}{2\sigma_w^2} \right] dr \quad = \quad A'\, 2\pi \int_0^\infty r\, \exp\left[-\frac{(r-d)^2}{2(\sigma_w^2 - d^2)} \right] dr \quad \text{(E.28)}$$

giving

$$A' \quad = \quad \frac{1 + \alpha^2}{\exp\left(-\alpha^2/2\right) + \alpha\sqrt{2\pi}\, \mathrm{erf}(\alpha/\sqrt{2})} A, \quad \text{(E.29)}$$

where we define $\alpha = d/(\sigma_w^2 - d^2)^{1/2}$. Examples are shown in the left-hand panel of Figure 63.

$$\Delta u_{\mathrm{fix}} = \frac{A'}{\sqrt{1+m^2}} \left\{ \exp\left[-\frac{(\delta - \alpha)^2}{2(1+m^2)} \right] + \exp\left[-\frac{(\delta + \alpha)^2}{2(1+m^2)} \right] \right\} \quad \text{(E.30)}$$

The time-lagged covariance function becomes

$$R_{ij}(\tau) = A'^2 \left\{ \sum_{k,l=\pm 1} \frac{\exp\left[-\frac{(1+m^2)(\delta_i^2+\delta_j^2) - 2\rho(\tau) m^2 \delta_i \delta_j + 2\alpha(\alpha + k\delta_i + l\delta_j)(1 - kl\, m^2 \rho(\tau))}{2[(1+m^2)^2 - \rho^2(\tau) m^4)]} \right]}{\sqrt{((1+m^2)^2 - \rho^2(\tau) m^4}} \right.$$

$$\left. - \sum_{k,l=\pm 1} \frac{\exp\left[-\frac{(1+m^2)(\delta_i^2+\delta_j^2) + 2\alpha(\alpha + k\delta_i + l\delta_j)}{2(1+m^2)^2} \right]}{1+m^2} \right\}, \quad \text{(E.31)}$$

where each sum contain four terms, and where we define $\alpha = d\,(\sigma_w^2 - d^2)^{-1/2}$, $\delta_1 = \sqrt{1+\alpha^2}\Delta_1$, $\delta_2 = \sqrt{1+\alpha^2}\Delta_2$, and $m = \sqrt{1+\alpha^2}M$. The variance is found as above

$$\sigma_{u,\mathrm{fix}}^2 = A'^2 \left\{ \sum_{k,l=\pm 1} \frac{\exp\left[-\frac{\delta^2 + (1 + (1-kl)m^2)(\delta(k+l)+\alpha)\alpha}{1+2m^2} \right]}{\sqrt{1+2m^2}} \right.$$

$$\left. - \sum_{k,l=\pm 1} \frac{\exp\left[-\frac{\Delta^2 + (\delta(k+l)+\alpha)\alpha}{1+m^2} \right]}{1+m^2} \right\} \quad \text{(E.32)}$$

and shown in the right-hand panel of Figure 63. For moderate meander intensity these profiles are more complex than with the simpler moving-frame profile in Figure 60, whereas differences are small for high meander intensity. The covariance function is found by insertion of $\rho(0) = 1$, leading to

$$\mathrm{Cov}_{ij} = A'^2 \left\{ \sum_{k,l=\pm 1} \frac{\exp\left[-\frac{\delta_i^2 + \delta_j^2 + (\delta_i - \delta_j)^2 m^2 + 2\alpha(\alpha + k\delta_i + l\delta_j)(1 + (1-kl)m^2)}{2(1+2m^2)} \right]}{\sqrt{1+2m^2}} \right.$$

$$\left. - \sum_{k,l=\pm 1} \frac{\exp\left[-\frac{\delta_i^2 + \delta_j^2 + (\delta_i - \delta_j)^2 m^2 + 2\alpha(\alpha + k\delta_i + l\delta_j)}{2(1+m^2)^2} \right]}{1+m^2} \right\} \quad \text{(E.33)}$$

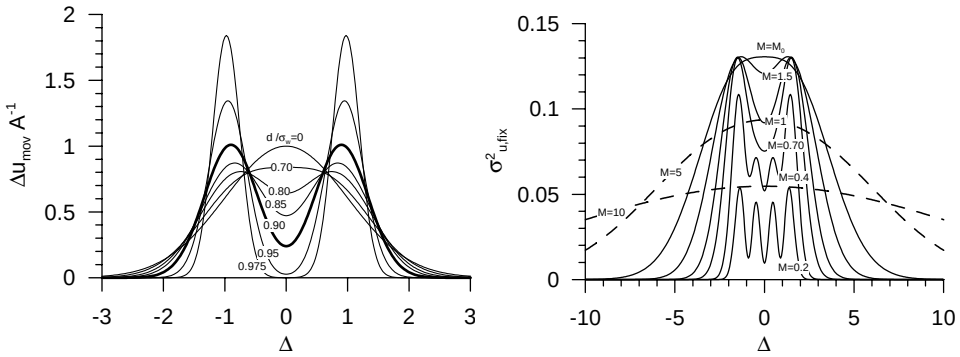

Figure 63. Bi-modal moving-frame profiles (left) and resulting fixed-frame variance (right) as a function of position for $d = 0.9\sigma_w$ and a range of meander intensities.

This function is shown in Figure 64. By comparison with Figure 62 we see that for modest meander intensity, both the time scale of the auto-correlation and the length scale of cross-correlation are shorter with the bimodal profile.

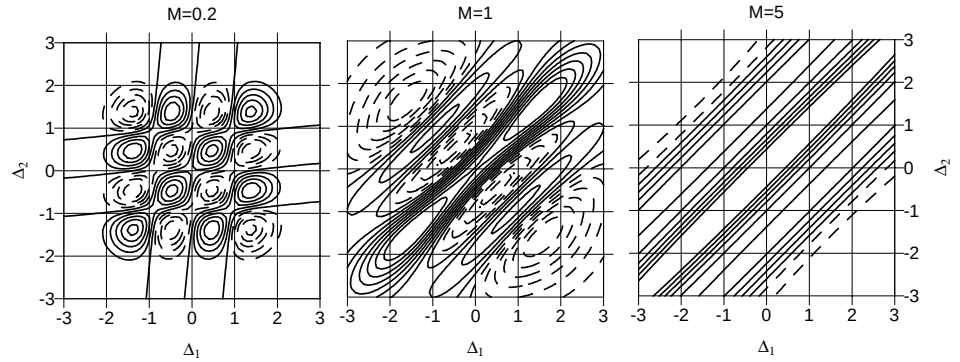

Figure 64. Contours of the covariance function Cov_{ij} *with a bi-modal moving-frame profile normalized by its maximum value at three different meander factors. Dashed lines indicates negative covariance.*

F Constrains involving derivatives of a stochastic process

The formalism derived in Chapter 6 is also capable to deal with constraints formulated in the derivatives of the stochastic processes. The derivatives can be of arbitrary order. Using partial integration, the basic recognition is the following

$$\int dt\, \delta'(t-t_0)\, v(t) = [\delta(t-t_0)v(t)]_{-\infty}^{\infty} - \int dt\, \delta(t-t_0)\, v'(t) = -v'(t_0)\,, \quad \text{(F.1)}$$

where a prime denotes differentiation, and $\delta(\cdot)$ is the Dirac function. By induction, it is seen that

$$\int dt\, \delta^{(n)}(t-t_0)\, v(t) = (-1)^n v^{(n)}(t_0)\,. \quad \text{(F.2)}$$

Let us now return to the single Gaussian process subjected to two constraints – prescribed wind speed and zero wind gradient – as formulated in Example 1 in

Section 4.3. Referring to the notation in the derived theory, the two constraints are defined by

$$\mathbf{f}_c = \begin{pmatrix} v_c \\ 0 \end{pmatrix}, \tag{F.3}$$

and

$$\mathbf{\Phi}_s = \begin{pmatrix} \delta(t) \\ \delta'(t) \end{pmatrix}, \tag{F.4}$$

where we for simplicity have assumed the constraints imposed at time $t = 0$. Equation (6.40) then yields

$$\begin{aligned} \mathbf{T} &= \int\int dt''\, dt \begin{pmatrix} \delta(t) \\ \delta'(t) \end{pmatrix} R(t-t'') \, (\delta(t''), \delta'(t'')) \\ &= \begin{pmatrix} R(0) & -R'(0) \\ -R'(0) & R''(0) \end{pmatrix}, \end{aligned} \tag{F.5}$$

from which we readily derive

$$\mathbf{T}^{-1}\mathbf{f}_c = \frac{v_c}{R(0)R''(0) - R'(0)^2} \begin{pmatrix} R''(0) \\ R'(0) \end{pmatrix}. \tag{F.6}$$

The requested ensemble mean gust shape is thus finally obtained from equation (6.41) as

$$v_g(t'') = \frac{v_c R(t'')R''(0)}{R(0)R''(0)}, \tag{F.7}$$

where it symmetry of $R(\cdot)$ has been utilized, meaning that $R(t'') = R(-t'')$ and that $R'(0) = 0$. Replacing t'' with $t - t_0$ we finally arrive at

$$v_g(t - t_0) = \frac{v_c R(t - t_0)}{R(0)}. \tag{F.8}$$

The resulting stochastic process is now obtained directly from equation (6.42) as

$$v_r(t) = v(t) + (v_c - v(t_0)) \frac{R(t - t_0)}{R(0)} + \frac{v'(t_0)}{R''(0)} R'(t - t_0), \tag{F.9}$$

where $v(t)$ denotes the un–constrained Gaussian process. Expression (F.9) is exactly equal to the expression for the same gust situation derived in (Bierbooms & Dragt 2000) although using a different approach.

G Constrained simulation of critical wind speed gusts by means of wavelets

Presented at the 2002 Global Windpower Conference and Exhibition 2 - 5 April 2002 - CNIT, La Défense, Paris, France
by Gunner Chr. Larsen, Kurt S. Hansen and Bo Juul Pedersen

Abstract

For most structures exposed to wind loading, extreme response is associated with extreme wind speeds. However for wind turbines - especially for pitch regulated wind turbines - the design driving thrust loading is often associated with severe wind gust situations occurring during normal operation and these are thus related to the mean wind speed regime [5m/s; 25m/s]. Based on knowledge on the load response characteristic of the wind turbine (in terms of aerodynamics and pitch action) it is possible to identify a general critical mean gust shape that may potentially result in ultimate thrust loading. In the IEC 61400-1 design code, this particular load case is defined as Extreme Operational Gust (EOG). This (coherent deterministic) gust has a characteristic "Mexican hat" shape with prescribed time extend and magnitude. The time constant depends on the return period of the extreme wind speed gusts, whereas the magnitude depends on the return period as well as the mean wind speed. The present paper presents a rational method to calibrate the wind speed gust magnitudes specified in the IEC 61400-1 code. The method combines a wavelet expansion with extreme statistics and results in consistent estimates of wind speed gust magnitudes for arbitrary return period, mean wind speed and gust time scale. In addition the method offers to embed the resulting extreme wind gust consistently in a (coherent) stochastic wind field. Based on measured data, extracted from "Database on Wind Characteristics" (http://www.winddata.com/), the method has been applied to estimate the magnitudes of wind speed gusts with similar shape, time extend and return period as the gusts specified in the IEC 61400-1 code.

Keywords: Extreme Statistics, Extreme Wind Conditions, Gust Models, Turbulence, Wind Speed Gusts.

Introduction

Verification of the structural integrity of a wind turbine according to the Draft IEC 61400-1 code [1] involves analysis of a number of ultimate load cases. Among these is the load case Extreme Operational Gust (EOG), which is of particular relevance for the thrust loading of pitch regulated wind turbines due to its characteristic "Mexican hat" like shape. The EOG load case is a coherent deterministic gust with prescribed time scale and magnitude. The present paper presents a rational method to calibrate the wind speed gust magnitudes specified in the IEC 61400-1 code. In addition the method offers to embed the resulting extreme wind speed gust consistently in a (coherent) stochastic wind field.

Methodology

The method is based on identification of gust occurrences of the prescribed shape and time scale in full scale measurements, followed by an extreme-value analysis of the identified gust magnitudes. The extreme-value analysis encompasses transformation of the estimated extreme gust magnitudes to return periods others than the available recording periods. Finally, the method allows for embedding the resulting extreme gusts in a (coherent) stochastic wind field that can be used as input to aeroelastic simulations of wind turbine response.

Wavelet transformation

Wind speed gust phenomena are typically characterised by having compact support is the time domain as well as in the frequency domain. As a consequence such wind situations are well suited for expansion in wavelets. Inspired by the EOG gust shape, the identification of gust occurrences in measured wind field time series is based on a wavelet expansion of the wind speed signal using the *Mexican hat* wavelet as a mother wavelet. The Mexican hat wavelet is equal to the second derivative of a Gaussian, whereas the EOG load case is expressed in terms of trigonometric functions. However, both formulations are idealisations of a critical wind speed gust shape occurring as realisations in a stochastic field, and the conceptual difference between these is therefore not considered important in the present context. The Mexican hat wavelet is expressed [6] as:

$$\psi(t) = \frac{1}{\sqrt{\Gamma(5/2)}}\left(1-t^2\right)e^{-t^2/2}. \tag{G.1}$$

Basically, a wavelet function must satisfy the weak *admissibility condition* formulated as:

$$C\psi = \int_0^\infty \frac{\left|\hat{\psi}(\omega)\right|^2}{\omega} d\omega < \infty, \tag{G.2}$$

where $\hat{\psi}(\omega)$ is the Fourier transform of $\psi(t)$.

As a consequence of equation G.2 the DC component must equal zero, from which it is seen that a wavelet function must have zero mean. Associated with the mother wavelet is a family of time-frequency "atoms" obtained by scaling and translating the mother wavelet by s and u, respectively. In the process of scaling the mother wavelet function, the energy of the scaled wavelets must be kept constant. This is achieved by suitable normalisation, and the resulting wavelet functions are expressed by:

$$\psi_{u,s}(t) = \frac{1}{\sqrt{s}}\psi\left(\frac{t-u}{s}\right). \tag{G.3}$$

Note, that the wavelet functions expressed by equation G.1 and G.3 are normalised such that

$$(\psi_{u,s}, \psi_{u,s}) \equiv 1, \tag{G.4}$$

where $(*,*)$ denotes the inner product. The wavelet transform of a signal, $f(t)$, is a convolution product given by:

$$W_\psi f(u,s) = (f, \psi_{u,s}) = \int_{-\infty}^{\infty} f(t)\frac{1}{\sqrt{s}}\psi^*\left(\frac{t-u}{s}\right)dt, \tag{G.5}$$

where * denote complex conjugate. A given wavelet coefficient "measures" the correlation of the signal with the particular wavelet. As the Mexican hat wavelet has compact support in the time as well as in frequency, it measures the variations - in the frequency band corresponding to the scale parameter s - of $f(t)$ in the neighbourhood of u. With wavelet functions obeying the *admissibility condition*, it is possible to reconstruct the original signal from its wavelet transform as [6]

$$f(t) = \frac{1}{C_\psi}\int_0^\infty\int_{-\infty}^{\infty} W_\psi f(u,s)\frac{1}{s^{5/2}}\psi\left(\frac{t-u}{s}\right)duds. \tag{G.6}$$

Note, that equation G.6 is true even when the wavelet atoms do not form an orthogonal basis. This is the situation for the Mexican hat wavelet, and the consequence is that some redundant information is hidden in the computed wavelet coefficients.

The constant C_ψ can be analytically determined from equation G.2, and we have the following identity [5]:

$$C_\psi \equiv \frac{1}{2\Gamma\left(5/2\right)}. \tag{G.7}$$

Referring to the EOG load case, the focus is on a coherent wind speed signal, $v(t)$, of the form

$$v\left(t\right) = \frac{A}{\sqrt{s_0}}\psi\left(\frac{t-u_0}{s_0}\right) + g\left(t\right), \tag{G.8}$$

where A is a normalised amplitude, s_0 denotes the wavelet scale corresponding to the requested time extend of the gust, u_0 is the position of gust on the time axis, and $g(t)$ is a stochastic (turbulence) process superimposed on the gust signal. Let us now apply the wavelet transformation, expressed in equation G.5, on the wind speed signal given by equation G.8. Thus

$$W_\psi v\left(u,s\right) = A\left(\psi_{u_0,s_0},\psi_{u,s}\right) + \left(g,\psi_{u,s}\right) \tag{G.9}$$

The particular wavelet coefficient corresponding to scale s_0 and position u_0 is thus

$$W_\psi v\left(u_0,s_0\right) = A\left(\psi_{u_0,s_0},\psi_{u_0,s_0}\right) + \left(g,\psi_{u_0,s_0}\right) \tag{G.10}$$

For a sufficiently large amplitudes A the following approximation is valid

$$W_\psi v\left(u_0,s_0\right) \approx A\left(\psi_{u_0,s_0},\psi_{u_0,s_0}\right) = A, \tag{G.11}$$

where the last identity is obtained from equation G.4.

Suppose, we want to modify the wind field given by equation G.8 in the sense that the amplitude A is to be replaced by an amplitude nA, where n is some (known) factor. The modified wind speed signal, $v_m(t)$, is thus given by

$$v_m\left(t\right) = \frac{nA}{\sqrt{s_0}}\psi\left(\frac{t-u_0}{s_0}\right) + g\left(t\right). \tag{G.12}$$

The wavelet coefficients corresponding to the modified signal is given by

$$W_\psi v_m\left(u,s\right) = nA\left(\psi_{u_0,s_0},\psi_{u,s}\right) + \left(g,\psi_{u,s}\right) \tag{G.13}$$

Combining equations G.10 and G.11, a relation between the wavelet coefficients corresponding to the original wind speed signal and the modified wind speed signal, respectively, is obtained as

$$W_\psi v_m\left(u,s\right) = W_\psi v\left(u,s\right) + \left(n-1\right)A\left(\psi_{u_0,s_0},\psi_{u,s}\right) \tag{G.14}$$

The inner product in the last term of equation G.14 is simply the reproducing kernel of the wavelet. It measures the correlation of arbitrary two wavelet atoms, and is a quality with the applied wavelet and as such independent of the analysed signal. For the Mexican hat wavelet, the reproducing kernel can be evaluated analytically. The computations, as well as the result, is somewhat lengthy, and is therefore not reproduced here - we refer to reference [5]. The interpretation of equation G.14 is that a wavelet expansion of the modified wind speed signal, obtained by increasing the gust amplitude from A to nA, can be obtained by extracting the influence from the original gust on the wavelet coefficients, and subsequently introduce the influence from the modified gust in the wavelet coefficients. Note, that a prerequisite for this transformation is knowledge to the

amplitude A, and thus (from equation G.11) the existence of sufficiently large gusts with the prescribed characteristics in the data material.

Having modified the wavelet coefficients according to equation G.14 the associated time series representation is obtained applying the inverse wavelet transformation, as given in equation G.6, on the modified wavelet coefficients. Note, that (knowing the initial amplitude A) the amplitude of the modified gust equals nA (cf. equation G.12).

The basic idea in the present paper is to identify large values of the amplitude A, from a large number of full scale wind field measurements, by means of wavelet filtering as described above. These gust amplitudes will refer to a limited return period typically given by the length of the available time series records. By use of extreme-value statistics, the most likely gust amplitudes for arbitrary return periods can be estimated and then subsequently introduced in a coherent wind field using the method summarized in equations G.14 and G.6.

Extreme statistics

The occurrence of wind speed gusts (and thus gust extremes), with limited time scale is a result of the stochastic nature of turbulence. It is well known (and intuitively clear) that the amplitude of such gusts is closely related to the standard deviation associated with the stochastic process that describes the wind speed [2]. As the wind speed standard deviation is known to depend strongly on the mean wind speed, the statistics of extreme gust excursions is also likely to depend on the mean wind speed. As a result, the analysis to be outlined in the following involves statistics conditioned on the mean wind speed.

At a given site and in a given height above the surface, we now consider N samples each of size n (which is typically the number of wavelet coefficients corresponding to the prescribed gust time scale within a record time span T) taken from the same population. Referring to the above discussion, we assume the population to be uniquely *defined* by the mean wind speed associated with each sample.

An extreme value distribution can now be established based on the largest value taken from each sample. The distribution of the largest value among N observations must asymptotically approach the distribution of the largest value within samples of size n, provided that an asymptotic distribution exists. An extreme value distribution, EV1, satisfying these requirements can be derived [4]. Initially we will *assume* that the (extreme) computed wavelet coefficients with the requested characteristics, conditioned on the mean wind speed, can be described by this statistical distribution. The extremes, conditioned on the mean wind speed, will thus be distributed according to a cumulative probability density (CDF) function with two parameters of the form:

$$F\left(W_\psi v;\alpha,\beta\,|U\right) = \exp\left(-\exp\left(-\alpha\left(W_\psi v-\beta\right)\right)\right) \tag{G.15}$$

where U denotes the mean wind speed over the sampling period, and (a, b) are the distribution parameters. The scaling and position parameters of the wavelet coefficients have been omitted for convenience. The associated probability density function (PDF), conditioned on the mean wind speed, is given by:

$$f\left(W_\psi v;\alpha,\beta\,|U\right) = \alpha\exp\left(-\exp\left(-\alpha\left(W_\psi v-\beta\right)\right)\right)\exp\left(-\alpha\left(W_\psi v-\beta\right)\right) \tag{G.16}$$

Note, that the distribution parameters in general will depend on the mean wind speed, because this parameter defines the population of observations.

The distribution parameters are estimated using a least square fit in the well established normal score plot depiction [5]. Having estimated the EV1 distribution, corresponding to the return period T, the extrapolation to an (arbitrary)

other return period, pT, are performed based on an independence assumption in a binomial process. The resulting modified extreme value distribution, F_p, is thus determined from

$$F_p\left(W_\psi v;\alpha,\beta\,|U\,\right) = \left[F\left(W_\psi v;\alpha,\beta\,|U\,\right)\right]^p \tag{G.17}$$

The extreme value with a return period equal to pT is the extreme value that *in average* is exceeded only once during the time span pT, thus corresponding to the $(1-1/p)$ quantile in the extreme value distribution F expressed in equation (15). It can be shown [5] that, for the EV1 distribution, the $(1-1/p)$ quantile in F corresponds (for large p) to the mode (i.e. the most likely extreme value) in the Fp distribution. The value of p is related to a distribution conditioned on the mean wind speed. Usually, p is determined by initially selecting a return period corresponding to the overall wind climate on the site - i.e. typically the number of years to be considered. Based on knowledge to the mean wind climate on the site p is easily computed for selected mean wind speed bins. The mean wind speed is conventionally assumed to follow a (two parameter) Weibull distribution given by the following CDF and PDF, respectively:

$$\begin{aligned} F_U(U;k,\beta_U) &= 1-\exp\left[-\left(\frac{U}{\beta_U}\right)^k\right];U\geqslant 0, \\ f_U(U;k,\beta_U) &= \frac{k}{\beta_U}\left(\frac{U}{\beta_U}\right)^{k-1}\exp\left[-\left(\frac{U}{\beta_U}\right)^k\right];U\geqslant 0, \end{aligned} \tag{G.18}$$

where U denotes the mean wind speed, and k, bU are the (shape and intensity) distribution parameters, respectively.

Data material

The method described in Section G has been applied to analyse wind speed gust events originating from a site located in Oak Creek, near Tehachapi in California.

The experimental setup consists of two 80m high meteorological towers erected on a ridge in a complex mountainous terrain. Although the site is complex, the turbulence intensity is not exceptional as seen from Figure G, where the mean turbulence intensity has been depicted as function of the mean wind speed at level 65m.

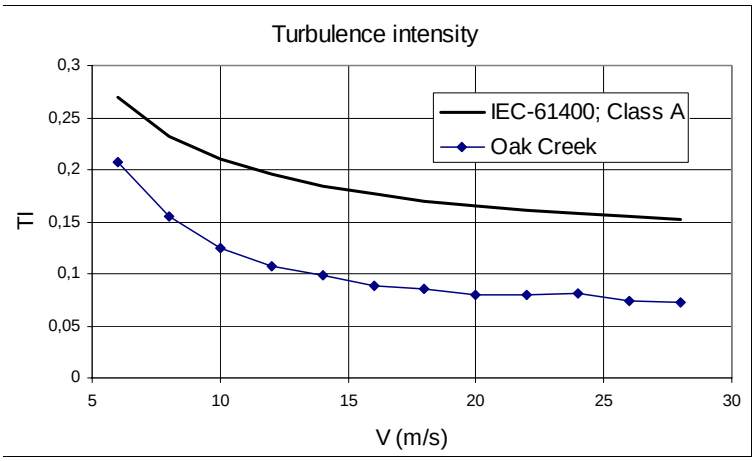

Figure 65. Turbulence intensity as function of mean wind speed at level 65m.

The meteorological towers are intensively instrumented with sensors in several heights above the ground surface. For the present investigation only cup anemometer recordings from the 65m level are applied, motivated by the fact that this level is close to the hub height for a modern wind turbine. The cup anemometer signal has been recorded with a sampling frequency equal to 8Hz.

The measurement campaign has been running from May 1998 until November 2000, and it has resulted in a large number of wind field time series covering a mean wind speed range extending from 0.5m/s to 29.4m/s. Of these 9506 10-minute time series have been selected covering the normal operational regime of a wind turbine. The recording system is designed to deliver an overrepresentation of time series with mean wind speeds above 15m/s, compared to a continuous recording strategy. This is an advantage for the present type of analysis based on extreme distributions conditioned on the mean wind speed, as it ensures a fair representation of events even in mean wind speed bins with representing high mean wind speeds.

Data analysis

The first step is to identify occurrences of wind speed gusts, with prescribed characteristics concerning shape and time scale, using a filtering process based on a wavelet expansion.

Wavelet transformation

The IEC code operates with characteristic time scales for (coherent) wind speed gusts equal to 10.5s and 14.0s for gusts with recurrence periods of 1 year and 50 years, respectively. Initially, these time scales are transformed to characteristic wavelet scales. Referring to equation G.3, we denote these s_1 and s_{50}, respectively.

Subsequently, a suitable discretization of the wavelet space is performed in terms of the scaling and translation parameters s and u (c.f. equation G.3). Care must be taken that s_1 and s_{50} are realised in the discretization of the scaling parameter s. For the discretization of the translation parameter u, it is important that the increments are small compared to the characteristic gust time scales in question. The reason is that the approximation expressed in equation G.11 is best when, in the wavelet domain, the characteristic gust is resolved primary in one dominating wavelet coefficient.

With the selected discretization, the wavelet transformation is performed in accordance with the direction given in equation G.5, except that the finite length character of the investigated time series implies that the integration interval is also of finite length. However, due to the *cone of influence* [6] for the support of a given wavelet atom, the integration interval must exceed the length of the analysed time series. For the present investigation, it was, somewhat arbitrary, selected to extend the integration t-regime with 5s in both ends of the available wind speed time series. Within these 2×5s intervals a function value of zero has been assumed. For an arbitrary time series, the result of the wavelet transformation is illustrated in Figure G.

Having performed the wavelet transformation for all available time series, the wavelet coefficients with scales s_1 and s_{50} are extracted for a succeeding extreme value analysis.

Extreme statistics

Initially, the extracted wavelet coefficients are binned according to the mean wind speed of the wind speed time series they refer to. A step in bin size equal to 2m/s

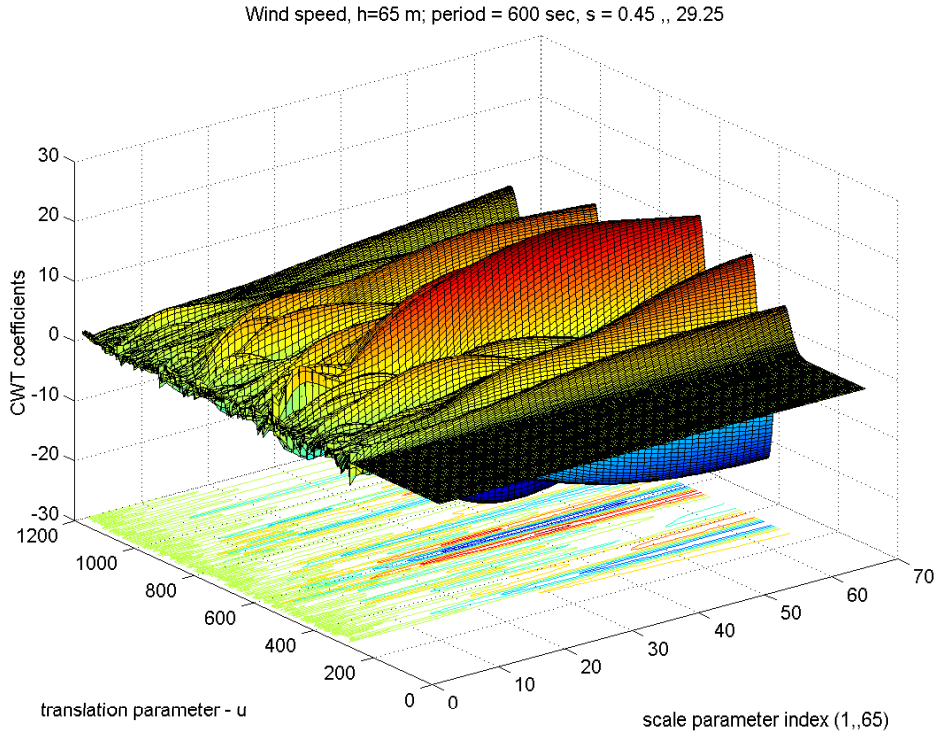

Figure 66. Wavelet coefficients resulting from the selected resolution

has been selected, and the wind speed regime outside the normal operation regime ($5\text{m/s} < U < 25\text{m/s}$) of a wind turbine is excluded from the analysis. The width of the mean wind speed bins is as usual a compromise between a suitable mean wind speed resolution and the number of resulting extreme events available for performing the statistical fits.

For each time series, belonging to a particular mean wind speed bin, the largest wavelet coefficients (with scales s_1 and s_{50}, respectively) are identified and used as basis for the extreme value analysis, by fitting these to a (conditioned) distribution of the type given in equation G.15. The fitting is performed by plotting the identified (extreme) wavelet coefficients in an EV1 depiction, and subsequently derive the distribution parameters from a linear least square fit to these observations. For an ideal EV1 distributed variable, the EV1 depiction results in a linear relationship. It is characteristic that the present data material results in a very close to linear behaviour, thus confirming the conjecture of the present extreme wavelet coefficients being approximately EV1 distributed. Representative examples of EV1 depictions of extreme wavelet coefficients for two different mean wind speed bins are given in Figure G.

With the estimated distribution parameters, the (conditional) extreme distributions of wavelet coefficients with scales s_1 and s_{50} are defined corresponding to a return period equal to the length of the investigated time series (10 minutes). A representative example of probability density functions (PDF) of extreme wavelet coefficients, related to the mean wind speed interval ranging between 9m/s and 11m/s are presented in Figure G.

The last step, in the extreme value investigation of the selected wavelet coefficients, is to transform the estimated PDF's, referring to a return period equal to 10 minutes, to return periods of 1 year and 50 years, respectively. More specific, the PDF's of wavelets with scale s1 is transformed to 1 year recurrence period distributions, whereas the PDF's of wavelets with scale s_{50} is transformed to 50 year

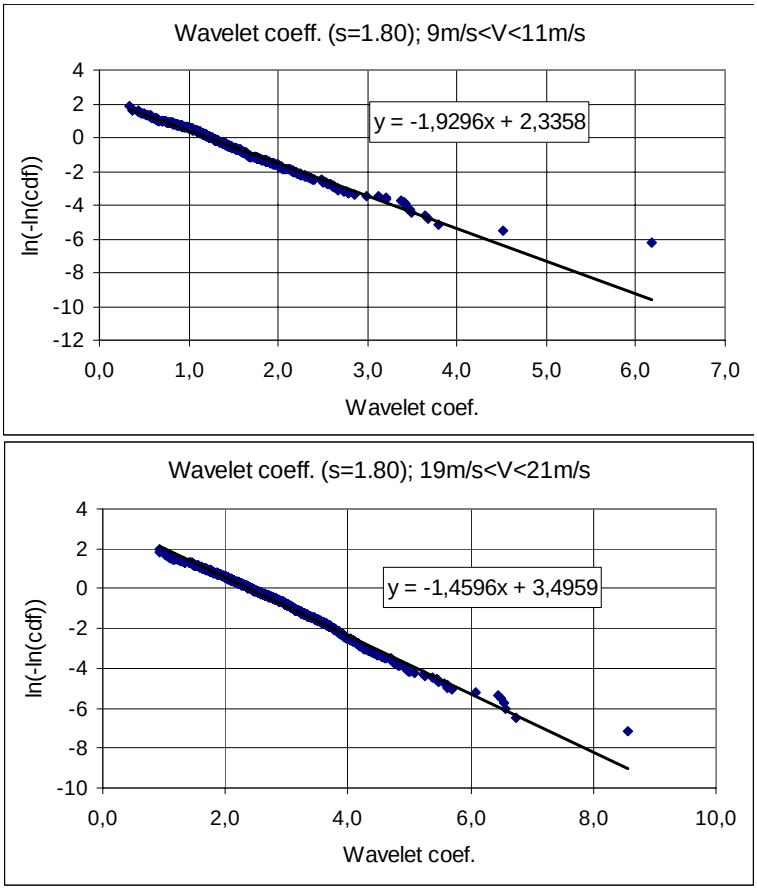

Figure 67. EV1 depiction of extreme wavelet coefficients corresponding to scale s_{50}.

recurrence period distributions. The transformation is performed in accordance with the method described in Section G, assuming an IEC Class 1 site (annual mean wind speed equal to 10m/s) and a shape factor in the mean wind speed Weibull distribution (c.f. equation G.18) equal to 2, which makes it degenerate to the Rayleigh distribution applied in the IEC code.

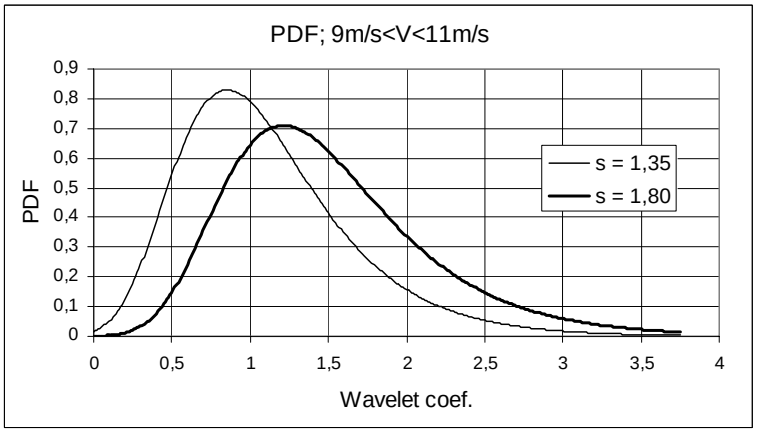

Figure 68. PDF of extreme wavelet coefficients with scales s_{50} *and* s_1*, respectively.*

Results

The estimated extreme distributions of the selected wavelet coefficients associated with recurrence periods equal to one year and fifty years, respectively, have been used to estimate the *most likely* peak-peak value of IEC gusts with recurrence periods 1 year and 50 year, respectively. The peak-peak values are determined by combining the values of the most likely extreme wavelet coefficients with. equations G.3 and G.11. Note, that the estimated peak-peak values refer to the turbulence intensity level prevailing at the measuring site.

The estimated peak-peak values are subsequently compared with corresponding values obtained from the IEC code. The results for recurrence period 1 year and 50 years are shown in Figures G and 69, respectively.

It is characteristic that the IEC recommendations substantially over-estimates the observed extreme gust peak-peak values at the investigated site, when based on turbulence class A or B specifications.

However, if the standard turbulence description is replaced by the prevailing turbulence intensity at the present site, as given in Figure G, the IEC recommendation turns out to under-estimate the estimated extreme gust peak-peak values.

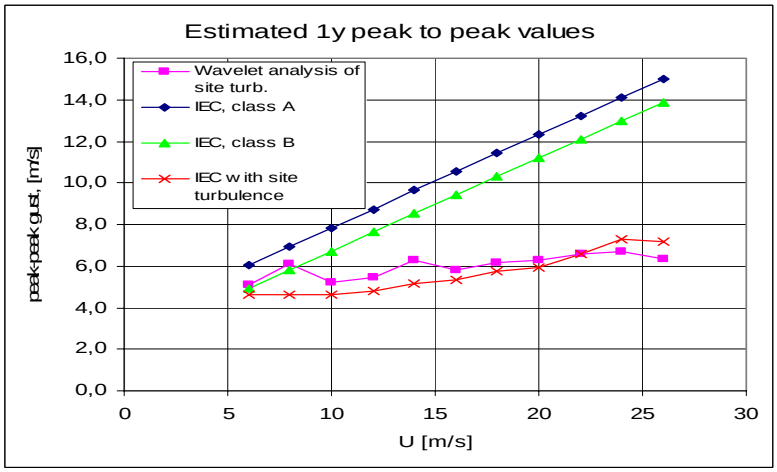

Figure 69. Gust peak-peak values (1 year).

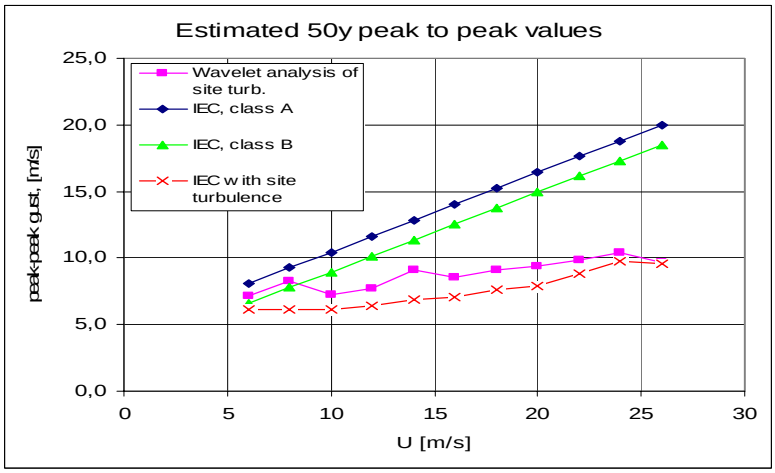

Figure 70. Gust peak-peak values (50 year).

In a conventional spectral turbulence description [1], the turbulence energy scales directly with the turbulence intensity squared. As a consequence, the turbulence velocity components scales directly with the turbulence intensity. Everything else kept constant this means that the gust amplitudes scales with the turbulence intensity. The consequence is that, for a given turbulence intensity, the IEC code tend to under-estimate the extreme gust peak-peak value for the EOG load case.

Conclusion

Based on a large number of one point measurements, extreme (coherent) wind speed gust events with return periods 1 year and 50 years, respectively, have been estimated. For the relative large wind speed gust time scales investigated, it has thus implicitly been assumed that one point gusts adequately represent fully coherent gusts over the rotor plane of a wind turbine. The gust estimates have subsequently been compared with predictions based on the IEC code. For identical turbulence conditions, the IEC code tend to somewhat under-predict the estimated extreme gust events, except for the high wind region associated with the return period 1 year.

Still outstanding are analyses of the criticality of other gust time scales as well as the sensibility of the estimated extreme gust events with the turbulence structure. More specific, the influence from Gaussian ctr. non-Gaussian turbulence behaviour, turbulence length scale and turbulence coherence characteristics should be investigated.

Acknowledgement

The Danish Energy Agency funded the present work under the contract ENS 1363/01-0005.

References

1. IEC 61400-1 Wind Turbine Safety System: Part 1, Safety Requirements.
2. Bierbooms, W., Cheng, P.W., Larsen, G.C. and Pedersen, B.J. (2000). Modelling of Extreme Gusts for Design calculations - NewGust. Publishable Final Report, TU Delft, Delft, The Netherlands.
3. Database on Wind Characteristics. http://www.winddata.com/.
4. Gumbel, E.J. (1966). Statistics of Extremes. Columbia University Press.
5. Larsen, G.C., Pedersen, B.J. and Hansen, K.S.. Extreme coherent wind speed gusts. To appear.
6. Mallat, S. (1998). A Wavelet Tour of Signal Processing. Academic Press.

Bibliographic Data Sheet **Risø–R–1437(EN)**

Title and author(s)

Wind Simulation for Extreme and Fatigue Loads

M. Nielsen, G. C. Larsen, J. Mann, S. Ott, K. S. Hansen, and B. J. Pedersen

ISBN	ISSN
87–550–3281–8(Internet)	0106–2840

Dept. or group	Date
Wind Energy	January 7, 2004

Groups own reg. number(s)	Project/contract No.
1100 078-1	EFP 1363/01-0005

Pages	Tables	Illustrations	References
104	3	70	39

Abstract (Max. 2000 char.)

Measurements of atmospheric turbulence have been studied and found to deviate from a Gaussian process, in particular regarding the velocity increments over small time steps, where the tails of the pdf are exponential rather than Gaussian. Principles for extreme event counting and the occurrence of cascading events are presented. Empirical extreme statistics agree with Rice's exceedence theory, when it is assumed that the velocity and its time derivative are independent. Prediction based on the assumption that the velocity is a Gaussian process underpredicts the rate of occurrence of extreme events by many orders of magnitude, mainly because the measured pdf is non-Gaussian.

Methods for simulation of turbulent signals have been developed and their computational efficiency are considered. The methods are applicable for multiple processes with individual spectra and probability distributions. Non-Gaussian processes are simulated by the correlation-distortion method. Non-stationary processes are obtained by Bezier interpolation between a set of stationary simulations with identical random seeds. Simulation of systems with some signals available is enabled by conditional statistics.

A versatile method for simulation of extreme events has been developed. This will generate gusts, velocity jumps, extreme velocity shears, and sudden changes of wind direction. Gusts may be prescribed with a specified ensemble average shape, and it is possible to detect the critical gust shape for a given construction. The problem is formulated as the variational problem of finding the most probable adjustment of a standard simulation of a stationary Gaussian process subject to relevant event conditions, which are formulated as linear combination of points in the realization. The method is generalized for multiple correlated series, multiple simultaneous conditions, and 3D fields of all velocity components. Generalization are presented for a single non-Gaussian process subject to relatively simple conditions, i.e. gusts and velocity jumps. Further generalizations for simulation of multiple correlated non-Gaussian processes are suggested.

Descriptors

COMPUTERIZED SIMULATION; DATA ANALYSIS; FATIGUE; GAUSSIAN PROCESSES; STORMS; THREE-DIMENSIONAL CALCULATIONS; TURBULENCE; VELOCITY; WIND LOADS; WIND; WIND TURBINES